Failure Prediction of Membrane Electrode Assemblies for Proton Exchange Membrane Fuel Cells

January 2016

A thesis submitted in partial fulfilment of the requirements for the degree of
Doctor of Philosophy in Engineering

Keio University

Graduate School of Science and Technology
School of Integrated Design Engineering

Thibaud Vermot des Roches

TABLE OF CONTENT

List of Figures

List of Tables

Chapter 1

INTRODUCTION

1.1. Research Background

In a context of growing concern over the depletion of petroleum-based energy resources, the broad question of the use of energy, from its generation to the disposal of by-products, emerges as one of the major political, social and environmental issues of this century. Much of the current infrastructure relies heavily on the availability of cheap, high energy density fuels extracted from fossil reserves. Switching to a sustainable infrastructure, both from the point of view of consumption and pollution, requires the accumulation and efficient use of ambient sources into usable energy form. Owing to its ease of distribution, electricity is a preferred form, but not ideal: it is difficult to store on a large scale and requires conversion to higher density states for some applications such as automotive uses. In this respect, a crucial aspect in the development of sustainable energies lies in the ability to perform efficient conversion of energy from solar, chemical or thermal to electricity.

Much recent research has been focused on this objective. Fuel Cells have been developed as a way to convert chemical energy into electricity. Even though several varieties of fuel cells exist, they all work on the same idea. An anode and a cathode are separated by an electrolyte. Two partial chemical reactions occur at the electrodes; the electrolyte is such that it is permeable to ions, but not to electrons. Electrons freed by the reaction, created at the anode and consumed at the cathode, flow through an external circuit and are the source of the created electric current. Currently used fuel cells have power outputs ranging in the hundreds of kilowatts, though this number can easily be scaled up for the needs of large stationary units. As it stands, most stationary or portable fuel cells have a power output inferior to ten kilowatts, but the power output for transportation is higher, from around a hundred kilowatts for a personal vehicle to double or triple that number for a city bus.

Studies have shown a great increase of commercial interest for fuel cells since 2007, and this tendency seemed only to accelerate in the past few years, as is clearly visible in Fig 1.1. It can be said that today, fuel cells are no longer a technology of the future: some applications are commercially available today. In particular, Fuel Cell vehicles keep attracting the automobile industry, with newer models being released at ever more affordable prices.

1.1.1. Basic function of a Proton Exchange Membrane Fuel Cell

Among the different types of fuel cells, Proton Exchange Membrane Fuel Cells (PEMFCs) have drawn particular attention thanks to their high performances. They employ a hydrophobic solid polymer as the electrolyte, reactants being hydrogen and oxygen gases. The full reaction,

$$2H_2 + O_2 \rightarrow 2H_2O, \tag{1.1}$$

is split into the anode and cathode half reactions, respectively,

$$H_2 \rightarrow 2H^+ + 2e^-, \tag{1.2}$$

$$\frac{1}{2}O_2 + 2H^+ + 2e^- \rightarrow H_2O\,. \tag{1.3}$$

The overall structure of a PEMFC is given in Fig. 1.2, and will be discussed in more details in Chapter 2. The membrane electrode assembly (MEA), composed of the two electrodes and of the electrolyte membrane, is the central part of the cell and plays a critical role by being the siege of the chemical reaction, conducting protons between the electrodes while acting as a barrier for the reactants and as an electronic insulator[3].

By allowing efficient conversion of chemical energy into electricity, PEMFCs are considered a promising technology for a variety of power generation applications. In particular, there is great interest in using them as an alternative to traditional internal combustion engines for automotive applications. The superiority of fuel cell technology over conventional engines in several aspects have been demonstrated, including high energy concentration and high efficiency (over 50% for PEMFCs), easy scale-up and, most importantly, no emissions, the only by-products being water and heat[2]. PEMFCs in particular have some advantages over other fuel cells, namely rapid start-up and shut-down transients, and relatively low working temperatures (from 50 to 120°C). Also, the fact that any fuel that can provide a source of hydrogen can be used by a PEMFC

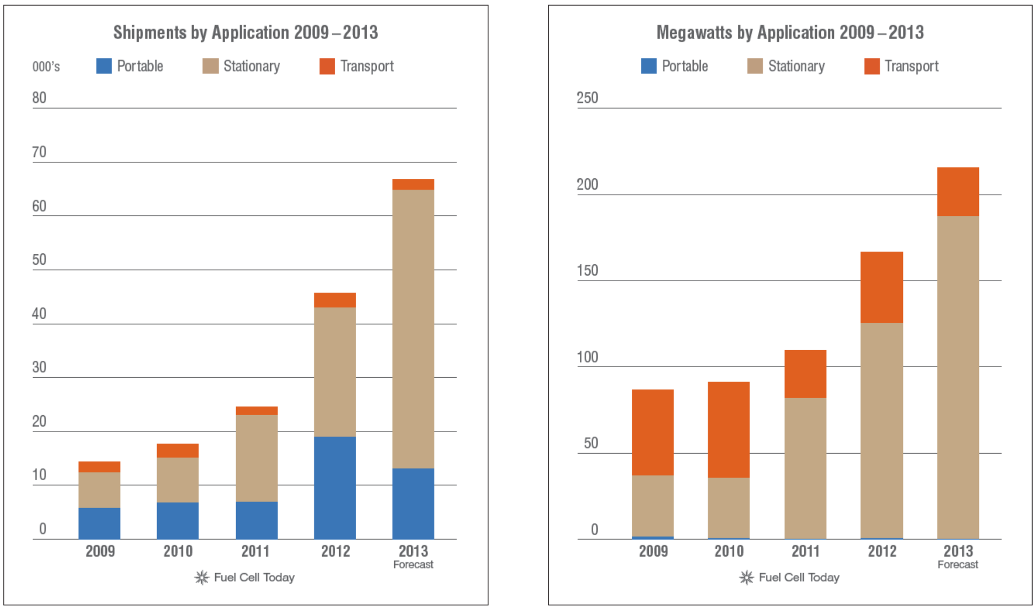

Fig. 1.1. Development of the fuel cell market since 2009 [1]

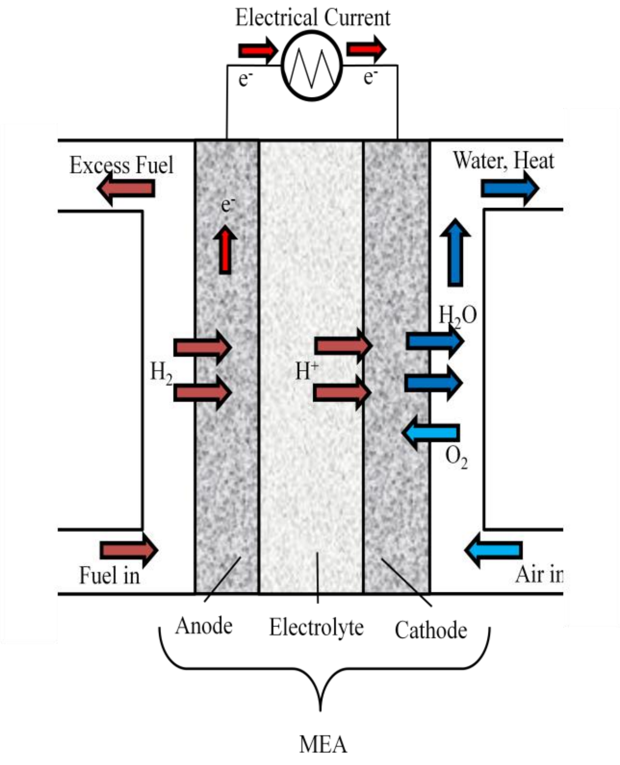

Fig. 1.2. Overview of the structure and functioning of a PEMFC

accounts for a great versatility and adaptability of these systems. For these reasons, it was reported that in 2010, 97% of the fuel cells shipped worldwide were PEMFCs, most of these being portable systems with relatively low power[1]. This domination is expected to continue, as PEMFCs are likely to continue being the technology of choice for the development of future fuel cells vehicles.

In practical applications, high proton conductivity has been the determining factor in choosing and designing the membrane. In recent years and with the rise of expectations regarding the longevity of the fuel cell, other factors such as mechanical and chemical stability have come to importance. Degradation of the membrane eventually leads to pinhole formation, allowing fuel crossover. This dramatically reduces the efficiency of the cell by wasting the products of the reaction as just heat, decreasing the voltage of the cell. Since fuel cell stacks are generally serially connected in order to reach a useful output voltage, a voltage drop of one cell decreases the voltage of the entire stack. For these reasons, reliability of the MEA is the most important factor when considering the reliability of the entire cell.

1.1.2. Barriers to commercialization

Despite their attractive features, some important issues remain to overcome in order for fuel cells to become economically viable alternatives to conventional power units, cost and durability being the most widely mentioned.

For the PEMFC to emerge as a competitive technology, reliability has to be extended while still reducing the costs. The targets set by the United States Department of Energy, updated in 2011, estimate that by 2017 a lifetime of 5,000 hours for transportation application should be achieved, at a cost no greater than $30/kW[5]. As of 2011, studies report that a lifetime of 2,500 hours and a cost of $49/kW were reached. The mentioned costs are for complete systems, including the fuel cell stacks, and the auxiliary systems necessary for the function of the fuel cell, such as the pumps to bring the reactants to the electrodes. The cost target for the fuel cell stack alone is set to $15/kW, with current performances of $22/kW. Inside the fuel cell stack, the MEA generates most of the cost, with current status of $13/kW and a 2017 target of $9/kW. As for durability, the MEA is the limiting factor. Though it is possible to create membranes with lifetimes that reach the 5000 hours objective, their performance is not yet satisfying as the voltage degradation also needs to be minimal after that time. A voltage drop that is too large would result in an unusable system.

The high cost of a MEA can be partly accounted for by the necessity of catalyzing the reaction. In order to split the hydrogen and oxygen the most appropriate catalyst material to date is platinum, and much progress has been made in the later years in order to reduce the quantity needed. Two concurrent approaches are used when trying to reduce costs: either to optimize the design and composition of existing materials, or to search for innovative materials[4]. Because the field of study is relatively recent, the materials and designs used today cannot be said to be definitive.

Durability is dependent on the reliability of the components, which are subject to an aggressive chemical and thermal environment. Any failure of the MEA will compromise the function of the PEMFC by dramatically reducing the power output, and there is much ongoing research to get a better understanding of its properties. Failure of the MEA can be attributed to several causes. Chemical or thermal instability can cause the MEA to fail, however the recent development of more stable materials has made this mode of failure secondary[6].

It has been shown that the principal cause of failure or of performance degradation for the MEA was the humidity at the electrodes[7,8]. As has already been mentioned, water is created at the cathode as a product of the reaction. This water has then to be evacuated as new reactants are brought to the cathode, or after shutdown of the fuel cell. The membrane, electrodes and gas diffusion layers being porous, water can be found throughout the MEA. As water is absorbed by the different components of the MEA, they swell, and this results in mechanical strains to the system. Because humidity varies between ambient levels and high water concentrations with time, the different layers of the MEA are subjected to cyclic loading, which is likely to induce fatigue, and eventually failure, of the assembly.

Another limiting factor is oxygen crossover, which is susceptible to affect the electrodes. It usually happens as a consequence of pinhole formation in the polymer. This is especially a concern during startup after a long idle time, as ambient air is present near the anode. Although this does not result in failure of the system, oxidization of the electrodes can decrease the voltage output (by increasing the resistance), thus reducing the performance.

The risks factors for fuel cell performance that are related to mechanical degradation are most pronounced at the MEA. As will be discussed in details in Chapter 2, the other components of the fuel cell have different constraints that make it possible to select materials that are less prone to mechanical degradation. A simple fault-tree analysis for the loss of performance of the cell is shown in Fig. 1.3. In order to achieve a greater lifetime for PEMFCs, it is necessary that all the failure mechanisms of its components be clearly understood and documented.

1.1.3. Review of existing studies

Many studies have been conducted in the past in order to model the functioning of a fuel cell. There have been much interest in the physical and chemical aspects of the gas flow through the layers and of the interactions between reactants[9-11]. These studies usually focus on the static and dynamic behavior of the fuel cell components, but do not take into account mechanical strains or failure.

Some research exists on catalyst layers aiming to make its structure optimal, but its

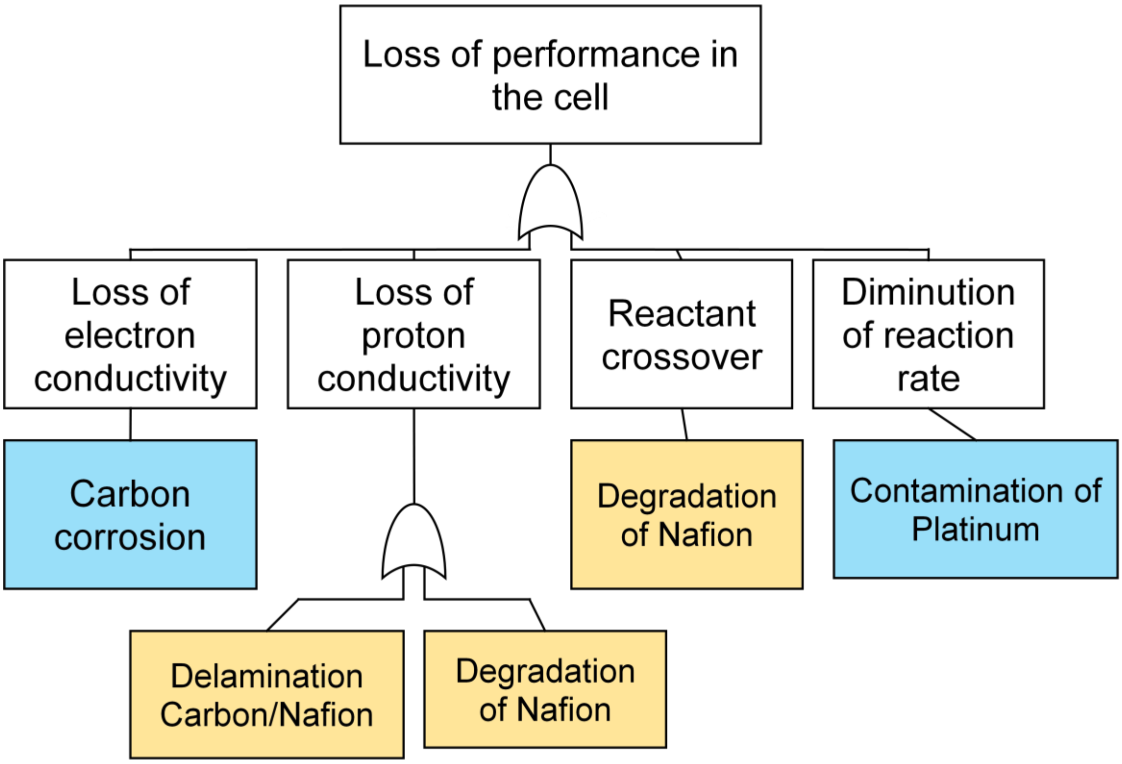

Fig. 1.3. Simplified fault-tree analysis of the cell. In blue are the chemical causes, in orange the mechanical causes of performance loss

mechanical properties are not well documented[12-15]. This is made more difficult by the fact that there is not yet a standard for catalyst layers, so their mode of fabrication is often kept confidential by industrial makers. Recent research on catalyst layers have been aimed at reaching maximal activation of the catalyst, with the objective of reducing the quantity of platinum needed. The use of a core-shell structure for catalyst particles have shown promising results[14,16-18].

Several studies have introduced experimental protocols for accelerated fatigue tests to estimate the lifetime of fuel cells components and to investigate the possible modes of failure. By subjecting a MEA to rapid cycles of voltage and humidity, Jao et al. have concluded that catalyst degradation was the leading cause for MEA decay, followed by creep deformation[19].

Other factors likely to affect the durability of a fuel cells stack have been examined: Oyarce et al. have compared different shut-down strategies and studied their effect on the durability of the cell[20]. Luo et al. have studied the effect of freeze-thaw cycles on the function of the cell[21]. Thermal management within a fuel cell stack has also been a subject of interest: recently, Sasmito et al. have proposed a method to improve cooling of the fuel cell stack by improving the design for convective cooling[22].

Naturally, the proton exchange membranes have also received a lot of attention. A widely used material for the ion-exchange membrane is Nafion®, commercially available from the company DuPont™. Nafion is a perfluorosulfonic acid polymer with a good chemical stability. Due to its large popularity in fuel cell applications, all experiments and models in this thesis use Nafion as the material for the proton exchange membrane. An in-depth discussion of its characteristics can be found in chapter 2.

Since Nafion is the most commonly used material for that purpose, it has been the most studied, although some attempts have been made in order to find and study the feasibility of cheaper alternatives[12,23-26]. When it comes to Nafion, a lot of efforts have been made in order to understand its complex viscous behavior. Most of the reviewed studies have been focused on studying its morphology, through various methods[27], its chemical behavior with respect to ions and water absorption[28-33], and trying to understand and model its mechanical properties. Most mechanical models that were found in the literature were concerned with local behavior on a micrometer scale, with only few dealing with large deformations of the material on a macroscopic scale[3,10,27,34-40]. The effects of various external parameters like temperature or chemical environment are investigated, but the failure of Nafion has only started to be systematically studied in the past few years. Notably, Kusoglu and Santare have studied the effect of humidity cycling on the membranes[41-43]. Creep failure and its effect on the mechanical endurance of Nafion has been discussed by Solasi et al.[37,44-45] On a related topic, Dillard, Gittleman et al. have investigated the mechanical fatigue of Nafion[38,46-47].

1.1.4. Numerical simulation method

Numerical models are a convenient way to estimate the properties of a fuel cell or of its individual components; the alternative being systematic experiments, which are expensive, time consuming and require the use of multiple prototypes. Though some amount of experimental data is necessary to calibrate and validate the numerical models, this method still allows to save much valuable resources.

The materials used in the fuel cell industry have for the most part been developed recently, and sometimes their manufacturing process is confidential, due to industry constraints. For these reasons, documentation on the properties of these materials is scarce. To date, further experimental investigations are still needed in order to fully determine the properties of the components in a large range of environmental conditions. As a consequence, proper characterization of the materials is the first hurdle when designing a numerical model for a PEMFC. The advantage of this approach however is that once an accurate constitutive model for the materials is achieved, the numerical simulation allows to gain insights about the behavior of the MEA in a wide variety of applications, with more flexibility than experiments.

There is currently no definitive numerical model to predict the behavior of Nafion, although several models have been proposed, with varying degrees of success. As a general rule, studies have had to compromise between complexity and difficulty of implementation. What generally limits existing models is the change of environmental conditions.

- The most simplistic model is the linear elastic-plastic model; it does not take into account the viscous behavior of Nafion and therefore is very limited in its applications.

- The 2-layer viscoplastic model was applied to Nafion by Solasi et al. in 2008[48]. By adding a viscous component to the elastic-plastic model, it greatly improves the accuracy of the model, especially around the yielding point. The disadvantage of this model is that it doesn’t take into account environmental parameters, so the model has to be fitted separately for each set of conditions.

- In 2011, a nonlinear viscoelastic–viscoplastic constitutive model was proposed by Yoon and Huang[49]. This model is based on an earlier model introduced by Bergström and Boyce in 1998[50], that uses the microstructure of ionomers to deduce constitutive equations. Applied to Nafion, this model gets very good results over a wide range of strains, but a limiting factor is that, similarly to the 2-layer viscoplastic model, it requires a different set of parameters for each set of environmental conditions. As a result, the model cannot be used when variations of temperature or humidity happen as part of the simulation.

- Independently from the previous model, Boyce and Silberstein have introduced a different viscoelastic-viscoplastic model for Nafion with promising results, that they later improved[51-55]. This model is also inspired from the microstructure of Nafion. Its advantage over the previously discussed model is that it takes into account the dependence of Nafion on the temperature and humidity. By introducing back stresses in the constitutive equations, it is also successful in modeling the unloading and reloading behavior. However, the model was only tested for strains of up to around 0.6, which is a somewhat limited range since Nafion can sustain stresses well over that point. It also does not take into account fatigue of the material.

While the recent interest in investigating the mechanical behavior and failure of fuel cells is clear, there has not yet been a systematic study of the failure behavior taking into account variations of temperature or humidity. The exact failure mechanisms of the MEA are still unclear, as most of the research has been focused on power output rather than mechanical integrity. For this reason, the estimation of the lifetime of components has mostly been empirical. There is also a lack of numerical models to simulate the mechanical behavior of the cell. While such models would be valuable to assist in the design and evaluation of fuel cells, exiting models in the reviewed literature are generally limited in the scope of their application due to not taking into account environmental conditions or failure of the materials.

1.2. Purpose of the study and outline of thesis

Generally, the mechanical integrity of materials is determined by their fracture resistance, under both static and dynamic loadings. In many cases where the material is ductile (which is the case of the polymers that form the MEA), the failure is not a catastrophic event, rather there is a phase of crack propagation, which can take a large portion of a material’s lifetime[47,56-58]. Knowing the material’s resistance to fracture is essential for both estimating its lifetime and for coming up with more efficient designs, whether it is by postponing the apparition of cracks or by minimizing the speed of crack propagation.

In the case of the MEA, mechanical strains appear from the successive swelling and shrinking that occurs upon variations of environmental conditions, in particular variation of humidity. Such cyclic variations are inevitable as water is created in the catalyst layer by the oxydo-reduction reaction, is then evacuated and eventually returns to ambient conditions when the cell is shut down (Fig. 1.4 (a)). Such cycling of swelling strains leads to mechanical fatigue and crack formation in the catalyst layer (Fig. 1.4 (b)). In Chapter 3, a model is proposed to elucidate the mechanism of crack initiation. While crack initiation might decrease the efficiency of the cell (by reducing its active area), it does not compromise its integrity. Several cracks might thus form in the catalyst layer, which then start to propagate in the ductile ionomer that forms the substrate of the layer (Fig. 1.4 (c)), and then in the proton exchange membrane. For this reason, when studying the cause of failure of a fuel cell, it is common to observe pinpoint cracks on the surface of the membrane (Fig. 1.4 (d)). As cracks keep propagating, they eventually reach the opposite side of the membrane. This causes gas crossover, as the reactants are now able to pass directly from one electrode to the other, which results in a rapid loss of performance and ultimate failure of the cell (Fig. 1.4 (e)).

The objective of this dissertation is to systematically study the fracture behavior of the MEA

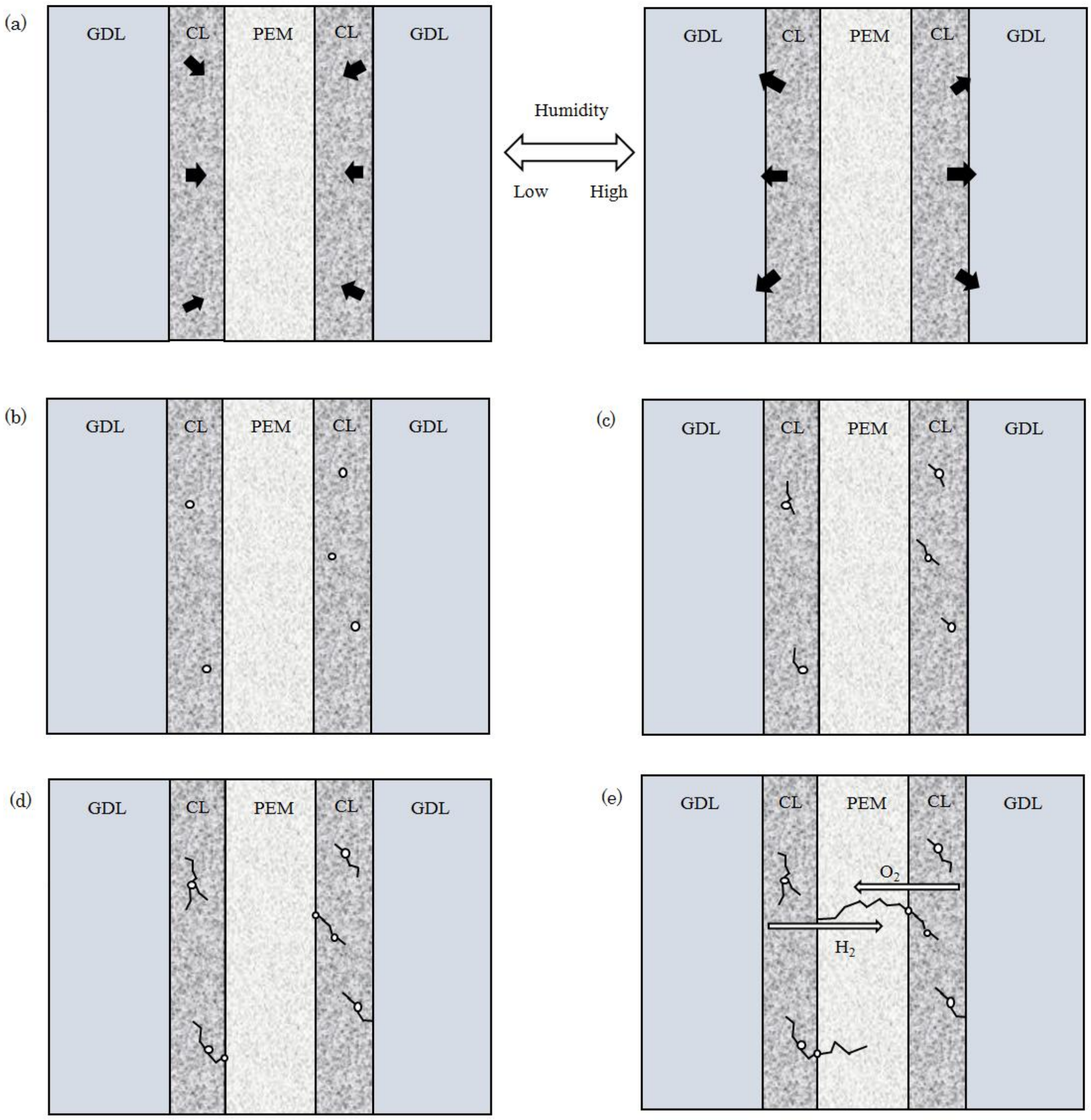

Fig. 1.4. Typical scenario for the mechanical failure of the MEA: (a) Cyclic variations of humidity create swelling and shrinking strains in the MEA; (b) Crack initiation occurs inside the CL; (c) Cracks start to propagate in the CL; (d) Cracks start to pinpoint the surface of the PEM; (e) Crack propagation reaches the opposite side of the membrane, allowing reactant crossover and failure of the cell.

in order to propose a failure criterion and quantitative data to better estimate its lifetime. The scope of the study includes static and dynamic failure, as well as crack propagation. In order for the data to be applicable for fuel cells in practice, the same experiments are repeated in different conditions of temperature and humidity.

On top of that, this study aims to develop a numerical model able to simulate the failure of the MEA. As compared to experimental tests, numerical simulations are quicker to perform, need less material and are more easily reproduced or adapted. Thus, numerical simulations are both cheaper and more convenient to realize, so having the ability to rely on a simulation while bypassing the experimental process would be a sizable advantage. In addition, a numerical simulation may give additional insights into the behavior of the material which would be hard to get from experiments, such as stress distribution or dissipated energy. Naturally, these simulations need first to be validated against experimental data in order to be useful, which this study aims to accomplish.

The steps taken in this study in order to investigate the fracture resistance of the MEA are as follows. Tensile experiments are done to collect data on its mechanical behavior. The data is used to calibrate the constitutive model for both materials in the MEA, and a critical fracture stress is extracted. Following this, fatigue tests are performed both experimentally and numerically, and a fracture criterion for cyclic failure is proposed. The chosen approach to quantify the resistance to fracture is to calculate the Essential Work of Fracture. Once again, experimental results are complemented by finite element analysis. The combination of these results equips us with valuable insights about the fracture resistance of MEAs. This approach is summarized in a flow chart in Fig. 1.5.

Following this introduction, **Chapter 2** gives a detailed overview of the structure of a PEMFC stack, and of the state of knowledge of the materials that compose it. This includes the proton exchange membrane and the catalyst layers (together forming the MEA), the gas diffusion layer (GDL) and the bipolar plates. The characterization of the mechanical properties of Nafion is given special attention.

In **Chapter 3**, the crack initiation inside the MEA is investigated. Based on cyclic loading experiments, the MEA is found to follow a Coffin-Manson law. A numerical scheme is proposed in order to corroborate experimental results. A failure criterion for determining the failure from fatigue of the catalyst layer is introduced and discussed. Finally, using insights from the numerical model, the mechanics of Nafion slippage and decohesion from the molecules of carbon black is introduced as a possible explanation for the origin of cracks in the catalyst layer.

The focus of **Chapter 4** is to improve upon the constitutive models of Nafion discussed in Chapter 2. When dealing with the failure of Nafion, it is necessary that the model used stays accurate even at high strains. Based on the viscoplastic model proposed by Prof. Boyce, a least square optimization is conducted in order to ensure the best possible fit throughout the entire range of strains.

The fracture resistance of Nafion is the subject of **Chapter 5**. The results of a double-edge notch tensile (DENT) test are shown for different environmental conditions, giving insights on the fracture resistance of the membrane. Two environmental parameters are controlled, temperature and humidity. Following the DENT test, the fracture surfaces of post-mortem specimen are observed on a scanning electron microscope, revealing the effect of the environment on the fracture mechanisms.

In **Chapter 6**, a numerical model aimed at reproducing the result of the DENT test is introduced. The model is shown to be able to accurately estimate the work of fracture of Nafion. The plastic zone around the crack tip during the DENT test is examined for the different sets of environmental conditions tested. Their effects on the plastic zone and consequently on the work of fracture is discussed.

Finally, **Chapter 7** summarizes the research findings and draws the conclusions of the study and their significance about the fracture resistance on membrane electrode assemblies in proton exchange membrane fuel cells. Future directions for research in this field are discussed.

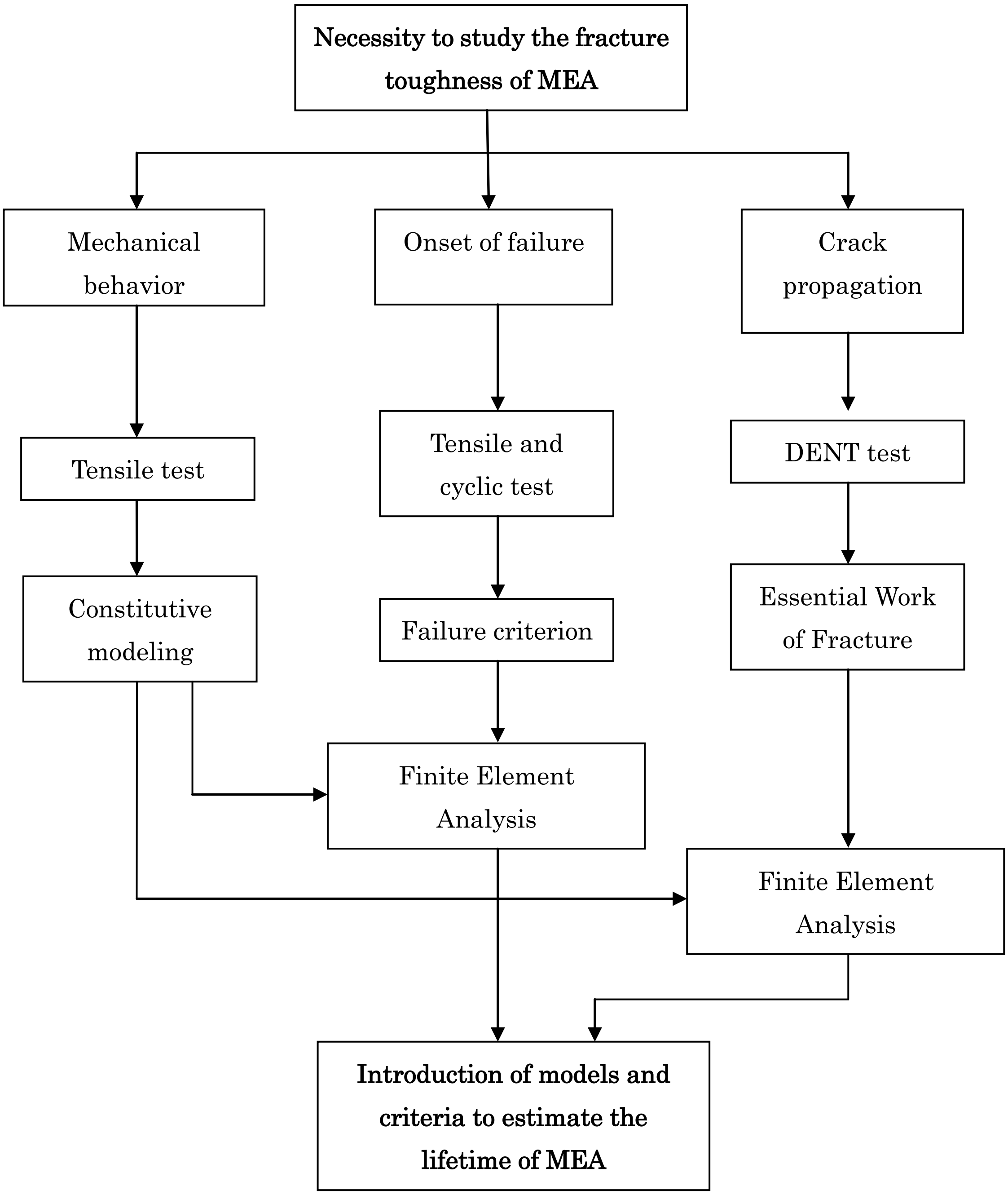

Fig. 1.5. Flow chart of the dissertation

CHAPTER 2

Structure of a Proton Exchange Membrane Fuel Cell

This chapter gives a detailed overview of the function of a Proton Exchange Membrane Fuel Cell, the different components that enter its composition and the requirements that these components must verify in order for the cell to work properly. Mechanical characterization of the Membrane Electrode Assembly is also discussed.

2.1. Functionality

At its core, a PEMFC is divided into two electrodes separated by a proton exchange membrane (PEM). The two reactants that are used are dihydrogen and dioxygen in gas form, combining them produces water. By dividing the reaction between the two electrodes separated by an electrically isolating membrane, the electrons freed up by the reaction are forced to travel to an external circuit, and the current is used to generate electricity.

At the anode, dihydrogen is separated to free up electrons:

$$H_2 \rightarrow 2H^+ + 2e^- \tag{2.1}$$

The PEM is permeable to protons, which are therefore able to cross it to reach the cathode.

There, they react with oxygen to create water:

$$\frac{1}{2}O_2 + 2H^+ + 2e^- \rightarrow H_2O. \tag{2.2}$$

Figure 2.1 (a) gives a 2-dimensional view of the structure of a fuel cell unit. The composition of the MEA, which is the subject of this dissertation, is detailed in Fig. 2.1 (b).

Although the basic functionality of a fuel cell is fairly simple, in practice several challenges arise to make sure that the cell produces a useful amount of current. These challenges are discussed in below.

Firstly, the reaction of hydrogen with oxygen needs to be catalyzed in order to proceed at a satisfying rate. This justifies the use of a Catalyst Layer (CL) inserted on each side of the membrane, acting as the electrodes.

Secondly, the reactants must diffuse over the entire area of the electrodes to maximize the reaction rate, and thus the current output of the cell. This is ensured by the use of Gas Diffusion Layers (GDL), through which the reactants are forced to diffuse before reaching the electrodes.

Thirdly, the PEM must be kept in a hydrated state in order to maximize its proton conductivity. However, since water is created as a product of the reaction, eventually flooding might happen at the cathode. This has the effect of blocking the access of reactants to the active parts of the cell, diminishing the reaction rate. Therefore, water management solutions should be implemented within the cell. The GDL and the bipolar plates are responsible for water management.

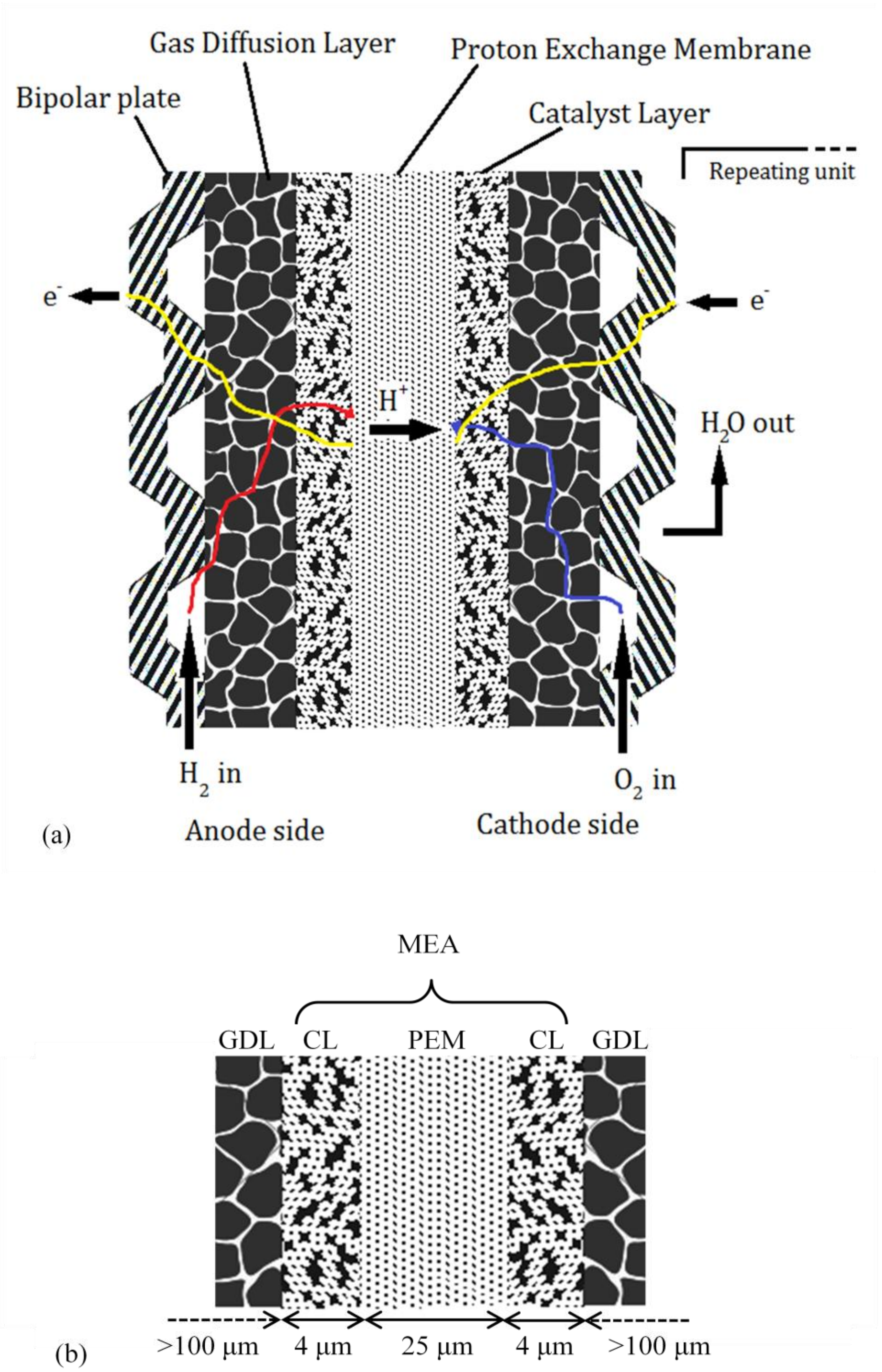

Fig 2.1 (a) Structure and function of a PEMFC unit; (b) Close-up on the Membrane Electrode Assembly (MEA)

Fourthly, the reaction is exothermal, which means the fuel cell must be equipped with thermal managements systems in order to prevent overheating. In general, thermal management is done with cooling fluids within the bipolar plates. The rate of the reaction increases with temperature, so it is advantageous to keep the temperature at a minimum of 80ºC.

Finally, even with all the previous conditions verified a single fuel cell will only output less than a volt. In order produce useful voltage, cells are organized in stacks. Practically, dozens or hundreds of fuel cells units are serially connected through their bipolar plates. Because of this, the current of each cell is the current of the whole stack. While this has the advantage of increasing the current additionally with each cell added, making it possible to output arbitrarily large amounts of current, another consequence is that the malfunction of any individual cell will decrease the output of the entire stack. This makes the question of the durability of each cell unit of particular importance.

The following sections of this chapter discuss the specific structure and requirements for each of the four components of a fuel cell.

2.2. Proton Exchange Membrane

Proton Exchange Membranes give their name to PEMFCs, as they are their core component. The fundamental requirement of the PEM is that it must be able to conduct protons while acting as a barrier for electrons. Another constraint is to limit gas crossover, thus preventing reactants to reach the opposite electrode. Aside from that, PEMs must be able to operate in the conditions of temperature and humidity met by fuel cell without losing their properties.

By far the most widely used material for the PEM is Nafion[59], which is the reason why this is the material upon which this study focuses on. It is produced and sold by the company DuPont™ in a variety of forms, although its chemical structure, shown in Fig. 2.2, stays the same. The specific model used in this study is Nafion NR211, which comes in sheets 25µm thick. This model is the one used in modern fuel cells.

Protons on the SO_3H groups can be transmitted from one acid site to another. Pores allow movement of cations but the membrane does not conduct anions or electrons, which makes Nafion an ideal material to use in PEMFC. The CF_2 chains act as a backbone that gives Nafion its mechanical integrity. These chains are hydrophobic. The sulfonated side chains on the contrary are hydrophilic, and are prone to form clusters in a wet environment. Eventually when enough water is added, these clusters percolate, facilitating the transfer of protons through the membrane. This property is the reason why the proton conductivity of Nafion increases with humidity.

Nafion exhibits non-linear viscoplastic behavior and is very sensitive to changes of temperature, humidity or strain rate. All these parameters have to be taken into account during modeling.

2.3. Catalyst Layer

Catalysts layers are the electrodes located on each side on the PEM, and act as the siege of the oxydo-reduction reaction. Their main function is to catalyze the reaction up to an acceptable rate. Because catalyzation requires the use of noble metals (typically Platinum), CLs are the most expensive individual components in a fuel cell unit. In practice, they have to meet the following requirements: allow access of the reactant gases to the catalyst particles, allow good activation of these particles, and be electrically conductive (in order to collect the electrons freed by the reaction and transmit them to the GDL). From a structural point of view, they should adequately bond to the PEM (so that the protons freed at the anode can then migrate to the cathode). Bonding to the GDL is not required as long as water evacuation is ensured. For this reason, the most common method of fabrication for the CLs is to deposit them directly on the PEM, and to simply compress the GDLs onto the resultant MEA. The CL should be rigid enough to not deform into the pores of the GDL, as this could cause cracks to form on the surface of the CL[60].

2.3.1. Fabrication and structure of the catalyst layer

Since the cost of the CL, and by extension that of the entire fuel cell stack, is heavily dependent on the amount of Platinum used, a lot of efforts are being made to reduce the Pt-loading as much as possible without compromising the efficiency of the cell. Since an ideal solution has yet to be found (proposed solutions are often a compromise between cost and efficiency), the exact structure and mode of fabrication can vary from one CL to the other. However, since the requirements for the CL are rather specific, some characteristics overlap between all kinds of CLs. Below is the description of the CLs that were used in this study.

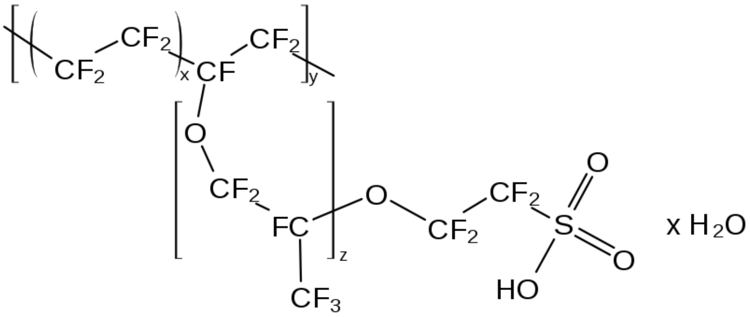

Fig. 2.2. Chemical structure of Nafion

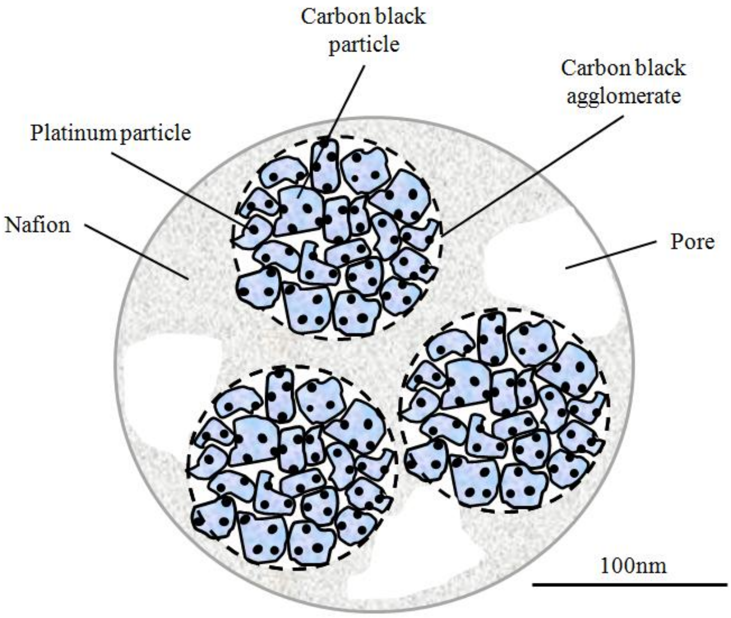

Fig. 2.3 Structure of a catalyst layer

The catalyst layer has to be based on ionomer material, which allows to collect the protons as well as to bond the layer to the PEM. This ionomer is filled with electrically conductive material, typically a type of carbon black. The ratio of carbon black has to be sufficient to percolate to ensure that the CL stays electrically conductive. The carbon black serves a double purpose, as it is also used as a backbone to deposit catalyst particles, which is much more economical than using solid catalyst clusters. Different strategies exist to maximize the activation of the catalysts. Depending on the exact type of carbon black used, the size and shape of the cluster will vary; for the purpose of maximizing the active area of the CL it is preferable that the carbon clusters be as dendritic as possible. As for the catalyst particle themselves, earlier fuel cells simply deposited platinum or platinum alloy particles on the carbon black, recently a more promising approach has been to use core-shell type catalysts, where the catalyst particle, spherical in shape, only has its outer layer coated in Platinum, while its core is made of other, cheaper materials. This approach has the advantage of reducing the quantity of Platinum needed without changing the active area of the catalyst particles.

The carbon black, onto which the catalyst particles have been deposited, is then mixed with solvent to form a catalyst ink, and then added to the ionomer. The CL is now ready to be deposited on the PEM.

For the specific CLs that were used in this study, catalyst ink was prepared by mixing 60 wt% Pt/C and coated on a Teflon sheet with a Pt loading of 0.2mg/cm^2. The formed catalyst layers were then transferred to both sides of the Nafion using the heat press method at 15MPa and 130°C for 10 minutes, followed by 3MPa and 130°C for 4 minutes. The resulting CL is measured to be approximately 4μm thick.

The structure that emerges as a result of this fabrication process is highly irregular. The carbon black aggregates in cluster 100 to 200nm in diameter, and are decorated with Platinum particle approximately 5nm in diameter. As a result of the solvent evaporating, pores are also present within and around carbon clusters. Pores may limit the access of reactants to the catalysts, and they are also susceptible to collect liquid water, risking flooding the electrodes. Therefore, it is advantageous to limit their quantity and size. Figure 2.4 displays a scanning electron microscope observation of the surface of one of the CLs used in this study. The resolution obtained at a 20,000 times magnification allows to see the carbon black particles and the highly porous structure; however it is not enough to distinguish the Platinum particles. The presence of pores can lead to initial defects in the structure, with a size of generally less than a micrometer, as can be seen in Fig. 2.4.

Huang et al. [61] observed catalyst layers under a transmission electron microscope and reported a composition in volume of 43% of Carbon/Platinum agglomerate, 27% of ionomer and 30% of pores. Fig 2.3 gives a representation of the structure of a typical CL, which is corroborated by the actual visualization of a CL made by Huang et al.

2.4. Gas Diffusion Layer

Gas diffusion layers are located on each side of the MEA, compressed between the catalyst

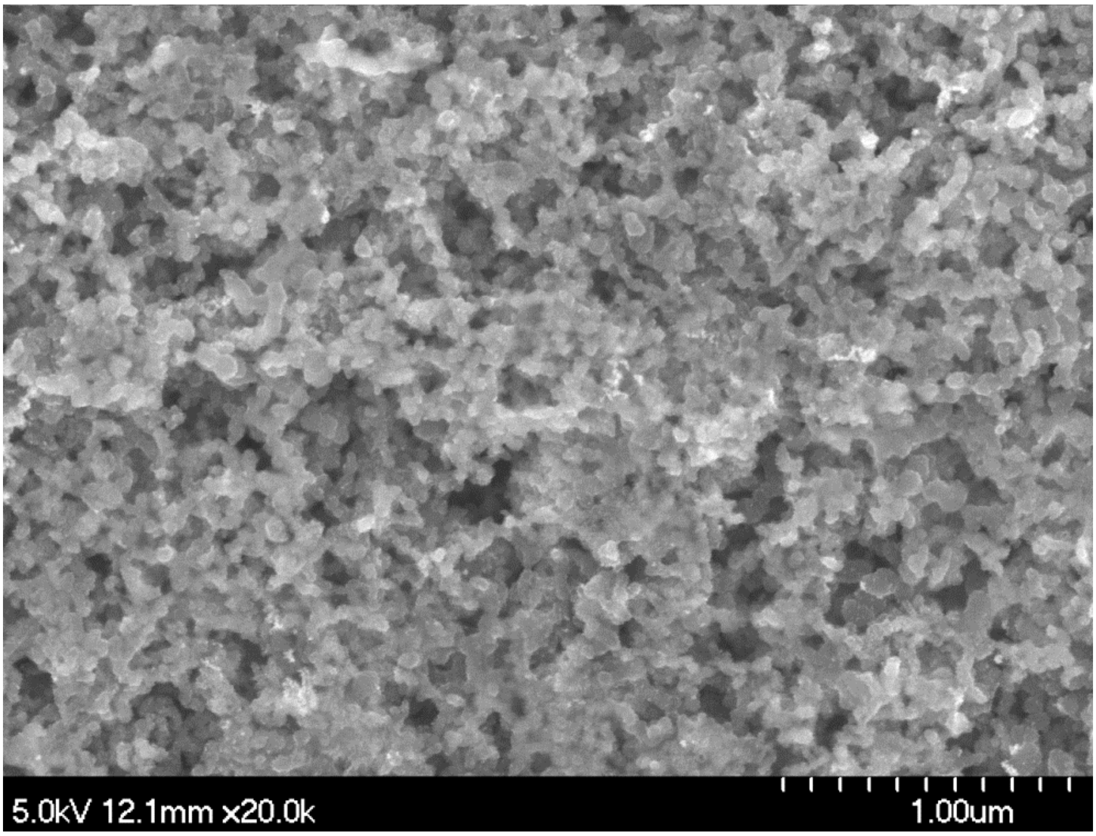

Fig. 2.4 Scanning electron microscope observation of the surface of the CL in as-received MEA sample

layers and the bipolar plates. As indicated by their name, their main function is to provide an adequate media for gas diffusion from the bipolar plates to the active zone of the cell. Gas diffusion layers allow the reactant gases from the inlet channels to reach the entire reactive area of the cell. Otherwise, the gases could only access the parts of the CL directly opposite the inlet channels, which would not be efficient. Meanwhile, the GDL also allows the water created at the cathode to evacuate the active zone of the electrode by diffusing through the GDL by capillarity, thereby preventing the flooding of both the cathode and of the inlet channels. The final role of the GDL is to allow electrons to transit to and from the bipolar plates that act as current collectors.

Therefore, the requirements for the GDL are as follows: the layer should be permeable to reactant gases and water, and efficiently conduct electron and heat (as heat is produced at the electrodes and the cooling mechanisms are in the bipolar plates). From a mechanical perspective, it should provide support to the MEA and prevent it to deform and creep. In particular if the pores of the GDL are too large, there is a risk that the MEA will buckle into these pores and crack[60]. The GDL itself should be rigid enough to not deflect into the channels of the bipolar plates, which could result in a pressure drop inside the cell[62]. Some of these requirements are contradictory: while ideally gases would diffuse better through an empty medium, such a solution would not be able to support the MEA and would stop the transit of electrons.

When it comes to assembly of the fuel cell, there are two strategies for the GDL: either the catalyst layer is deposited on the GDL, forming what is called a gas diffusion electrode, which are then applied on each side of the PEM; or the catalyst layer is deposited on the PEM first, forming the MEA, which is then compressed on each side by GDLs. This thesis, which focuses on the fracture resistance of the MEA, concerns the latter strategy.

There was a lack of data on GDL in the reviewed literature compared to other components of the fuel cell, due to the fact that the GDL is neither a source of durability problem (like the MEA) nor of voltage loss (like the bipolar plates). As a result, most studies on GDL are empirical. However, gas diffusion layers have been shown to play an important role for the cold start of the cell: the behavior of the gases in the GDL as they initially flow through the GDL, as well as the possible condensation that might arise as a result of blowing humidified air on the still-dry MEA have received some attention[63].

2.4.1. Materials

In practice, porous materials fill the structural requirements for the GDL. The material should have enough empty spaces that a porous network is formed, and at the same time the pores should be small enough to allow liquid water to transit through the GDL by capillarity. In order to facilitate the evacuation of water and limit liquid retention, the material should be either hydrophobic or be coated with a hydrophobic layer. Some researchers have proposed to purposefully design hydrophilic channels inside the GDL to further prevent water from flooding the electrodes. Since there is no standard way to manufacture GDLs, many have proprietary designs and materials. Their thickness is generally in the order of a hundred micrometers, that is, as thin as possible but still thick enough to ensure adequate diffusion of the gases and structural integrity. The GDL should be able to withstand some amount of compression forces and be rigid enough to not affect either the bipolar plates or the MEA.

Materials that fit these requirements are most often based on carbon fibers: their high porosity (>70%), good electrical conductivity and satisfying mechanical properties make these kinds of products ideal for use in the gas diffusion layer[64-67]. These materials are then teflonized to some degree in order to ensure hydrophobicity, and therefore better water management properties[68-70].

Recently, porous metals have been investigated as a less costly alternative to carbon fiber. For example, nickel-based GDL have been reported to offer decreased contact resistance with the CL and increased rigidity when compared to a carbon cloth[71]. However, most of the proposed porous metals require some coating material such as gold in order to prevent corrosion without decreasing electrical conductivity. Since such coatings are too expensive to use on a large scale, porous metals still need further progress in order to be competitive with carbon fibers for use in the GDL[72].

2.5. Bipolar plate

Bipolar plates, or more exactly bipolar flow field plates, are the outermost components of a fuel cell unit, and as such serve an important structural purpose to ensure the integrity of the cell. Their ‘bipolar’ designation comes from the fact that in a fuel cell stack, the same plate will be both on the anode side of a fuel cell unit and at the cathode side of the next unit. From the point of view of fuel cell functionality, bipolar plates have to collect electrons freed from the reaction, thus acting as a current collector. They provide an inlet for the reactants while also providing channels for the coolant fluids as well as for the evacuation of water. For these reasons, bipolar plates need to have good electrical and thermal conductivity with little gas crossover. Sealing structures are used on the extremities of the plates to prevent the leaking of reactant gases between the bipolar plate and the GDL. A variety of strategies exist in order to seal the cell, however at the time of writing there is not yet a standardized approach[73].

Since bipolar plates must act as a support for the rest of the cell, and since they provide different channels for several types of fluids, they are considerably thicker than the other components: bipolar plates are several millimeters thick while other components, the GDL and the MEA, have their thickness in the order of a few tenths of micrometers. Therefore, they make up the largest portion of the weight of a fuel cell, and so the density of the material chosen for the bipolar plate also comes under consideration. In general, the choice of the optimal material for a bipolar plate will be a compromise between performance and cost of fabrication.

As the bipolar plates are a structural component for the cell, and as they use materials that are stronger than for other components, the mechanical properties of bipolar plates are generally not a concern for the durability of the cell, and therefore are not well documented.

2.5.1. Geometry

The geometry of bipolar plates is the most complex among the components of a fuel cell, due to the different types of channel they must contain. As such, the manufacturing process can become a time and resource intensive task. Several approaches for designing the bipolar plates have been proposed, and research is still ongoing to find an optimal configuration. A good design is one that will facilitate the flow of reactants and water management for the cell.

Since the flow of gases inside of a fuel cell is pressure driven, the main mechanism for the transmission of reactants to the gas diffusion layer is diffusion. Therefore, it is necessary to maximize the contact area between the inlet channels and the GDL. On the other hand, contact between the bipolar plate and the GDL is important and necessary to provide good mechanical support for the rest of the cell, as well as to ensure electrical conductivity. As a general rule, the performance of the cell will improve with increased channel size (thanks to easier flow of reactants and water evacuation) until the points of contact with the GDL become insufficient to support the cell.

Other than increasing the surface area of the inlet channels to maximize diffusion of the reactant gases and water evacuation, another method is to design the bipolar plate so as to create a large pressure drop between the inlet and the outlet channels. In modern fuel cells, this is accomplished by creating serpentine flow fields[9,74]. The many switchbacks of the serpentine pattern allow for a better mixing of gases and a greater pressure drop than a simple straight channel design.

Another common method to increase gas flow to the GDL is interdigitation of the channel.

With this method, the inlet and the outlet are not a continuous channel; rather the gases are forced to pass through the GDL to get from one to the other in order to exit. In a conventional design, the gases would simply flow through the channel along the surface of the GDL and would only propagate to the GDL through diffusion. Another advantage of this type of design is that the force exerted by the flow of gases into the GDL is higher than by simple diffusion, and thus is more effective at pushing water out of the GDL[75,76].

In order to facilitate water evacuation, it is preferable that water be prominently in vapor phase. This is accomplished by ensuring that the partial pressure of water vapor in the channels stays below the saturation pressure of water. Since the capacity of air to absorb water increases with temperature, this is another reason why the temperature of the cell should be kept relatively high. Some amount of liquid water will accumulate regardless of the efforts to keep the partial pressure of water vapor low. In that case, it is important that liquid water stays in the form of small droplets so as not to obstruct the channels of the bipolar plate. For this reason, the cross-section of the channels presents sharp corners, which break the surface tension of water more efficiently than smooth channels.[9,76]

2.5.2. Materials

Because of the restrictions explained above, the range of materials suited for bipolar plates is somewhat limited. Following are the different materials that are typically used in the bipolar plates of modern fuel cells:

- Graphite: From a performance point of view, graphite is the ideal material to fill the role of bipolar plates. It has good electronic conductivity and is resistant to corrosion. It also has low density, meaning it allows for a very light weight fuel cell unit. However, its poor mechanical strength severely limits the options for manufacture, driving the costs high. Because of this, while the performance of graphite bipolar plates can be used as a benchmark to compare the performance of other materials, in practice they are restricted to research centers.[77-80]

- Carbon composites: As an attempt to harness the performance of graphite at a lower cost, composite materials using graphite and polymer resins are a popular alternative to pure graphite. Naturally, while a larger fraction of polymer resin will lower the cost and make manufacture easier, it comes at the price of a decreased conductivity. Different methods have been proposed to counteract this effect.[81-85]

- Stainless steel: As a metal, stainless steel has good thermal and electronic conductivities. Moreover, its low price and good mechanical strength means it is especially suitable for mass production. Among the available types of stainless steel, those with the highest corrosion resistance are preferred, since corrosion of the steel would lead to contamination of the rest of the cell by ions. This would poison the membrane, leading to the failure of the cell. In order to further decrease corrosion, coating the steel might be needed. Here, too, price is considered, ruling out materials such as gold, which would produce the best performance. Different coating materials have been proposed, typically metal oxides, nitrides and conducting polymers.[86-88]

- Other metals: Metals with low density and good electrical conductivity are also good contenders for use in bipolar plates; however they have the same limitation as stainless steel when it comes to corrosion resistance. Two metals that have excellent corrosion resistance thanks to their passivating oxide layer, titanium and aluminum, have been considered for being used in bipolar plates. However, the oxide layers of these metals are also insulating, meaning some conductive coating needs to be applied. This complicates the manufacturing process and drives the price up, and as a result stainless steel is the preferred material. Some research exists to develop metal alloys that would give even better performance with respect to both corrosion resistance and electrical conductivity.[85,89-96]

2.6. Summary

This chapter gives an in-depth discussion of the different components that are part of modern fuel cells, their functions and the constraints that they face. As has been mentioned several times throughout the chapter, at the conception level the choice of design and material for each component gives priority to the power generation aspect. It is only recently, as fuel cell technology has reached a point where the power output is sufficient to compete with other methods of power generation, that other considerations such as mechanical failure and durability have gained importance. Table 2.1 summarizes the different materials that are used and their main physical properties. For the PEM and the CL, these properties are discussed in more details in Chapter 3.

From the point of view of mechanical durability of fuel cells components, the following conclusions can be reached:

- Bipolar plates are the least affected by mechanical failure, due to the fact that they are made of rigid materials and do not have as much restriction on their thickness as other components. For this reason, they act as a support for the rest of the cell.

- Gas Diffusion Layers are designed to facilitate the diffusion of reactant gases and evacuation of water. Since this requires porous but rigid materials, typically based on carbon fiber, mechanical durability is not a major concern.

- The MEA is the component that is the most affected by mechanical degradation, which justifies the focus of this dissertation. Both the proton exchange membrane and the catalyst layer have strong requirements on the choice of materials that can be used. As a consequence, the materials of the MEA are ductile, very sensitive to variations of temperature and humidity and only a few tens of micrometers thick. The MEA is also constrained on both sides by the GDL, which causes compressive strains when the environmental conditions change. As a result, the MEA is the limiting factor when it comes to durability of the fuel cell. The following chapters will characterize this observation by introducing means of estimating the lifetime of the MEA.

Table 2.1 Summary of the main physical properties of the materials used in fuel cells

	Proton Exchange Membrane	Catalyst Layer	Gas Diffusion Layer	Bipolar Plate
Material	Nafion	Carbon Black/ Nafion	Teflon coated Carbon fiber	Graphite, Graphite composites, Steel
Thickness	25 µm	4 µm	>100 µm	>1 mm
Young's modulus (MPa)	30-260	126-174	>1000	>4000 (Graphite) >180000(Steel)
Poisson ratio	0.5	0.25	0.1	0.17-0.23 (Graphite) 0.3 (Steel)
Tensile strength (MPa)	23	3-8	150-380	5-76 (Graphite) >500 (Steel)
Coefficient of thermal expansion (K^{-1})	$1.23x10^{-4}$	$2\text{-}6x10^{-6}$ (Carbon black)	$1\text{-}10x10^{-6}$	$2\text{-}6x10^{-6}$ (Graphite) $10\text{-}18x10^{-6}$ (Steel)
Coefficient of hygrometric expansion ($\%RH^{-1}$)	$8\text{-}30x10^{-4}$	0 (Carbon black)	0	0

CHAPTER 3

Mechanical characterization and cyclic fatigue of the MEA: Experiment & Simulation

This study develops a numerical model to predict the failure criterion of the Membrane Electrode Assembly. The behaviors Nafion and the catalyst layer, the two materials making up the MEA, are first discussed. The fact that they respond differently to changes in temperature or humidity means that the behavior of the MEA as a whole will change qualitatively as the environmental conditions change. Tensile tests are performed in order to study the failure of the MEA. A shear-lag elastic plastic model as well as a finite element model is then developed to establish a failure criterion and to analyze the stress-strain constitutive behavior of the MEA. Finally, the finite element model is used to conduct a fatigue analysis of the MEA. This study should provide a better understanding of the mechanical behavior of the MEA as well as a way to include the failure of the components in future models.

3.1. Mechanical characterization of the MEA

3.1.1. Mechanical characterization of Nafion

Although Nafion has been widely studied, there is a lack of data concerning its material properties. The high sensitivity of Nafion to its surrounding temperature and humidity, to the strain rate, to the possible pre-treatment that was applied prior to the experiment, and the presence of hysteresis make it difficult to gather the necessary data on Nafion at the conditions that are relevant to this study. For this reason, the mechanical properties of Nafion were investigated using a simple unidirectional tensile test.

3.1.1.1. Testing Protocol

Tensile tests were conducted using the program LabVIEW developed by the company National Instrument (NI). This program allows to transmit a displacement and a displacement rate to a controller connected to the computer. The controller used was of the model GSC-02, developed by the company Sigma Koki. The controller actuated two stages, to the ends of which the specimen was clamped. Stages were of the model SGSP26-100, also developed by Sigma Koki. The ends of the stages were coated with rubber so as to catch the specimen without slipping. The stress applied to the membrane was measured using a load cell situated on one of the stages. Measurements from the load cell were visible on a connected oscilloscope. The model of the load cell was LUX-B-ID1, manufactured by the company Kyowa, while the oscilloscope was the model DL850 from Yokogawa Meters and Instruments. The surface of the membrane was observed using the Motion analyzing Microscope VW6000 from Keyence with VH-Z100UR lenses. Images were recorded at a rate of 30 frames per second and a shot speed of 1/60 second.

In order to control the environment, a custom environmental chamber was used. Temperature was controlled on both sides of the specimen, using a glass heater (model S-101(AC100V250W) from the company Blast) on the up side and a temperature control unit SCR-SQ from the company Sakaguchi on the bottom side. Humidity was controlled using an injection hose and a gauge me-40ADP-SRZ from the company Micro Equipment (ME). No pre-treatment was applied to Nafion before the tensile test. The experimental setup is described in Fig. 3.1.

Tests were performed for temperatures of 25°C, 40°C, 60°C, 80°C and 90°C, and for humidities of 20%, 50% and 80%RH, for a total of 15 different sets of parameters. Specimens were applied a constant strain rate of $0.0025s^{-1}$, and tests were repeated five times for each set of parameters. Strain was continually applied until rupture, which corresponds to the ultimate elongation of Nafion.

3.1.1.2. Experimental results

Given a constant strain rate, Nafion can be approximated by an elastic-plastic model, as shown in Fig. 3.2, along with an idealized rheological representation of this model and its relevant parameters. These parameters are the Young's Modulus E, the hardening coefficient H, and the yield stress σ_Y. To the yield stress a yield strain corresponds, ε_Y; this defines the yield point of Nafion. Every one of these parameters depends on both the temperature and the humidity. Knowing these parameters, the constitutive equation can be written as follow for uniaxial constraints:

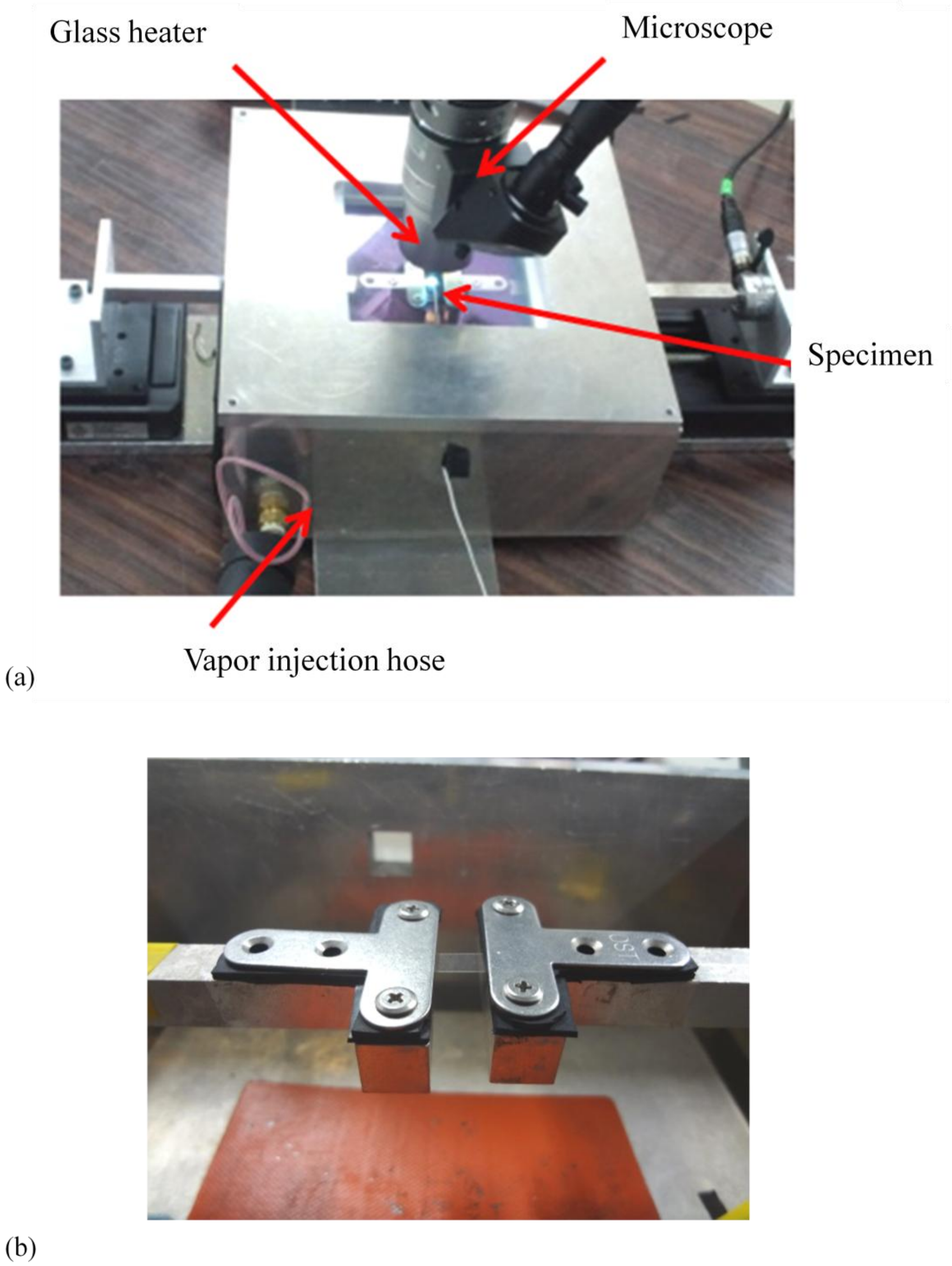

Fig 3.1 Experimental setup for characterization of Nafion: (a) Overview; (b) Close-up of the gripping mechanism

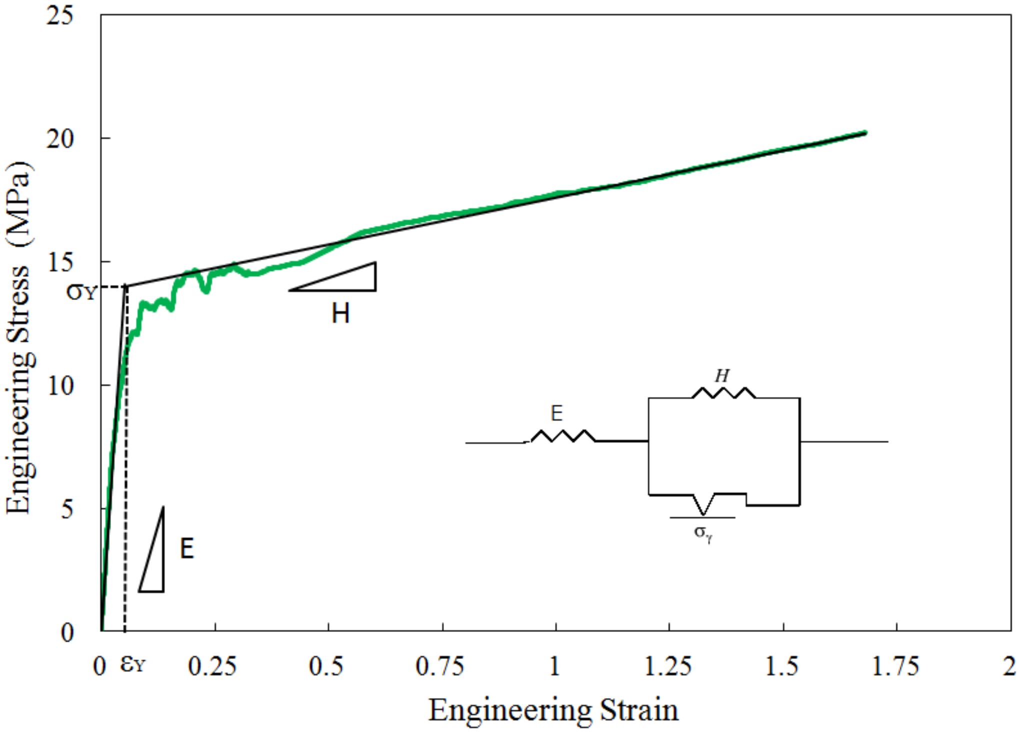

Fig 3.2 Elastic-plastic model for Nafion NR211 at 25°C, 20%RH. Insert: 1-D rheological representation of the elastic-plastic constitutive model

$$\begin{cases} \sigma = E\varepsilon & if\ \sigma \leq \sigma_Y \\ \sigma = E\varepsilon + H(\varepsilon - \frac{\sigma_Y}{E}) & if\ \sigma > \sigma_Y \end{cases} \tag{3.1}$$

The experimental values of the Young Modulus, hardening coefficient, yield stress and yield strain are synthetically summed up in Fig. 3.3, Fig. 3.4, Fig. 3.5 and Fig. 3.6 respectively. These are the mean values calculated from the series of experiment, with the error bars representing the standard deviation across the different specimens. These results stand for a strain rate of $0.0025s^{-1}$. It should also be borne in mind that the standard deviation for these values might be large: depending on the cases it might represent a deviation of 5-20% from the mean value. This large scattering of the data is the reason why the results found from one study to the other differ so much.

The relationship between the environment and the mechanical parameters of Nafion is complex. As a general trend, higher temperatures lead to higher yield strain and lower yield stress in Nafion. The Young Modulus and hardening coefficient are also decreased. This can be explained by the fact that Nafion undergoes a thermal transition which can be assimilated to a glass transition (or an order-disorder transition) in this range of temperature, and thus becomes more compliant. Higher humidities have the same effect, but for different reasons: as Nafion absorbs water and swells, the plasticizing effect of water, by weakening the intermolecular forces, makes the stiffness decrease. However, in the range of humidities tested, temperature seems to have a more clearly visible effect on the properties of the membrane than humidity.

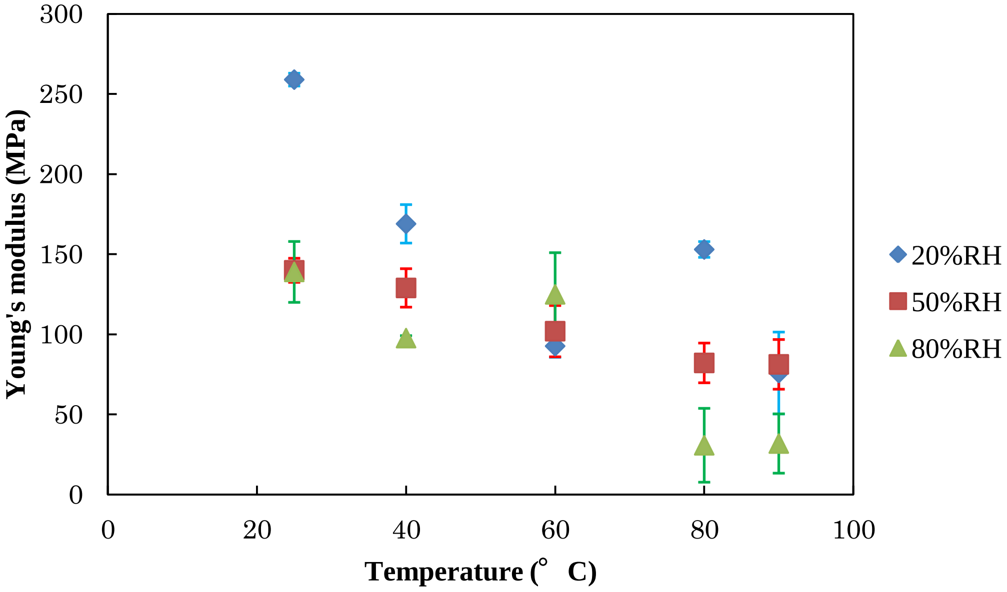

Fig. 3.3 Young’s Modulus of Nafion NR211

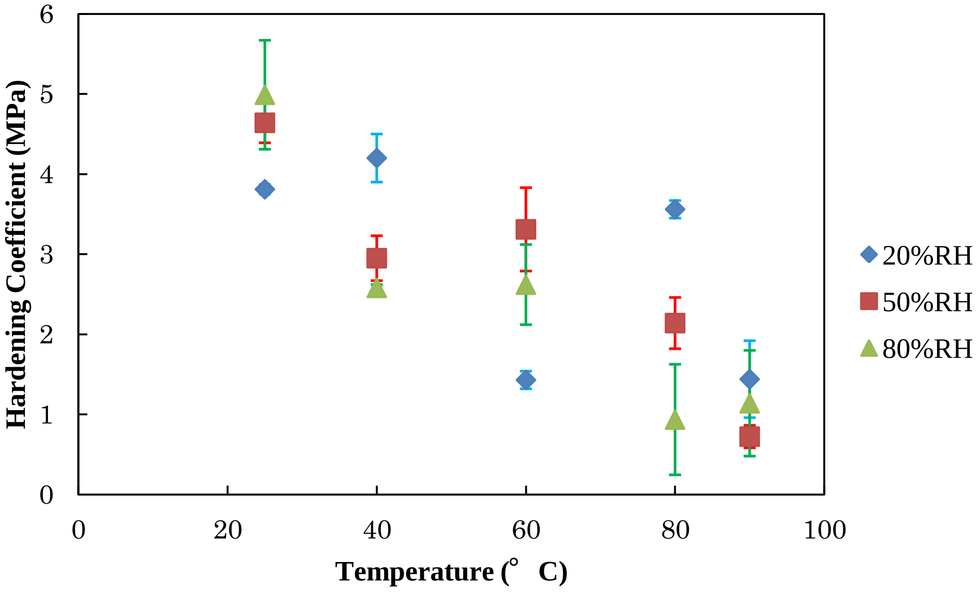

Fig. 3.4 Hardening coefficient of Nafion NR211

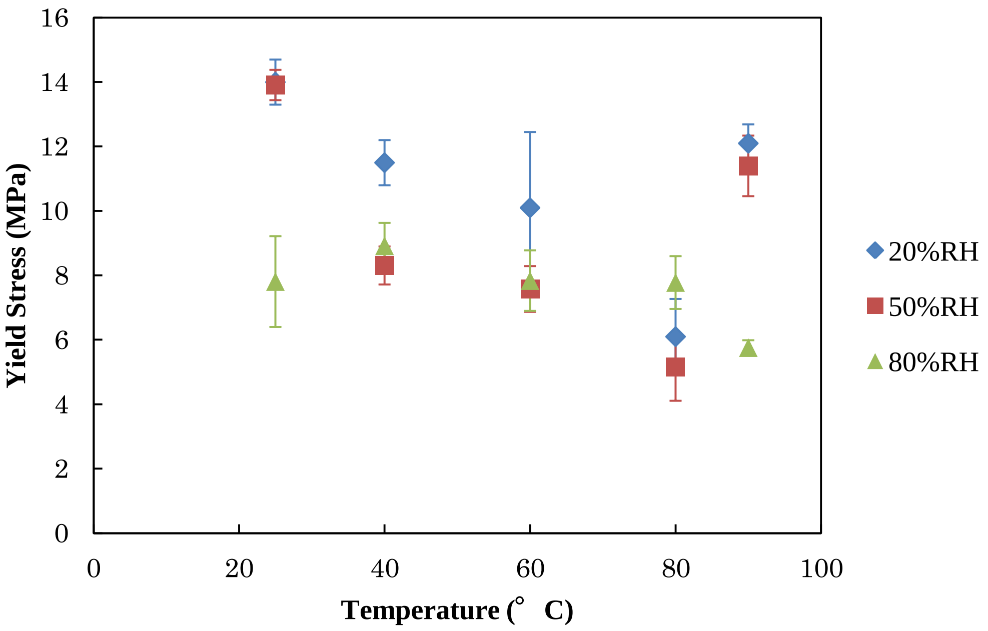

Fig. 3.5 Yield stress of Nafion NR211

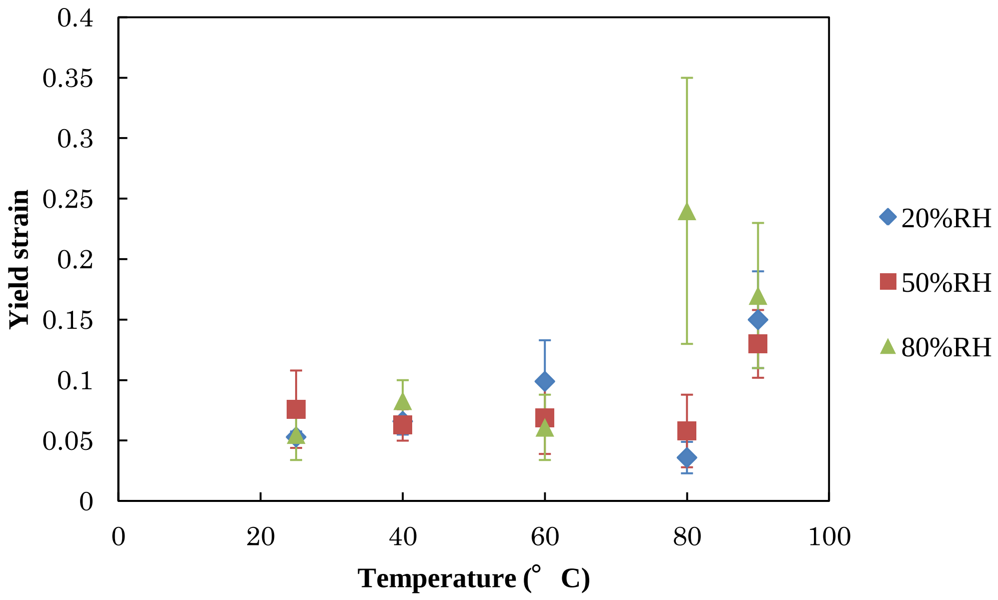

Fig. 3.6 Yield strain of Nafion NR211

3.1.1.3. Two-layer viscoplastic model

The mechanical characterization of Nafion discussed in the previous section considers the effect of temperature and humidity on its mechanical characteristics, but not the effect of strain rate. Even as a simplified model it is necessary to take these three parameters into account in order to get a useful approximation on the behavior of Nafion. Therefore, the previous model is improved by adding a time-dependant element to it.

This is accomplished by using a two-layer viscoplastic model. This model consists of the superposition of a linear elastic-plastic model with isotropic hardening and a perfect viscoplastic model following the Norton-Hoff laws. A one-dimensional idealization of this model is presented in the insert of Fig. 3.7. The total stress σ is divided into two components: the stress in the elastic-plastic network σ_P, and the stress in the elastic-viscous network σ_V, so that

$$\sigma = \sigma_P + \sigma_V \tag{3.2}$$

σ_P is calculated in the same way as in Eq.(3.1):

$$\begin{cases} \sigma_P = K_P \varepsilon & \text{if } \sigma \leq \sigma_Y \\ \sigma_P = K_P \varepsilon + H'(\varepsilon - \dfrac{\sigma_Y}{K_P}) & \text{if } \sigma > \sigma_Y \end{cases} \tag{3.3}$$

Following the notation introduced in Fig. 3.7, K_P is the long term modulus, σ_Y the initial yield stress and *H'* the hardening parameter.

The viscous stress follows the Norton-Hoff rate law:

$$\sigma_V = A^{-\frac{1}{n}} \dot{\varepsilon}^{\frac{1}{n}} \tag{3.4}$$

where *A* and *n* are fitting parameters and $\dot{\varepsilon}$ is the strain rate.

Since the linear elastic-plastic part of the model is the same as the model used to approximate Nafion in the experimental part of the study, the parameters were chosen according to the values already established in the previous section.

The experiments only investigated one strain rate, however in order to determine the parameters for the viscoplastic model it was necessary to rely on two previous studies which performed tests on Nafion at different strain rates[48,52]. In order to implement the two-layer model in the finite element software ABAQUS, three parameters are needed. The first two parameters, *A* and *n,* are fitting parameters for the calculation of the viscous stress. The last parameter, *f*, is defined as

$$f = \frac{K_V}{K_P + K_V} \tag{3.5}$$

and represents the ratio of the elastic modulus of the elastic-viscous network (K_V) to the total (instantaneous) modulus (K_P+K_V).

Using Eq. 3.4, and two strain rates $\dot{\varepsilon}_1$ and $\dot{\varepsilon}_2$ such that $\dot{\varepsilon}_2 = 10\dot{\varepsilon}_1$, we get the relation

$$\frac{\sigma_{V,2}}{\sigma_{V,1}} = \left(\frac{\dot{\varepsilon}_2}{\dot{\varepsilon}_1}\right)^{\frac{1}{n}} = 10^{\frac{1}{n}} \tag{3.6}$$

The plastic and viscous network being independent, the total stress is the sum of the stress in the plastic network and in the viscous network. Thus, at yield, it is possible to write

$$\sigma = \sigma_Y + \sigma_V \tag{3.7}$$

Here, σ_Y is the static yield stress, that is, the theoretical yield stress at a strain rate $\dot{\varepsilon} = 0s^{-1}$. It is possible to measure this stress by submitting Nafion to a strain high enough to produce yield, and then let it relax for a long time. The equilibrium stress is the static yield stress. This was done in Ref. [48], and the static yield stress was found to be $\sigma_Y = 3.5MPa$. That experiment was done at 25°C and 50%RH, and by default of other data this static yield stress is assumed to be independent of the environment. The viscous stresses observed in the two mentioned studies are summed up in Table 3.1.

Table 3.1. Viscous strain at different strain rates

[48] (25°C, 50%RH)		[52] (25°C, 30%RH)	
$\dot{\varepsilon} = 0.00023s^{-1}$	$\sigma_V = \sigma - \sigma_Y = 4.0MPa$	$\dot{\varepsilon} = 0.001s^{-1}$	$\sigma_V = 4.5MPa$
$\dot{\varepsilon} = 0.0023s^{-1}$	$\sigma_V = 6.5MPa$	$\dot{\varepsilon} = 0.01s^{-1}$	$\sigma_V = 7.0MPa$
$\dot{\varepsilon} = 0.023s^{-1}$	$\sigma_V = 9.5MPa$	$\dot{\varepsilon} = 0.1s^{-1}$	$\sigma_V = 9.5MPa$
$\dot{\varepsilon} = 0.23s^{-1}$	$\sigma_V = 12.0MPa$		

Using the values of Table 3.1 with Eq.(3.6), the following values of *n* are obtained:

$$\left.\begin{array}{ll} n = 6.24 & at\ 25°C, 50\%RH \\ n = 6.08 & at\ 25°C, 30\%RH \\ n = 6.17 & \quad overall \end{array}\right\} \tag{3.8}$$

The overall value was selected for the viscoplastic model.

Having determined *n*, the value of *A* can be calculated with the following equation:

$$A = \frac{\dot{\varepsilon}}{\left(\sigma - \sigma_Y\right)^n} \tag{3.9}$$

Using the values found in earlier for a strain rate $\dot{\varepsilon} = 0.0025 s^{-1}$, the values of *A* were calculated so as to fit the experimental observations. They are given in Table 3.2.

Table 3.2. Calculated values of the parameter A

	20%RH	50%RH	80%RH
25°C	1.19×10^{-46}	1.2×10^{-46}	2.91×10^{-44}
40°C	6.4×10^{-46}	1.48×10^{-44}	7.07×10^{-45}
60°C	2.1×10^{-45}	4.08×10^{-44}	2.78×10^{-44}
80°C	6.57×10^{-43}	1.0×10^{-41}	3.03×10^{-44}
90°C	4.09×10^{-46}	6.91×10^{-46}	1.56×10^{-42}

Finally, the parameter *f* was determined in order to fit the experiment with the best possible accuracy. The value that was selected was $f = 0.6$.

The model was tested using all the parameter thus defined, and was found to fit the experiment reasonably well, as exemplified by Fig. 3.7. The model is especially accurate at both low and medium strains (an engineering stress of 0.9 corresponds to a true strain of approximately 0.64), while slightly overestimating the stress around the yield point. The range of strain relevant to the study of the fatigue of the MEA being low (the cracking of the CL typically happening before yielding of Nafion), that model was considered satisfying for the purpose of the study.

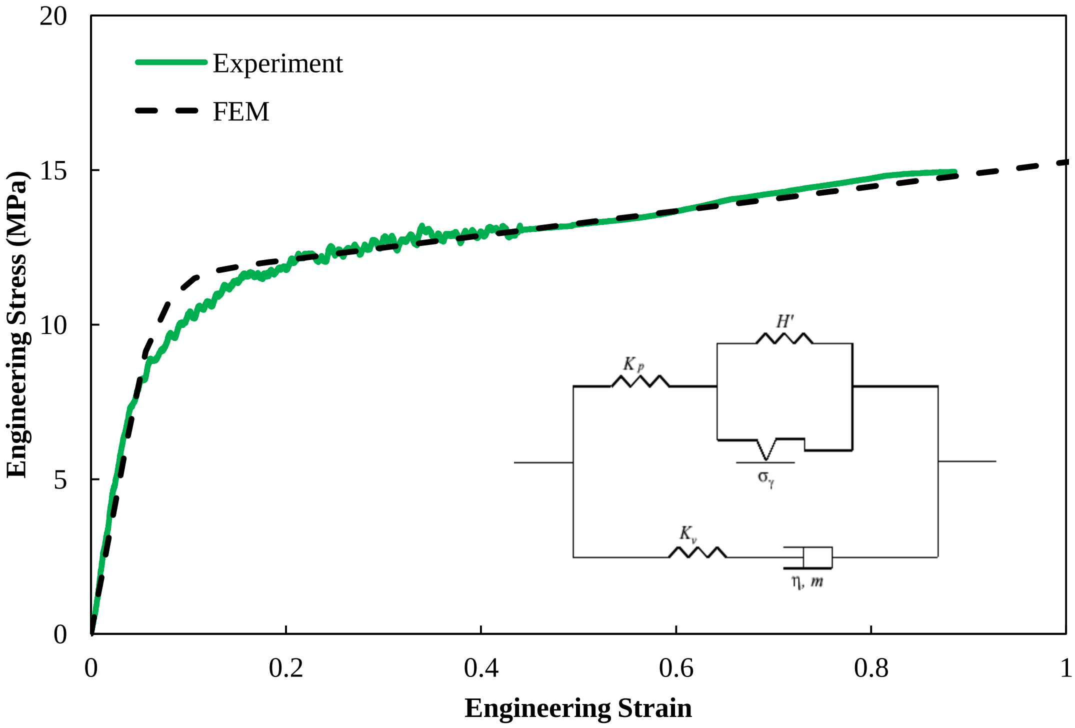

Fig 3.7 Two-layer viscoplastic model for Nafion NR211 at 40°C, 20%RH. Insert: 1-D rheological representation of the two-layer viscoplastic constitutive model

As a last remark concerning the two-layer model, it has been reported in other studies that it deviates from the experiment at extreme strain rates (either very low or very high). Nevertheless, the model is accurate for strain rates ranging for $10^{-4}s^{-1}$ to $10^{-1}s^{-1}$. In order to investigate the behavior of the MEA past this range, it should be necessary to add a correction to the two-layer model.

3.1.2. *Mechanical characterization of the CL*

The catalyst layer is assumed to behave following an elastic-plastic constitutive equation. This equation is analog to Eq.(3.1), with the different parameters (Young's modulus, hardening coefficient, yield stress) fitted to experimental behavior.

$$\begin{cases} \sigma = E_{CL}\varepsilon & if\ \sigma \le \sigma_{Y,CL} \\ \sigma = E_{CL}\varepsilon + H_{CL}(\varepsilon - \dfrac{\sigma_{Y,CL}}{E_{CL}}) & if\ \sigma > \sigma_{Y,CL} \end{cases} \tag{3.10}$$

Because of the thinness of the catalyst layer, it is not possible to isolate it to perform tensile experiments. As a consequence, CLs were tested indirectly by comparing tensile results on MEA with results for Nafion membranes alone. The mechanical properties of the CL were estimated using the following equation:

$$E_{CL} = \frac{E_{MEA}t_{MEA} - E_N t_N}{2t_{CL}} \tag{3.11}$$

where the indices MEA, N and CL represent the assembly, the Nafion layer and the catalyst layer respectively; *E* is the Young's Modulus and *t* the thickness of the respective layers. Similar equations were used for other parameters by substituting the Young’s Modulus for the hardening coefficient or for the yield stress. These parameters are enough to develop an elastic-plastic model for the catalyst layer. The difficulty of performing mechanical experiments on the CL alone makes it particularly challenging to gather other data on the properties of the CL. There has been at the present time no published model to predict the large scale behavior of this layer, other than the simple elastic-plastic model.

The testing protocol for testing the MEA is the same as the one for testing Nafion, and is described in section 3.1.1.1.

Temperature was found to not have any visible impact on the properties of the CL, so only the dependency to the humidity is here presented. Values retained are summed up in Table 3.3.

Table 3.3. Properties of the catalyst layer at different humidities

Humidity	20%RH	50%RH	80%RH
Young Modulus (MPa)	174.1	131.8	126.1
Hardening coef. (MPa)	0.936	0.957	1.059
Yield stress (MPa)	6.24	6.38	7.06
Yield strain	0.036	0.049	0.056

The effect of humidity is here better visible than for Nafion. Higher humidities lead to lower Young’s modulus, but higher hardening coefficient, yield stress and yield strain.

It is worth noting that yielding of CL always happen before yielding of Nafion. Also, while Nafion is stiffer than the CL at ambient temperature (25°C), this is reversed at higher temperatures. Another remark is that Nafion is much more compliant under hardening than the CL, as is shown by the difference in the hardening coefficients.

Poisson's ration was chosen, based on previous studies, to be $\nu_{CL} = 0.25$. This has the effect to introduce a mismatch between the Poisson's ratios of the layers, resulting in additional transverse strains. Owing to its higher Poisson's ratio Nafion will deform more transversally than the CL, as a consequence the stress in the CL will be increased.

3.2. Onset of failure in the MEA

3.2.1. Experimental procedure

The experimental apparatus that was used for the fatigue tests is the same that the one used for the tensile tests described in Section 3.1.1.1: the tests were conducted using a tensile machine and an environmental chamber, while the surface of the CL was observed using a microscope, as depicted in Fig. 3.1

The MEAs that were used in this study were made of Nafion, with catalysts layers applied on both sides. The mode of fabrication of the CL, as well as the method to apply it to Nafion, is given in details in Section 2.3.1. For the purpose of the experiment, specimens to be tested were cut to dimensions of 25 mm x 5 mm.

Figure 3.8(a) shows a characteristic view of the surface of the CL before the tests. The

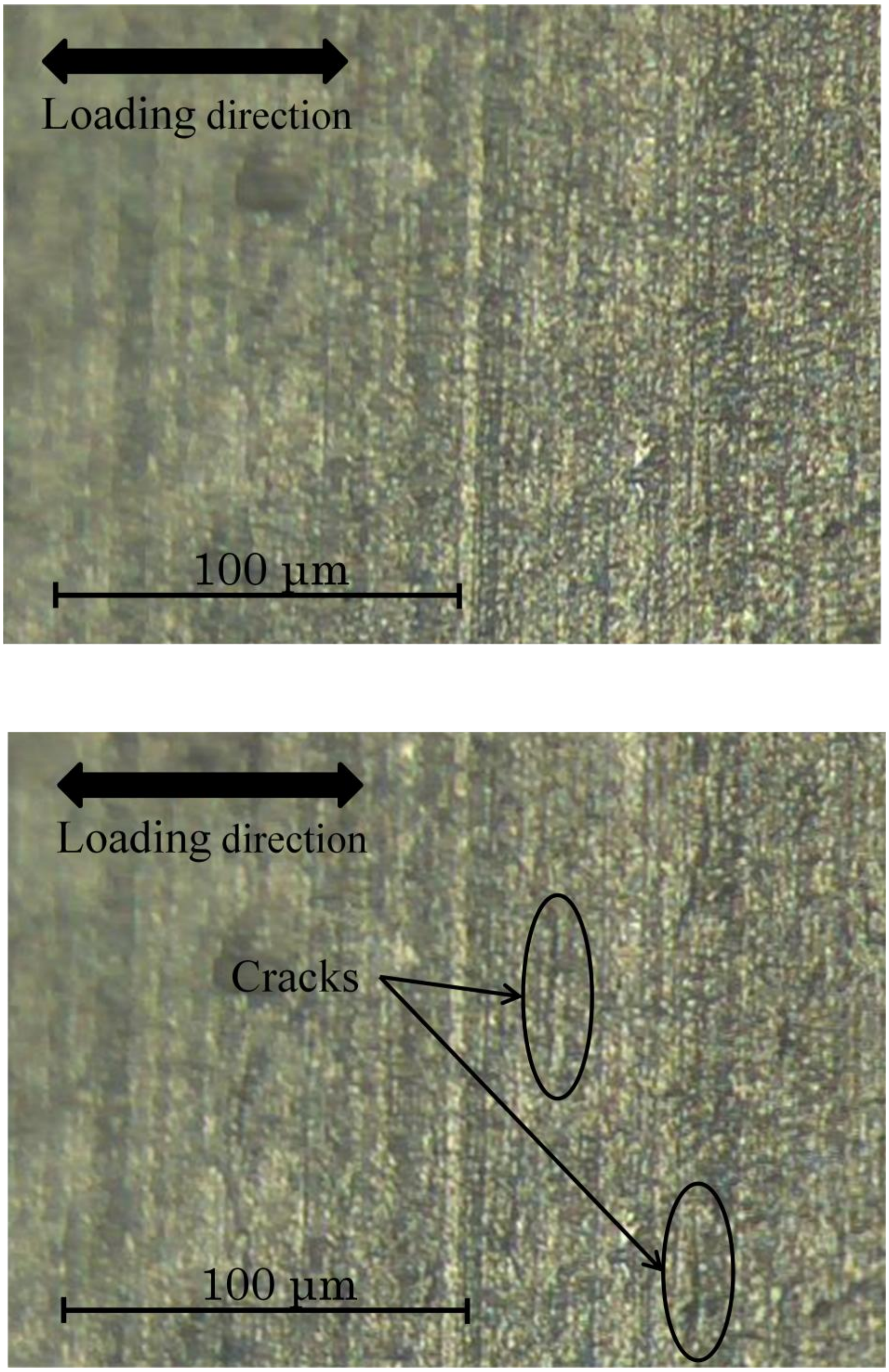

Fig.3.8. Observation of the surface of the CL in MEA sample: (a) as-received; (b) apparition of cracks on the surface

surface roughness was visible on the surface of MEA due to the heat press method, but it did not affect the crack initiation and propagation during tensile and fatigue tests.

Tests were performed for temperatures of 25, 40, 60, 80 and 90 °C, and for humidities of 20, 50 and 80 %RH, for a total of 15 different sets of parameters. Specimens were applied a constant strain rate of 0.0025 s^{-1}, and tests were repeated five times for each set of parameters.

A second set of experiments was performed at 25°C and 50 %RH, in order to test the fatigue behavior of the MEA. Two strain rates were tested, namely 0.0025 and 0.025 s^{-1}, at plastic strain ranges of 0.01 to 0.04. A regression analysis was then realized in order to derive a Coffin-Manson type law, linking the amplitude of plastic strain to the number of cycles to failure.

3.2.2. Shear-lag model

The shear-lag model is designed to predict the crack behavior of a brittle thin film over a polymer subsrate submitted to tensile strains, and thus applies to the case of the MEA. It links the transmission of shear stress from the substrate to the thin film, to the observed crack distribution on the film. Derivation of the relationship can be found in other studies[97]. The material parameters, the crack density and the critical strain are linked as follow:

$$n = \sqrt{\frac{E_N}{3E_{CL}}}\left[2\sqrt{t_N t_{CL}}\,\arg\cosh\left(\frac{1}{\frac{\sigma *}{\varepsilon E_{CL}} - 1}\right)\right]^{-1} \tag{3.12}$$

if the crack appears before the yield of Nafion, and

$$n = \frac{E_N \varepsilon_Y}{6E_{CL}t_{CL}} \left[\left(\frac{\sigma^*}{E_{CL}} - \varepsilon \right) \cosh\left(\arg\sinh\left(\frac{\varepsilon_Y \sqrt{\frac{E_N t_N}{3E_{CL}t_{CL}}}}{\varepsilon - \frac{\sigma^*}{E_{CL}}} \right) \right) + \varepsilon + \varepsilon_Y \sqrt{\frac{E_N t_N}{3E_{CL}t_{CL}}} \arg\sinh\left(\frac{\varepsilon_Y \sqrt{\frac{E_N t_N}{3E_{CL}t_{CL}}}}{\varepsilon - \frac{\sigma^*}{E_{CL}}} \right) \right]^{-1} \tag{3.13}$$

if the crack appears after. n is the crack density, ε_Y the yield strain of Nafion, E the Young's modulus, t the thickness and the indices N and CL represent Nafion and the catalyst layer, respectively. The crack initiation stress is noted σ^*.

In order to calculate the crack initiation stress it is then necessary to apply an arbitrary strain and to calculate the corresponding crack density. A simpler approach is to apply the crack initiation strain, ε^*, established in the tensile tests. At this strain, n becomes strictly positive: for a specimen length of 25 mm, at ε^*, n can be said to be equal to 0.04 mm^{-1} after the first crack.

The major advantage of this model is its simplicity; however it assumes that the cracks appear before the yield of CLs. Because of this, the expected crack initiation strain calculated from this model cannot be relevant when this is not the case.

Further discussions of this model are given in [98]

3.2.3. FEM Analysis

Numerical models, and in particular the finite element method, are a convenient way to estimate the properties of a fuel cell or of its individual components; the alternative being systematic experiments, which are expensive, time consuming and require the use of multiple prototypes. Though some amount of experimental data is necessary to calibrate and validate the numerical models, this method still allows to save much valuable resources.

The commercial software ABAQUS was used to realize the finite element model. The first purpose of the analysis was to be able to accurately replicate the tensile experiment, so the model was created with the dimensions of the MEA used in the experiments. Because of multiple symmetries, only one eighth of the actual specimen had to be created. A view of the model is presented in Fig. 3.9.

Mechanical properties of both layers (Nafion and CL) were established according to the data found in the experiments. Missing properties were chosen according to previous studies, or, because of the lack of existing data, fitted to reproduce experimental results.

For Nafion, the two-layer viscoplastic model described in the previous chapter was used in order to account for the strong time dependant response of the polymer. This model consists of the superposition of a linear elastic-plastic model with isotropic hardening and a perfect viscoplastic model following the Norton-Hoff law. For the CL, linear elastic-plastic behavior was assumed.

The second step of the FEM analysis was to perform fatigue tests. For this purpose cyclic strain was applied to the model, in a range of amplitudes and strain rates. The aim of this analysis was to establish a failure criterion for the MEA during fatigue experiments.

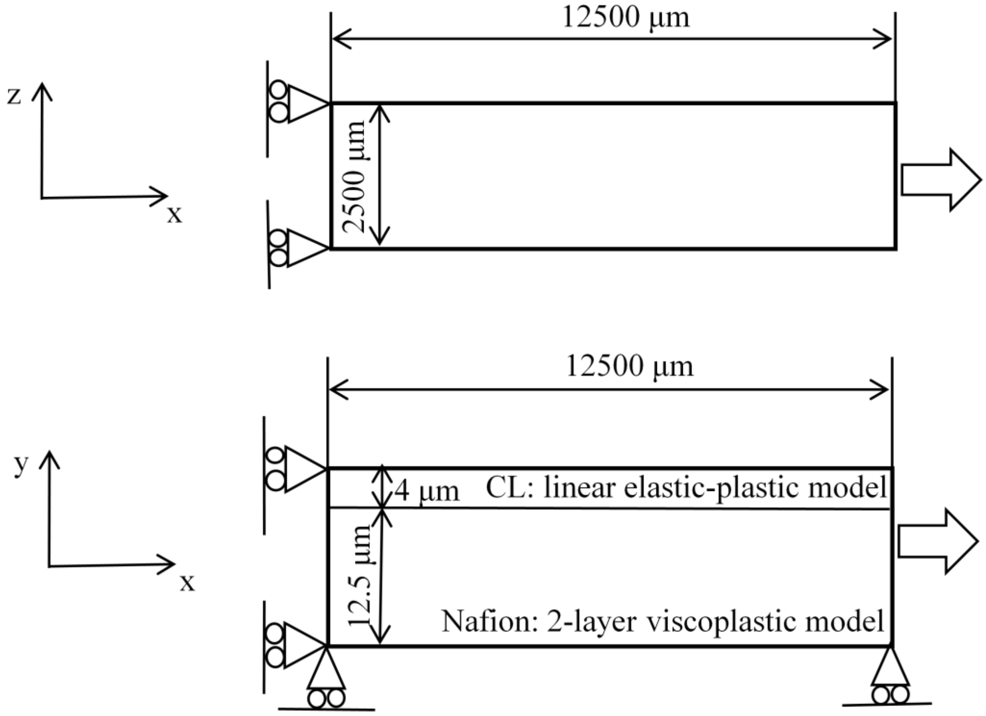

Fig.3.9. Overview of the Finite Element Model

3.3. Failure criterion of MEA

3.3.1. Failure criterion of MEA under static tensile loading

Failure of the MEA happens in several stages: cracks first appear, before widening and propagating; eventually the CL is entirely delaminated from the membrane. The stage relevant to this study is the crack initiation, and thus the failure criterion is defined by the apparition of the first crack in the CL. For a uniaxial tensile test, failure can be linked to an applied strain; however in a real situation the strain is likely to be multiaxial, so it is best to define the failure criterion using the local Mises stress at the time of failure. The Mises stress cannot be calculated from the experiment, and so was obtained via the FEM using the experimental crack initiation strain. This strain is shown in Fig. 3.10 for different conditions.

Temperature seems to have a greater effect on the crack initiation strain than humidity. This can be explained by the fact that as Nafion becomes more compliant, more stresses are transmitted to the CL. As temperature affects the stiffness of Nafion more than humidity, so is the case with crack initiation. Using this strain, the corresponding Mises stress was calculated in the numerical analysis. The predicted crack initiation stress from the shear-lag model was obtained by solving Equations 3.12 and 3.13 for σ^*. Equation 3.12 can be solved explicitly, but Equation 3.13 requires an implicit solution. The results for both the shear-lag model and the finite element model are compiled in Fig. 3.11.

As noted earlier, the shear-lag model is only accurate for cases where the crack initiation happens before yielding of the CL. This range can be seen by comparing the crack initiation strain shown in Fig. 3.10 with the yield strain of the catalyst layer from Table 3.3. The situations where the shear-lag model is valid are, for 50%RH: 60, 80 and 90ºC, and for 80 %RH: 40, 60, 80 and 90ºC. The reason for this limitation is that the model assumes a stiff film over a compliant substrate; however Nafion appears stiffer than the CL at low temperatures and humidities. As these parameters increase, Nafion becomes more compliant, thus satisfying the hypothesis. As can be seen in Fig. 3.11, in cases of high temperature and high humidity the results given by the two models are fairly similar. The FEM analysis has the advantage of having no limitation with respect to temperature or humidity. Another advantage is that this method can be adapted for failure prediction under dynamic loading, while the shear-lag model is limited to static loadings.

In the same manner as for the crack initiation strain, higher temperatures imply lower break stress, meaning that failure happens earlier in the test, while humidity does not have a great effect on the apparition of cracks.

These results indicate that temperature is the determining factor for estimating the durability of the MEA, whereas the humidity will not have an important effect on failure.

3.3.2. Failure criterion of MEA under cyclic loading

Investigating the behavior of the MEA under cyclic loading is of major importance for the study of reliability, because the MEA during normal function of a fuel cell will be subject to cyclic loading at strains not high enough to provoke failure in a single cycle, but high enough to induce fatigue of the material. In this study, the fatigue under ambient conditions (25ºC, 50%RH)

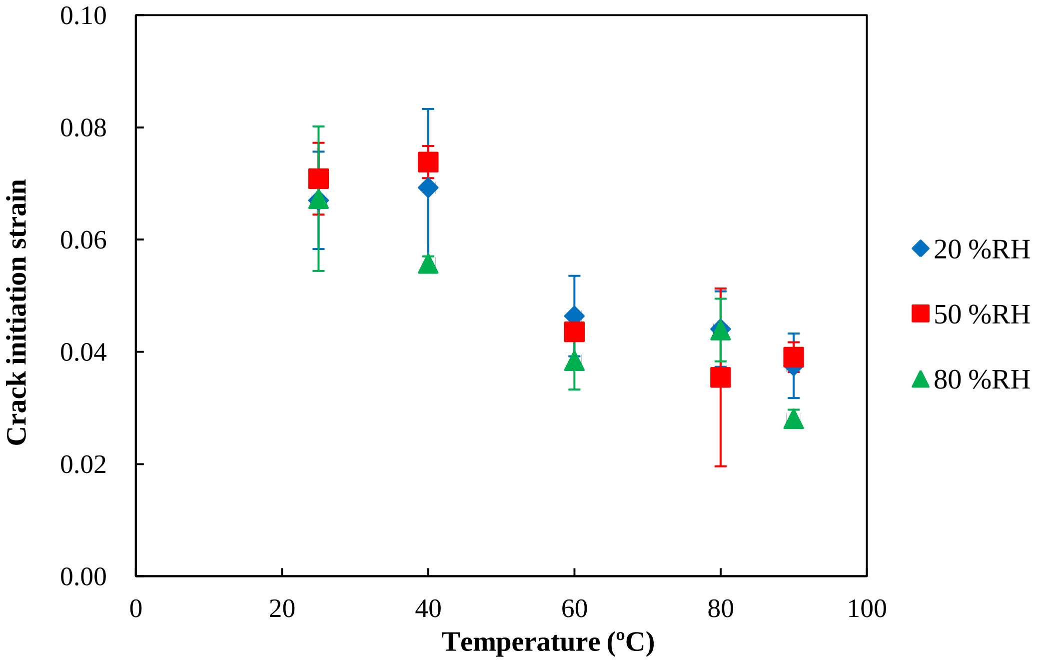

Fig.3.10 Crack initiation strain of the CL at different temperatures and humidities

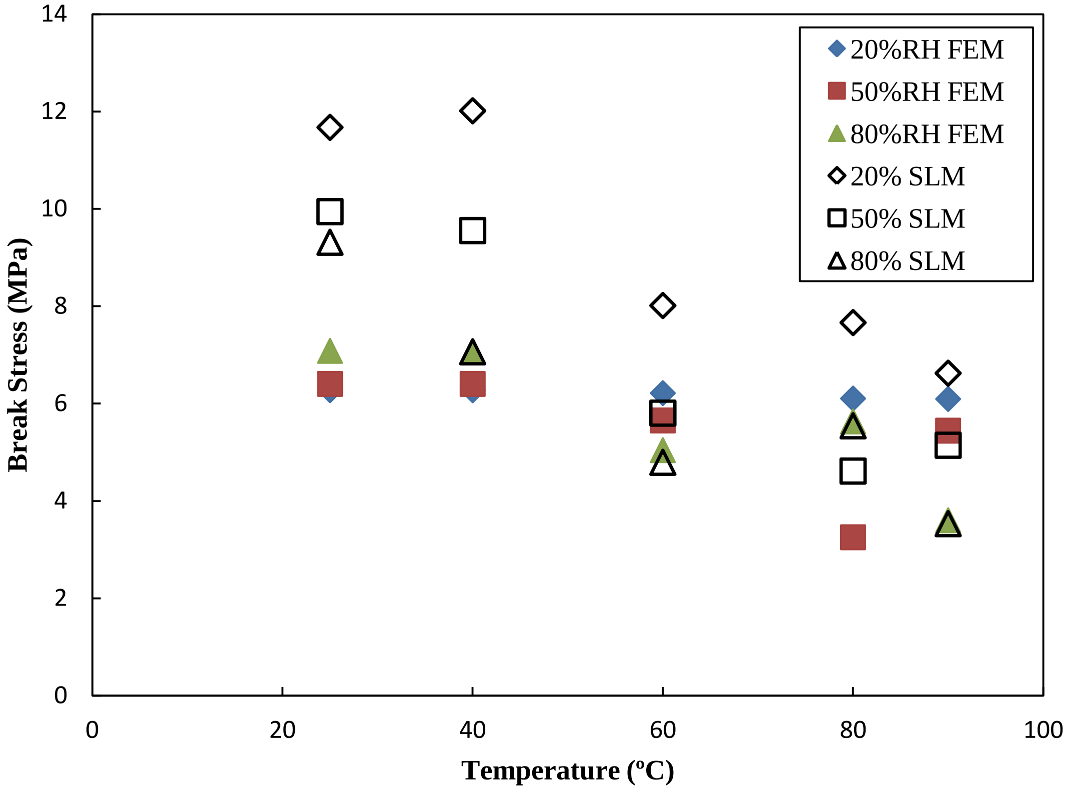

Fig.3.11 Break stress derived from the finite element model (FEM) and the shear-lag model (SLM)

is considered. Dependence on the strain rate is investigated. While the failure criterion is independent from the strain rate, it has been shown that mechanical parameters of Nafion are logarithmically correlated to it owing to its viscous properties[52].

The experimental procedure consisted of submitting the specimens to cyclic strains until the first crack appeared. The monitoring of the surface of the CL was done with an optical microscope with a 1000 times magnification, allowing to detect cracks of a size in the order of a few micrometers, as can be seen in Fig. 3.8(b). Since only a small portion of the surface of the specimen can be monitored this way, the experiments had to be done at least four times for each case in order to guarantee reliable results. Experimental results are summarized in Fig. 3.12. The objective of the finite element analysis was to replicate this experiment and to search for a failure criterion allowing to predict the onset of failure. Fatigue failure occurs even when the stress amplitude is under the maximum stress criterion for tensile tests, so there is a need for a more appropriate criterion for fatigue failure. The accumulated dissipation energy D_c, which builds-up during cycling until failure, and is not affected by the strain rate, was chosen. D_c represents the plastic dissipated energy per unit volume, or in other words, the energy that is lost due to plastic deformation of the material. It is calculated as

$$D_c = \int \sigma_P \cdot \dot{\varepsilon}_P^{pl} dt \tag{3.14}$$

where σ_P and ε_P^{pl} are respectively the stress and the plastic strains in the elastic-plastic network of the two-layer viscoplastic model. t is the time variable.

Noteworthy is the fact that fatigue only happens in cases where failure does not happen in the elastic domain of the CL, that is, low temperatures or low humidities.

Figure 3.13 shows the results obtained for a strain rate of 0.0025 s^{-1}. The line of equation $\Delta\varepsilon_p=0.0479N^{-0.163}$ represents the Coffin-Manson law established by the experiment. Coffin-Manson law is used for low cycle fatigue (ranging from hundreds to tens of thousands of cycles) and does not hold well for very low cycle or high cycle. The best fitting critical energy density in the relevant range of cycles has been found to be D_c=12.4 MJ/m^3. When applied to tensile test this critical value was found to be equivalent to the proposed break stress, within experimental error. At very low cycle, the energy builds up more rapidly and thus failure happens sooner than suggested by the simulation.

Finally, FEM analysis was done again using a strain rate of 0.025 s^{-1} and the same failure criterion D_c=12.4 MJ/m^3. Results are shown in Fig. 3.14.

The simulation successfully reproduces experimental results on the relevant range of cycles at both strain rates, which validates the chosen failure criterion.

Results indicate that higher strain rates imply a greater number of cycles to failure. This is explained by the fact that, due to the viscoplastic behavior of Nafion, it deforms less when subject to higher strain rates, and thus less stresses are transferred to the CL.

Even though good results are obtained in the investigated strain rate range, the two-layer viscoplastic model used for Nafion fails to accurately represent the behavior of Nafion under

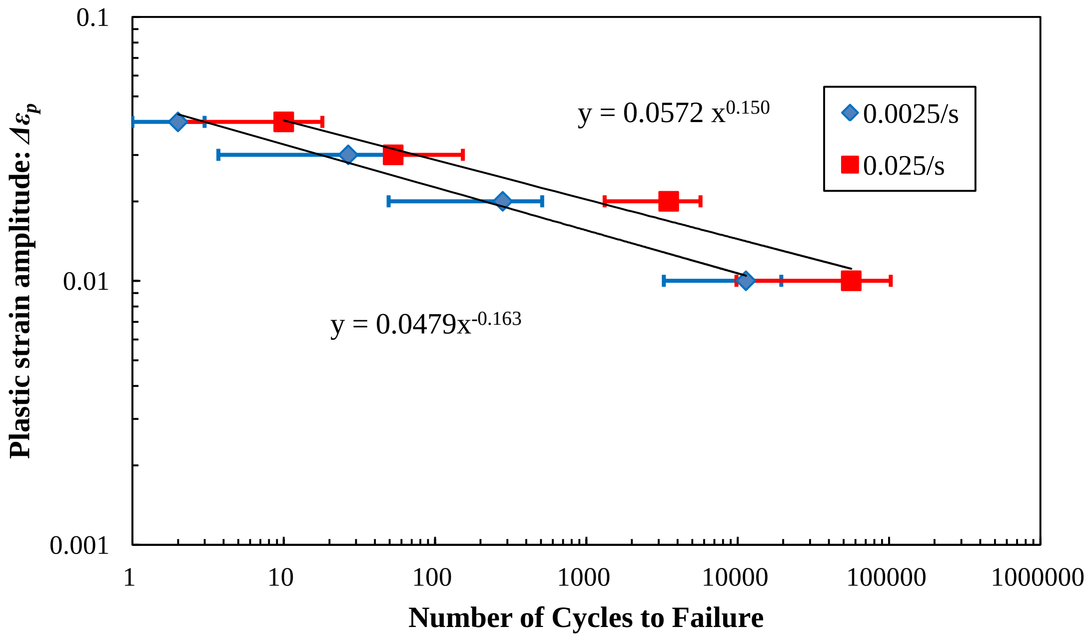

Fig.3.12 Result of low-cycle fatigue tests of the MEA in ambient conditions (25ºC, 50%RH)

for two different strain rates

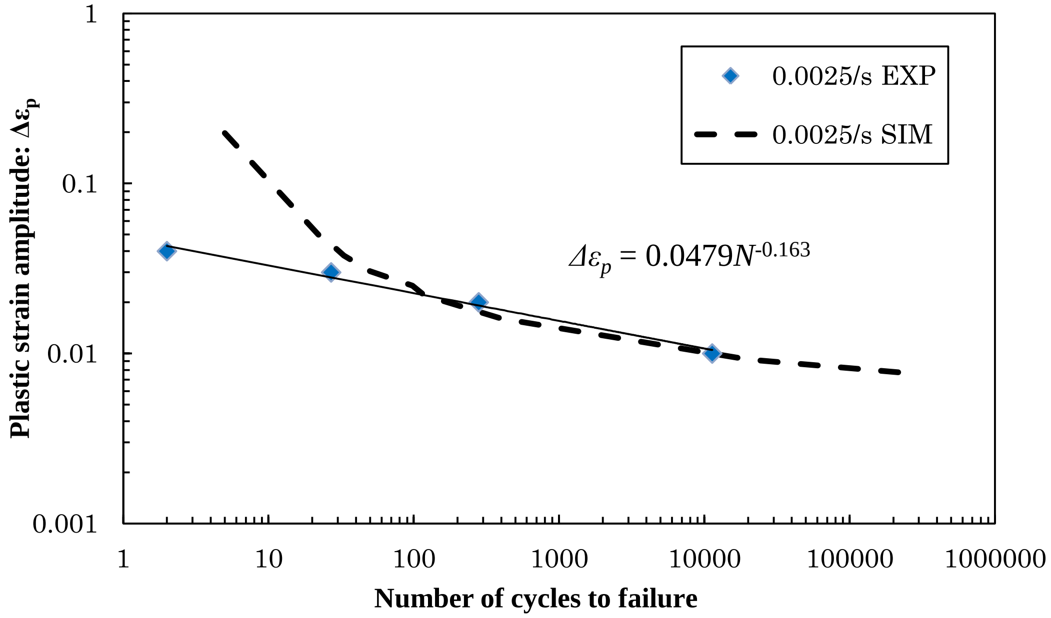

Fig.3.13 Comparison of simulation and experimental data for a failure criterion

D_c=12.4 MJ/m^3

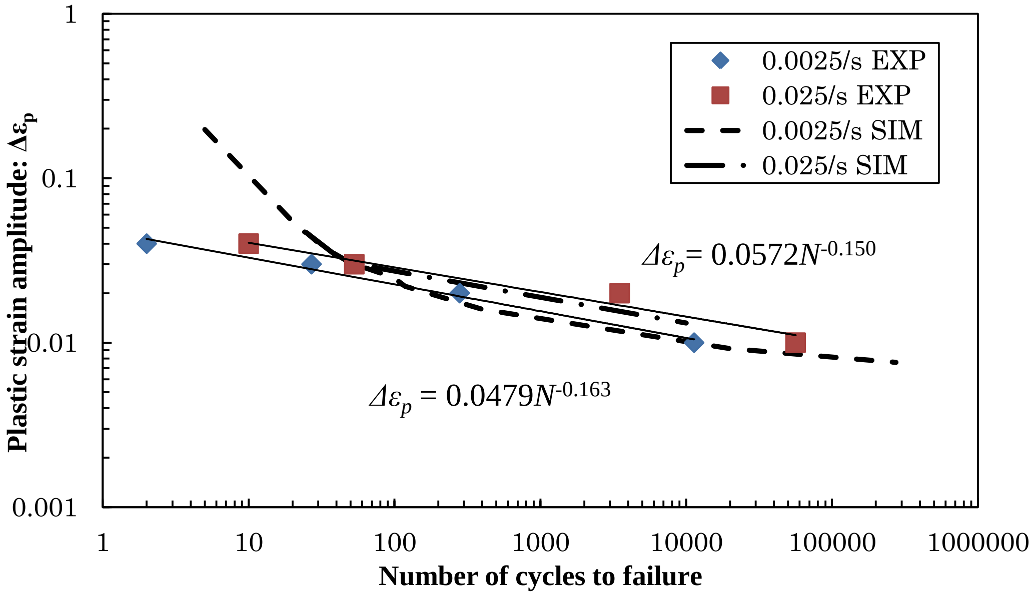

Fig.3.14 Comparison of simulation and experimental data for different strain rates

very low strain rates (in the order of $10^{-5}s^{-1}$), and thus limits the present model. In order to overcome this barrier, Chapter 4 will develop a more comprehensive model for Nafion.

3.4. Carbon/Nafion decohesion: A model to explain the crack initiation in the CL

In the fatigue tests described above, failure is considered to happen when cracks appear on the surface of the catalyst layer. While these results are useful to estimate the lifetime of the MEA, previous studies on the long-term behavior of fuel cells have reported that some loss of performance is observed before visible failure of the MEA happens[7,19,99,100]. This indicates that some restructuration of the layer happens before failure. However this is impractical to observe: the small scale at which this restructuration would happen (in the order of a hundred of nanometers) and the fact that the restructuration would occur inside the membrane means there is no experimental way to assess it. Nevertheless, this information would be useful to predict not only the total lifetime of the membrane, but also what performance loss is susceptible to happen before ultimate failure.

A hypothesis on what causes the loss of performance of the catalyst layer is decohesion between the carbon black and the Nafion that constitute the layer (see Section 2.3.1). The following paragraphs aim to refine this idea and quantify by using the finite element model that was developed earlier.

3.4.1. Origin of the Carbon/Nafion decohesion

Figure 2.3 shows the structure of a catalyst layer: clusters of carbon black are dispersed in an ionomer (Nafion in this case). Pores are also present due to the evaporation of the solvent. Since the Platinum particles are located at the surface of the carbon black clusters, this is where the reaction takes place. Therefore, cohesion between Nafion and the carbon black clusters is important to ensure the transport of protons to and from the site of the reaction. Decohesion results in less active area for the reaction, and as a consequence a loss of performance for the cell.

As has been discussed in the previous chapter, Nafion is sensitive to the changes of humidity and shrinks or swells according to its water content. On the other hand, carbon black is not only much stiffer than Nafion but also does not react to variation of humidity. This mismatch of expansion coefficient can be expected to create stresses along the interface of the two materials when the CL is subjected to humidity cycles. If those stresses can be shown to be enough to detach Nafion from the carbon black, it reinforces the idea that the Carbon/Nafion decohesion is the origin of the initial loss of performance of the catalyst layer. Further, it would also explain how the cracks that appear at the surface of the CL during fatigue tests are initiated.

3.4.2. Modeling the Carbon/Nafion interface

Since the materials and the environmental parameters necessary for this model are the same than for the previously developed model, the same constitutive models can be used here. Carbon black being much stiffer than Nafion, it can be modeled by a simple elastic behavior. The only new difficulty for this model is to design a shape and an accurate cohesive zone model for the interface.

In filled elastomers, the question of how the particles of carbon affect the local behavior of the polymer is still being debated, and different theories have been proposed to quantify that change[101-104]. Moreover, the carbon clusters are roughly circular in shape, but are dispersed randomly, making it difficult to select a specific representative configuration to model.

Based on Fig 2.3, the zone of most interest would be at the Carbon/Pore/Nafion triple interface. This is because of the fact that Nafion when absorbing humidity is allowed to expand into the pore, possibly slipping and detaching from the carbon black. As humidity decreases and Nafion shrinks back, decohesion would happen.

Figure 3.15 shows the model that was used to analyze this hypothesis. As mentioned earlier, the carbon black is a linear elastic model The Young's modulus and Poisson ratio of the agglomerate are taken to be E=4.8GPa[61] and v=0.15. These values are close to the properties of bulk graphite. Symmetry boundary conditions are applied to three of the faces, while the remaining face is left free to move. A field variable is introduced to represent humidity.

While carbon black is assumed to not be sensitive to humidity, a coefficient of hygro expansion β_ϕ is applied to Nafion. The mechanism is similar to that of thermal expansion, in that changes of humidity will introduce a swelling strain in the material:

$$\varepsilon^S = \beta_\phi \Delta\phi \tag{3.15}$$

In this equation, ϕ is the water activity of Nafion, which is empirically related to the relative humidity. The correspondence between ϕ and relative humidity is discussed in Ref. [33]. It is estimated that ϕ=1.5 corresponds to 30%RH, ϕ=3.5 to 50%RH and ϕ=22 to a fully hydrated state. The value for the coefficient of hygro expansion is taken from Ref. [52] as $\beta_\phi = 0.0081\ \phi^{-1}$.

Other studies investigating the delamination of polymers from carbon product suggest a maximum shear stress criterion for the cohesive zone model, defined as follow[61]:

$$\sigma_{shear,\max} = \frac{\sigma_{Y,Nafion}}{\sqrt{3}} \tag{3.16}$$

The maximum shear stress is function of the yield stress of the polymer, Nafion in this case. Once this criterion is reached, the cohesion is lost and the materials are allowed to slip or to move away from each other. The simulation is designed to verify whether the maximum shear stress can happen due to the changes oh humidity inside the cell, and to what extent. For this reason, the load is applied by way of humidity cycles.

3.4.3. Results of the interface simulation

The findings from the simulation are synthesized in Fig 3.16. As expected, upon swelling Nafion expands into the space left by the pores. This creates shear stresses at the interface with the carbon black. As depicted in Fig. 3.16, the maximum shear stress is easily reached even with small variations of humidity: slippage of Nafion against the carbon black is initiated for a variation of humidity as little as 5%RH. During the function of a fuel cell the humidity can vary by over 50%RH, meaning that this effect is likely to affect the CL. Once decohesion between

Nafion and the carbon black happens, slippage then increases rapidly with further increase of humidity. When humidity decreases, Nafion does not slip back in place along the interface: the amount of slippage does not immediately decrease, instead staying constant. This can be explained by the plastic deformation that happens as a result of being compressed against the carbon black. The hysteresis indicates that some restructuration occurs in the catalyst layer when subjected to humidity cycles.

The simulation suggests, however, that Nafion does not appreciably move away from the carbon black as the humidity decreases. The gaps that were created at the interface because of the shrinkage of Nafion were calculated to be in the order of 0.01nm wide, which is negligible at the scale of the model.

Therefore, it can be concluded from this simulation that the variations of humidity affect the structure of the CL at the nanoscale. While the deformation is not enough to directly create a gap between the carbon black and Nafion (which would result in a loss of performance due to the decreased active reaction area), it is sufficient to provoke a permanent restructuration of the layer by decreasing the cohesion between Nafion and the carbon clusters, even at very moderate loads. It can be hypothesized that with time these imperfections develop and propagate through the layer, eventually resulting in the failure of the CL similar to what was observed in fatigue tests.

3.5. Summary

In this chapter, the stress-strain constitutive behavior of the MEA was investigated.

Mechanical properties were determined through experiment, and were subsequently used for designing a numerical model of the MEA. Failure criteria were established for both tensile test and fatigue analysis, and results were shown to be consistent between experiment and simulation. A model was also proposed in order to elucidate the mechanism of crack initiation at the nanoscale. This study provides a better understanding of the properties of the crucial fuel cell component that is the MEA, thus serving as a base for future work to design devices with better reliability.

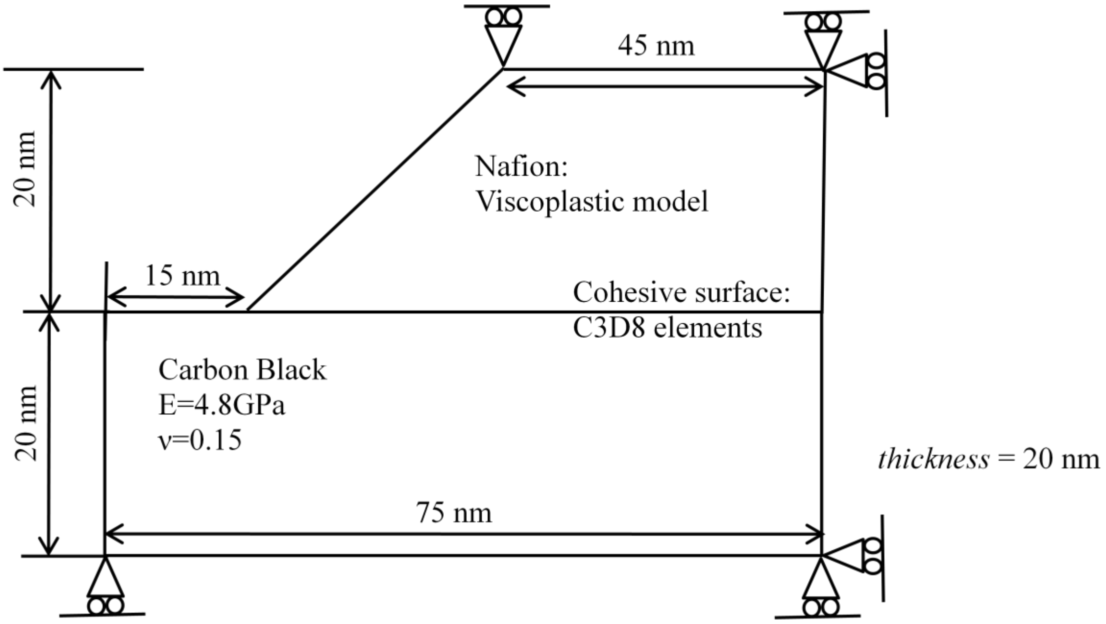

Fig.3.15 Proposed Finite Element Model for the interface between Nafion and Carbon

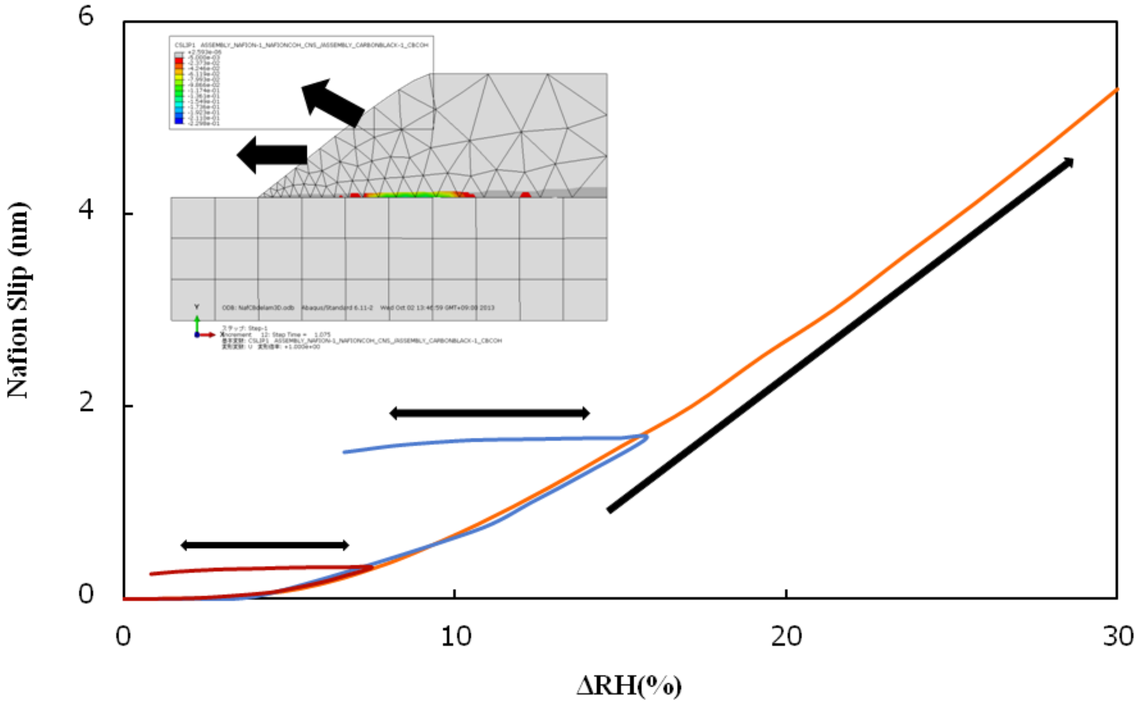

Fig.3.16 Evolution of Nafion slippage with variations of humidity

CHAPTER 4

Optimization of the constitutive model for Nafion

The two-layer viscoplastic model for Nafion that was developed in Chapter 2 was shown to be accurate at low to moderate strains. However, it also has some shortcomings, which have already been mentioned:

- The accuracy is diminished at high strains
- A separate set of parameters has to be calculated for every configuration of temperature and humidity
- It is not compatible with very low or very high strain rates.

Once properly calibrated, this model can therefore be used for applications that do not involve imposing high strains on the material, like the fatigue tests of Chapter 3. However, limitations start to appear when trying to simulate the failure and cracking of Nafion, because these experiments require the model to stay accurate at high strains, up to the maximum strain of the material. For the model to stay accurate in many different situations is naturally a requirement for the numerical simulation to be as versatile as possible. The purpose of this chapter is to build upon the model that was first introduced by Boyce and Silberstein in 2010 in order to achieve this result.

4.1. Boyce and Silberstein’s constitutive model for Nafion

The most accurate numerical model for Nafion found in the literature was proposed by Boyce and Silberstein in 2010[52]. It uses a variety of components to account for both intermolecular and network deformation of Nafion, as well as for the back stresses that occur during dynamic loading. Attributing these model components to specific molecular arrangements within the material is challenging. Figure 4.1 gives a rheological representation of the constitutive model used here. *I* and *N* stand for intermolecular and network mechanisms respectively; *P* denotes the plastic deformation and *B* the back stress mechanism. The representation given here is simplified, as in the model these components are non-linear and act three dimensionally.

In this model, the total stress is the sum of the stresses from the intermolecular and network mechanisms:

$$\sigma = \sigma_I + \sigma_N \tag{4.1}$$

The respective intermolecular and network stresses are calculated as follow:

$$\sigma_{Ii} = \frac{1}{J^e}[2\mu(\ln \lambda_{Ii}^e)' + \kappa \ln J^e] \tag{4.2}$$

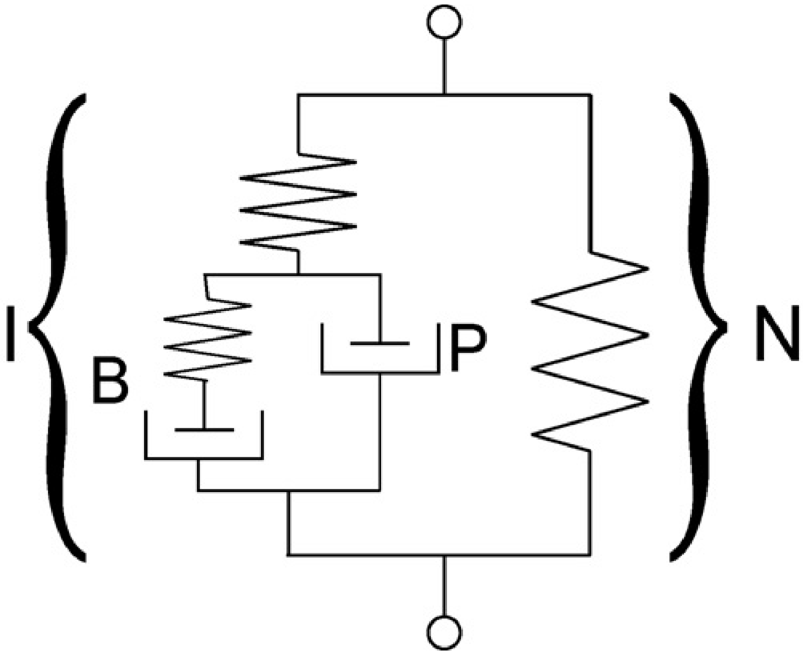

Fig. 4.1. 1-D Rheological representation of the constitutive model for Nafion

$$\sigma_{Ni} = \frac{\mu_N}{J_N^m \lambda^s} ({\lambda_{Ni}^m}^2 - {\lambda_{chain}^m}^2) \tag{4.3}$$

The indice i indicates the three principal stretch directions, λ_i the principal stretches, and J the mechanical volume ratio: $J = \lambda_1\lambda_2\lambda_3$. The total stretch λ_i is decomposed into elastic, plastic and swelling components: $\lambda_i = \lambda_i^e \lambda_i^p \lambda_i^s$. In Eq.(4.3), the exponent m only takes into account mechanical contributions: $\lambda_i^m = \lambda_i^e \lambda_i^p$. λ_{chain} is a measure of network stretch. Parameters μ, κ and μ_N are listed in Table 4.1. Finally, in Eq.(4.1) the apostrophe indicates that the deviatoric tensor is considered.

The elastic response of the back stress σ_B follows the same law as Eq.(4.2), however since plastic deformation is supposed to be isochoric in this model, it simplifies as

$$\sigma_{Bi} = \frac{1}{J} 2\mu_B \ln \lambda_{Bi} \tag{4.4}$$

On the molecular level, the intermolecular mechanism (I) is due to the deformation of individual molecules or clusters. Once the strain becomes enough to plastically deform those clusters, the plastic deformation mechanism (P) starts to become relevant. This is a distributed yield that occurs over a rather large range of strains (from less than 0.05 to 0.25 and above, as shown in Fig 4.2). This is because the individual configuration of clusters will make them more or less prone to yielding. Percolation softening happens as the plastic yield propagates through the membrane. It can be noted from Fig 4.2 that it is difficult to define the yield stress of Nafion because of this mechanism: from the start to the end of the distributed yield the stress grows from about 8MPa to over 14MPa.

The back-stress component (*B*) is important for unloading and cyclic behavior. The origin of this mechanism is likely to be the stress that locally develops around the plastically deforming region. This stress is restituted during unloading, facilitating the reverse deformation of the material. This explains why the slope of stress-strain curve is lower during unloading than during initial loading. Finally, the molecular alignment falls under the network component (*N*). As the strains keep increasing after yielding, individual molecules tend to align in a direction parallel to that of the strains. This effect only becomes noticeable after yield, and becomes more dominant the higher the strain.

A significant advantage of this model is that it also takes into account the dependency on temperature and humidity. It is also possible to determine how these parameters affect the individual components of the model. Neither temperature nor humidity has a strong effect on the intermolecular elastic deformation. Plastic yield is very sensitive to humidity since water gathers mostly around clusters and affect the material by making them more compliant. Meanwhile, increased temperature results in increasing the quantity of amorphous regions in Nafion (eventually reaching the glass transition to a rubbery state at temperatures above 80ºC). Amorphous regions, as opposed to clusters, offer less resistance to deformation and therefore result in an overall softer material.

In the present study, this constitutive model was used as a base for the finite element modeling of Nafion. There is very good agreement with experimental data at low to middle strains, however there was some divergence happening at higher strains, where molecular alignment becomes the most important factor of the constitutive model. Figure 4.3 compares the experimental behavior of Nafion and the calculated behavior using the same parameters as [52]. There is a discrepancy for strains above 0.25 that becomes larger the higher the strains. Since in this study the fracture of Nafion is modeled, it is necessary that the model be valid at high strains until the maximum stress is reached. Therefore some parameters of the initial model need to be modified in order to match as closely as possible the experimentally observed stress-strain behavior of the membrane.

4.2. Optimization of the post yield behavior through the least square method

4.2.1. Selection of the parameters to optimize

Since most of the attention is put into correctly modeling the yielding behavior, most of the parameters of the model are designed to control it (see Table 4.1). At high strains (after yielding has occurred), the behavior of Nafion is governed only by two independent mechanisms. The first is the decrease of the shear modulus until its saturation value μ_{sat}, which controls the post-yield softening of the material, and therefore directly impacts the value of σ_I. The variation of the shear modulus is calculated by

$$\dot{\mu} = h_\mu (1 - \frac{\mu}{\mu_{sat}}) \dot{\gamma}_I^p \tag{4.5}$$

h_μ is a fitting parameter that controls the rate of decline of the shear modulus, and $\dot{\gamma}_I^p$ is the

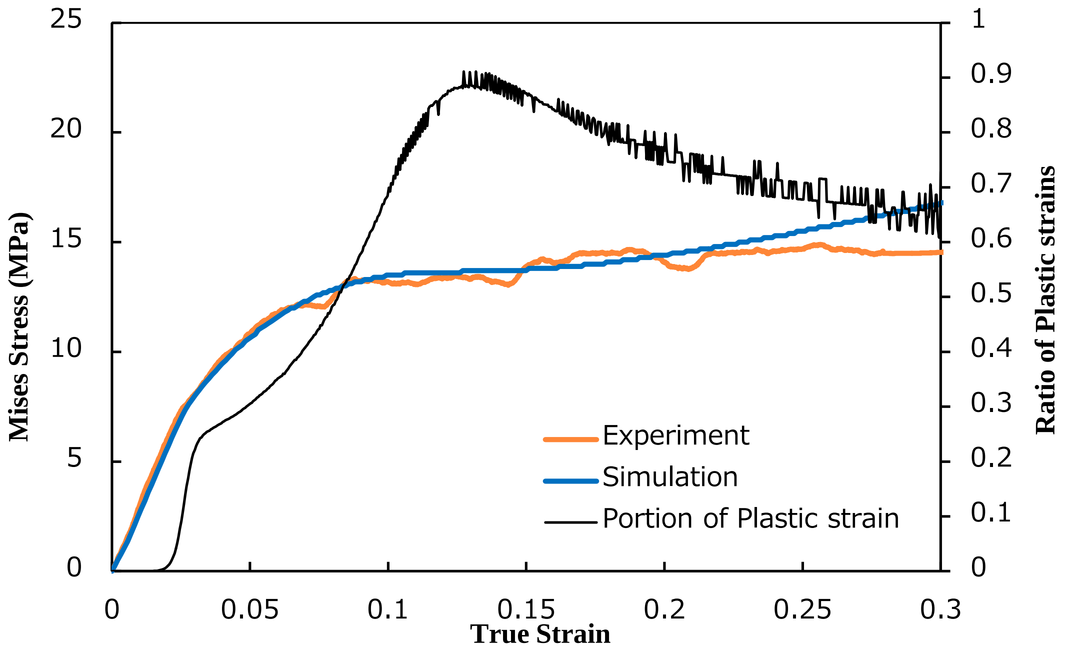

Fig. 4.2. Illustration of the distributed yield mechanism on the stress-strain curve of Nafion

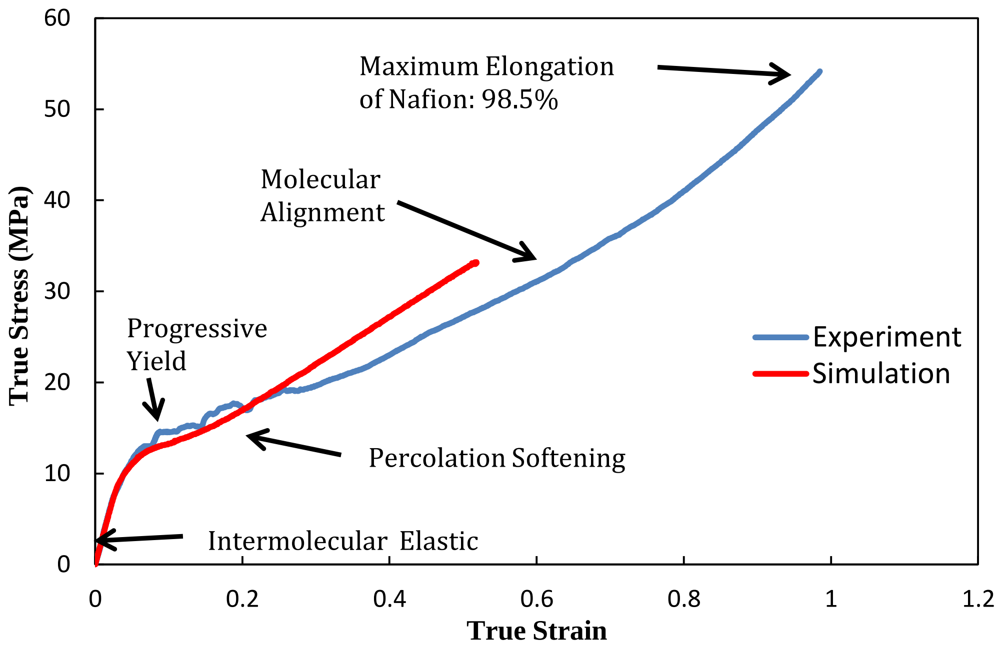

Fig. 4.3. Comparison of experimental and calculated behavior of Nafion by implementing the constitutive model from [52]

magnitude of the plastic velocity gradient. h_μ is set so that the value of μ_{sat} is attained after yield.

$\dot{\gamma}_I^p$ regards plastic deformation, and is calculated as

$$\dot{\gamma}_I^p = \dot{\gamma}_0 \exp[\frac{-\Delta G}{k_B\theta}]\sinh[\frac{\Delta G}{k_B\theta}\frac{\tau}{s}] \tag{4.6}$$

where ΔG is the activation energy, k_B the Boltzmann constant and θ the absolute temperature. τ is the scalar equivalent shear stress, defined as

$$\tau = \sqrt{\frac{1}{2}\sum_{i=1}^{3}(\sigma_{Ii} - \sigma_{Bi})'^2} \tag{4.7}$$

s is the shear resistance, divided into three components: $\tilde{s}$, which controls the distributed yield; $\hat{s}$, which controls the percolation softening and $\bar{s}$, which controls the molecular alignment. s is given by

$$s = \tilde{s} - \hat{s} + \bar{s} \tag{4.8}$$

Both $\tilde{s}$ and $\hat{s}$ vary following a law analog to Eq.(4.5) and, similarly to the shear modulus, saturate at yield. The remaining mechanism $\bar{s}$ keeps increasing as the strains in Nafion become higher, accounting for the increasing difficulty of deforming the polymer as the individual molecules start to align with each other. It is calculated as a function of the network stretch with the following equation:

$$\bar{s} = h(\lambda_{chain}^{n} - 1) \tag{4.9}$$

λ_{chain} is a measure of the network stretch, while h and n are fitting parameters.

This leaves a total of three parameters, μ_{sat}, h and n that have a dominant effect on the calculation on stresses at high strains. These parameters need to be adjusted in order to replicate the behavior at high strains.

4.2.2. *Optimization of the post yield behavior*

The least square method is applied in order to find the best fitting combination of these three parameters. The objective is to match the stress-strain relationship of the finite element simulation and of the experiment as closely as possible by minimizing the function

$$f(\mu_{sat}, h, n) = \sum_{\varepsilon=0}^{\varepsilon_{\max}} (\sigma_{\exp} - \sigma_{FEM})^2 \tag{4.10}$$

Since the constitutive model is non-linear, there is no close-form solution to this least square problem. Some initial values for the three parameters need to be chosen; this is done through trial-and-error method. The initial values are decided as such:

$$\begin{cases} \mu_{sat} = 3.5\text{x}10^7 \text{ Pa} \\ h = 2.3\text{x}10^6 \text{ Pa} \\ n = 10 \end{cases} \tag{4.11}$$

In order to simplify the problem, it is worth noticing that since μ_{sat} is the only one of the three parameters to control the immediate post-yield behavior of the material before molecular alignment starts to play a dominant role, it is possible to first find the best value for μ_{sat} alone by minimizing the function

$$g(\mu_{sat}) = \sum_{\varepsilon=0}^{0.4} (\sigma_{exp} - \sigma_{FEM})^2 \tag{4.12}$$

Experimentally, a true strain value of 0.4 corresponds to the transition between the dominant mechanisms governing the behavior of the material (see Fig.4.5). Before it, μ_{sat} is the dominant parameter, while h and n control the subsequent behavior. Keeping the initial values for h and n from Eq.(4.11), the function g is depicted in Fig.4.4(a). It displays a W-pattern with two local minima at 3.4x10^7 Pa and 3.6x10^7 Pa. Even though the former value minimizes the g function, the latter was found to give a better overall fitting when considering the full range of strains, while not significantly decreasing the accuracy at middle strains.

Finally, the f function in the neighborhood of the initial values of the parameters was drawn, with the results shown in Fig.4.4(b). The best combination was found to be

$$\left\{\begin{array}{l} \mu_{sat} = 3.6\text{x}10^{7}\ \text{Pa} \\ h = 2.2\text{x}10^{6}\ \text{Pa} \\ \text{n} = 10 \end{array}\right. \tag{4.13}$$

The resulting constitutive model after the least squares optimization is shown in Fig.4.5, compared with the model after optimization and with the 2-layer viscoplastic model that was developed in Chapter 3. As can be seen, although the proposed model tends to slightly overestimate the stress in the early stages of yielding, the accuracy at higher strains is greatly improved. For the purpose of calculating the strain energy, which is most relevant when studying crack propagation, the performance of each model can be seen in Fig. 4.6, with their absolute error summarized in Table 4.2. As can be inferred from Fig. 4.6, the behavior at high strains is much more relevant for the calculation of the strain energy than the behavior at low strains. In fact, the least squares optimization allowed to reduce the absolute error by a factor of three when compared to the initial model.

The accuracy of the model was deemed to be sufficient for the purpose of this study. It can be noted that since most of the parameters of the constitutive model in [52] are determined through trial-and error, it could prove valuable to realize an optimization study for the entire set of fitting parameters in order to achieve an even more accurate model. This however is beyond the scope of this study. Table 4.1 sums up the entire set of parameters used in the constitutive model.

4.3. Summary

In this chapter, a previously existing constitutive model for Nafion has been adapted to stay accurate at high strains. While several models for Nafion have been found in the literature (see Section 1.1.4), this is to the author’s knowledge the first time that emphasis was put on accurate behavior at high strains. Previous efforts were typically focused on modeling the low-strain behavior and in particular the yielding point. While the previous models are sufficient for estimating the behavior of Nafion in typical Fuel Cell application or in cyclic fatigue, in order to model the failure of Nafion it is necessary that the constitutive model stay accurate even at high strains.

Based upon the elastic-viscoplastic model proposed by Boyce and Silberstein in [52], three parameters were identified that controlled the behavior of Nafion at high strains. The least square optimization technique was applied to ensure that the chosen set of parameters give the best possible fitting. This model is useful for simulations that involve estimating the behavior of Nafion over large range of strains. In particular, it will be applied in Chapter 6 to recreate the results of DENT experiments, investigating the crack propagation in Nafion.

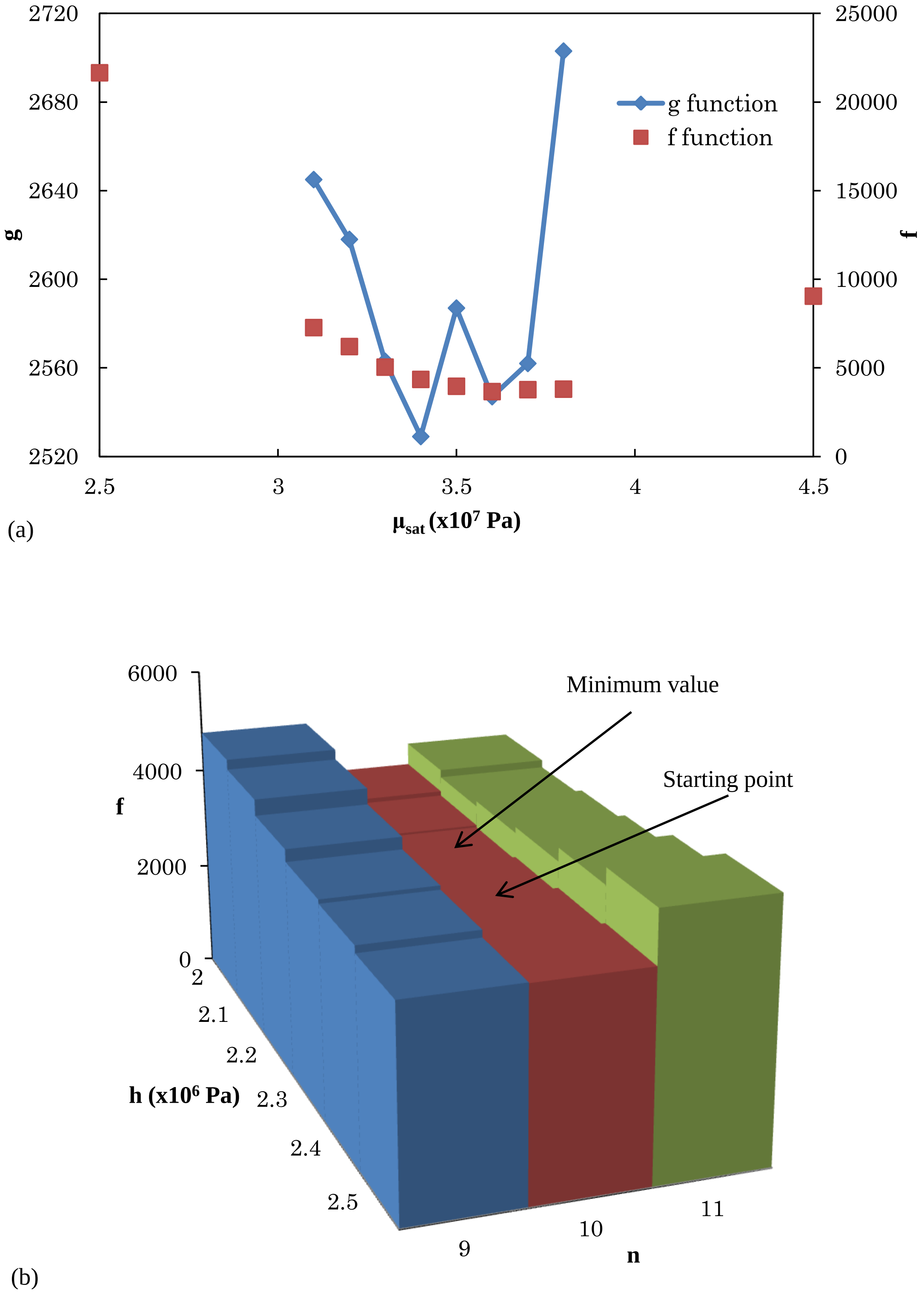

Fig. 4.4. (a) f and g functions for different values of μ_{sat}; (b) f function for μ_{sat} fixed at $3.6\text{x}10^{7}$ Pa

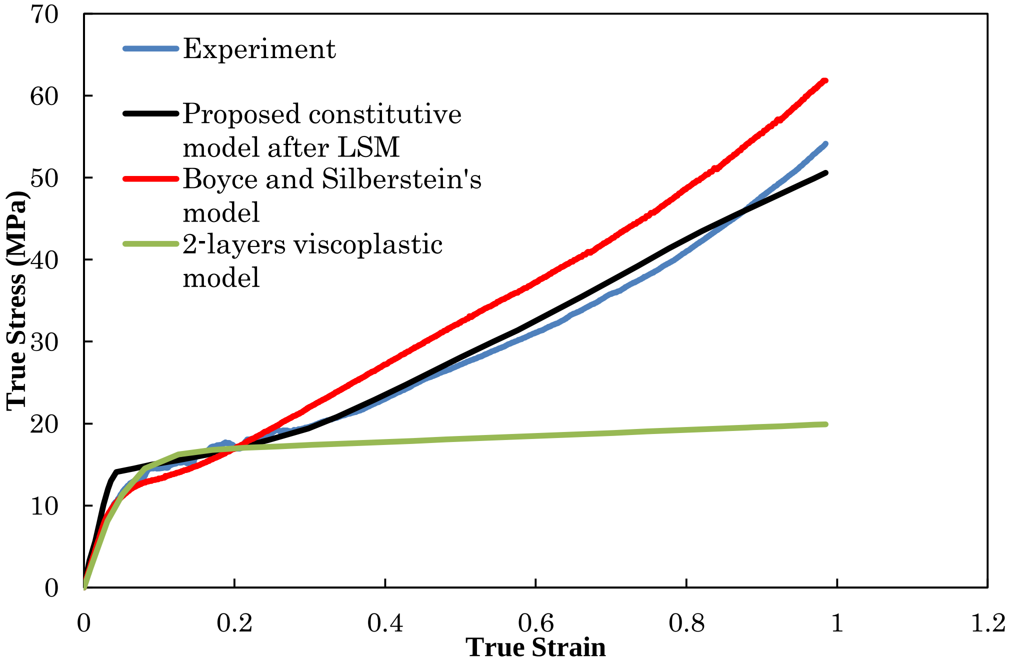

Fig. 4.5 Comparison of the simulation of Nafion behavior at 25℃ and 20%RH for Boyce and Silberstein's model before and after LSM optimization and the 2-layer viscoplastic model

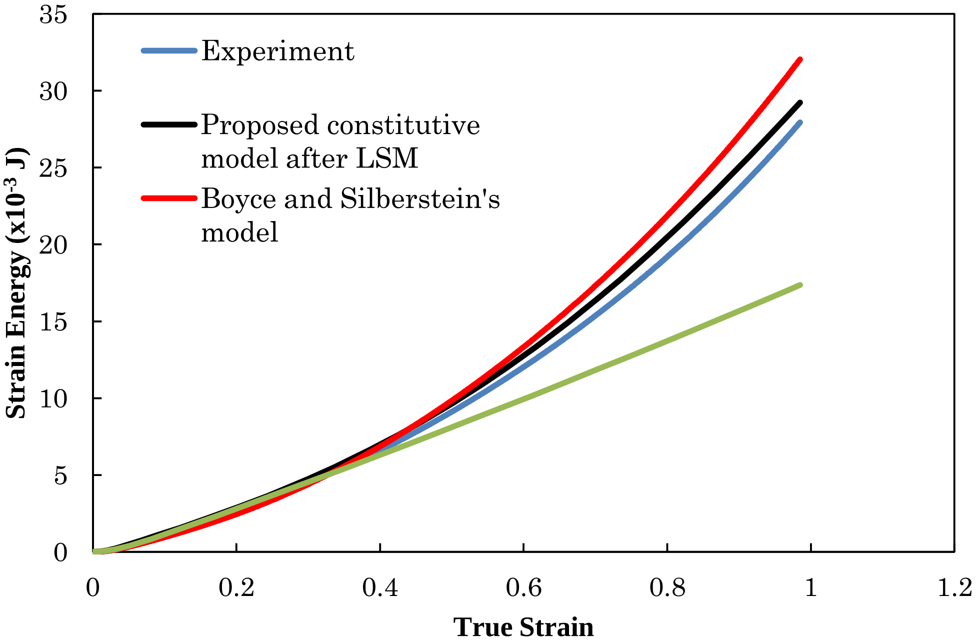

Fig. 4.6 Comparison of the strain energy for the three models with experimental results

Table 4.1. Model parameters used in the FEA

Model component	Material parameter	Value in [52]	Proposed value
Elastic	κ	$3.6\text{x}10^{8}$ Pa	
	μ_0	$1.1\text{x}10^{8}$ Pa	
Elastic evolution	h_μ	$4.7\text{x}10^{9}$ Pa	
	μ_{sat}	$7.0\text{x}10^{7}$ Pa	$3.6\text{x}10^{7}$ Pa
Rate-dependant yield	$\dot{\gamma}_0$	$6.72\ \text{s}^{-1}$	
	$\tilde{s}_0$	$8.98\text{x}10^{-20}$ J	
Distributed yield	$\tilde{h}$	$1.2\text{x}10^{9}$ Pa	
	$\tilde{s}_{sat}$	$9.6\text{x}10^{6}$ Pa	
	$\hat{h}$	$7.5\text{x}10^{7}$ Pa	
	$\hat{s}_{sat}$	$6.5\text{x}10^{6}$ Pa	
Isotropic hardening	h	$2.6\text{x}10^{7}$ Pa	$2.2\text{x}10^{6}$ Pa
	n	1	10
Back stress	μ_B	$2.65\text{x}10^{7}$ Pa	
	s_{B0}	$4.3\text{x}10^{6}$ Pa	
	h_B	$2.3\text{x}10^{8}$ Pa	
	s_{Bsat}	$7.7\text{x}10^{6}$ Pa	
Network	μ_N	$3.3\text{x}10^{6}$ Pa	
Thermal expansion	α_θ	$1.23\text{x}10^{-4}\ \text{K}^{-1}$	
Hygro expansion	β_ϕ	$8.1\text{x}10^{-3}\ \phi^{-1}$	

Table 4.2. Absolute error of the strain energy over the entire range of strains for each model

2-layers viscoplastic model	Boyce and Silberstein’s model	Proposed constitutive model after LSM
37.9%	14.7%	4.7%

CHAPTER 5

Effect of environmental conditions on the Essential Work of Failure of Nafion

The focus of this thesis until now has been on two points. In Chapters 2 and 4, the mechanical behaviors of the materials that compose the MEA were investigated. These behaviors are relevant to the normal function of the fuel cell. The second point has been in Chapter 3, were attention was put on the onset of failure in the MEA. There, a criterion was proposed in order to estimate the time to failure. It was found that cracks generally form in the CL.

Chapters 5 and 6 will deal with the crack propagation inside the proton exchange membrane. While the onset of failure is reached in the CL, the failure of the cell is not immediate. Once formed these cracks often continue to propagate through the CL and the proton exchange membrane. Since Nafion is the primary material in the MEA (making up both the PEM and the ionomer support in the CL), knowing its fracture resistance is a key to get a better estimate of the lifetime of the MEA.

5.1. Importance of the Essential Work of Failure

Given the importance of preventing the degradation of the MEA, it is crucial to have reliable data on its fracture resistance and behavior of its components, and how it varies with different environments. In this study, the essential work of fracture (EWF) of the proton exchange membrane is calculated for different temperatures and humidities. The EWF is the minimum amount of energy required in order to create a fracture surface in a given material. This property is commonly used for ductile polymers, as the fracture toughness that the EWF measures is equivalent, but easier to calculate, than the critical J-integral approach[105]. The EWF relates to the progression of cracks inside the material, which is particularly relevant in this case: since mechanical fatigue is the main cause of failure, critical stresses causing the material to break catastrophically are not expected to happen; more frequently, a significant proportion of the material's lifetime will be spent in the crack propagation phase.

By knowing how environmental conditions affect the fracture resistance, it becomes possible to better estimate the lifetime of the membrane. This is important both from the point of view of cost (scheduled maintenance) and safety. Moreover, since failure of the proton exchange membrane is a common cause of the loss of performance of fuel cells, the fracture resistance of the membrane is indicative of the reliability of the fuel cell as a whole.

5.2. Experimental method

5.2.1. Double-Edge Notched Tensile Test

The Essential Work of Fracture is an important material property to calculate when studying the fracture of polymers, as it gives the minimal amount of energy necessary in order to create a crack surface. The interest of the EWF approach over other methods lies in the relative simplicity of the experimental protocol. The double-edge notch tensile test (DENT) was developed in order to calculate the EWF of thin, ductile membranes. It is performed on a membrane notched with two symmetrical V-shaped incisions, as described in Fig. 5.1. A tensile load is applied until complete tearing of the specimen. The total work of fracture, W_F, can then be calculated from the load-displacement diagram of the experiment.

5.2.2. Method of calculating the EWF

The total work of fracture W_F can be separated into essential energy of fracture and other non-essential dissipated energies. This can be written as:

$$W_F = W_E + W_P \tag{5.1}$$

where W_E is the fracture energy and W_P is the plastic dissipated energy.

Several assumptions are taken in this experiment: there is supposed to be no out-of-plane stress, no edge effects, and the zone of plastic deformation should be limited in a small region along the ligament. In practice, in order to validate the underlying assumptions of the DENT experiment to obtain accurate measurement of the EWF, it is generally accepted[106,107] that the ligament length should verify

$$5t < l < \frac{W}{3} \tag{5.2}$$

l and W being the ligament length and the width of the specimen, as shown in Fig. 5.1.

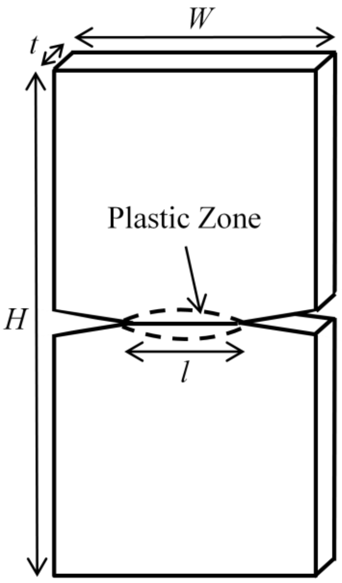

Fig. 5.1 Schematic of a DENT test specimen

However these inequations are only estimations; the actual range of valid ligament length is dependent on the material used. As the thickness of the membranes used in this study is very thin (25μm), the first part of the inequation is easily met. As reported in [106], ligament sizes greater than W/3 are valid as long as the specimen fails in a ductile manner. Ideally, the ligament should be fully yielded before the crack initiation, however it has been shown that this condition is too stringent and not necessary in order to calculate the EWF[108,109].

The plastic dissipated energy is proportional to the volume of the plastic zone around the ligament, while the EWF is a surface energy proportional to the surface of the created crack. It is therefore possible to rewrite Eq.(5.1) as

$$w_F lt = w_E lt + \beta w_P l^2 t \tag{5.3}$$

which simplifies into

$$w_F = w_E + \beta w_P l \tag{5.4}$$

where w_F, w_E and w_P are the specific energies relative to W_F, W_E and W_P respectively, and l and t are the ligament length and thickness of the specimen as shown in Fig.5.1. β is the shape factor of the plastic zone, and is not directly accessible from the experiment. The simplest method to calculate the EWF from Eq.(5.4) is to perform the DENT with several ligament lengths, then to linearly extrapolate the results to a length of 0 in order to isolate w_E.

5.2.3. Material

The proton exchange membranes in this study are made of DuPont's Nafion® NR211.

Knowing the crack propagation properties of Nafion is particularly important since it has been hypothesized that the cracks that form in the CL eventually propagate in the proton exchange membrane (see Chapter 3).

The specimens in this study are all cut to the same dimensions, with a width of 10mm and a gauge length of 20mm. The nominal thickness is standard for the NR211 type at 25μm. No pre-treatment was applied to the specimens before cutting: they were used as received from the distributor.

5.2.4. Experimental protocol

The DENT test requires to apply a tensile loading on pre-cracked strips of Nafion and to record the load-displacement and stress-strain curves until complete failure of the specimen.

The tensile testing equipment is largely the same as the one described in Chapter 2. It is composed of two linear stages with stepping motors (SGSP26-100, Sigma Koki Co., Ltd.) controlled by a motor controller (GSC-02, Sigma Koki Co., Ltd.) using LabVIEW (National Instruments Corporation). The displacement resolution is 40 μm. The gripping ends are large enough to grip the entire width of the specimen and are coated in non-slip rubber so as to avoid dislodging, as visible in Fig. 5.2(a). The crosshead speed that was applied to the specimen during tensile loading was 0.04 mm s^{-1}.

In order to control for temperature and humidity around the specimen, the setup was placed inside an environmental chamber. Temperature is controlled by heaters around the specimen, specifically a transparent glass heater above (S-101, Blast Co., Ltd.) and a rubber heater below (SCR-SQ, Sakaguchi E.H. Voc Corp.). Transparency of the glass heater was required in order to be able to observe the specimen in situ. Temperature was monitored by a thermocouple.

Humidity was controlled using an injection hose connected to a dew-point generator (me-40ADP-SRZ, Micro Equipment Co., Ltd.). This setup allowed to control the environmental conditions with an accuracy of ±1°C and ±5%RH. Experiments were only conducted once equilibrium was reached in the chamber. The schematic in Fig. 5.2(b) sums up the experimental setup.

For the purpose of obtaining enough data to calculate the EWF, specimens were prepared with ligament lengths of 2, 4, 6 and 8mm. For each ligament length, experiments were repeated four times on different specimens. Four environmental conditions were considered: ambient conditions (30°C, 50%RH), high humidity (30°C, 100%RH), high temperature (80°C, 50%RH) and high humidity and temperature (80°C, 100%RH). These environmental conditions mimic those met by fuel cells during normal function, as they commonly operate at 80°C in order for the chemical reaction to be sustained at a satisfying rate, while humidity naturally increase as water gets created by the oxidation of hydrogen.

The notches were created by cutting the specimen with a new razor, a method which is commonly found in the literature. There is no definitive answer on the exact effect of the notching technique on the fracture of the specimen. However in [109], when applying the DENT test on ductile polymers, there was no difference in the work of fracture by changing the notching

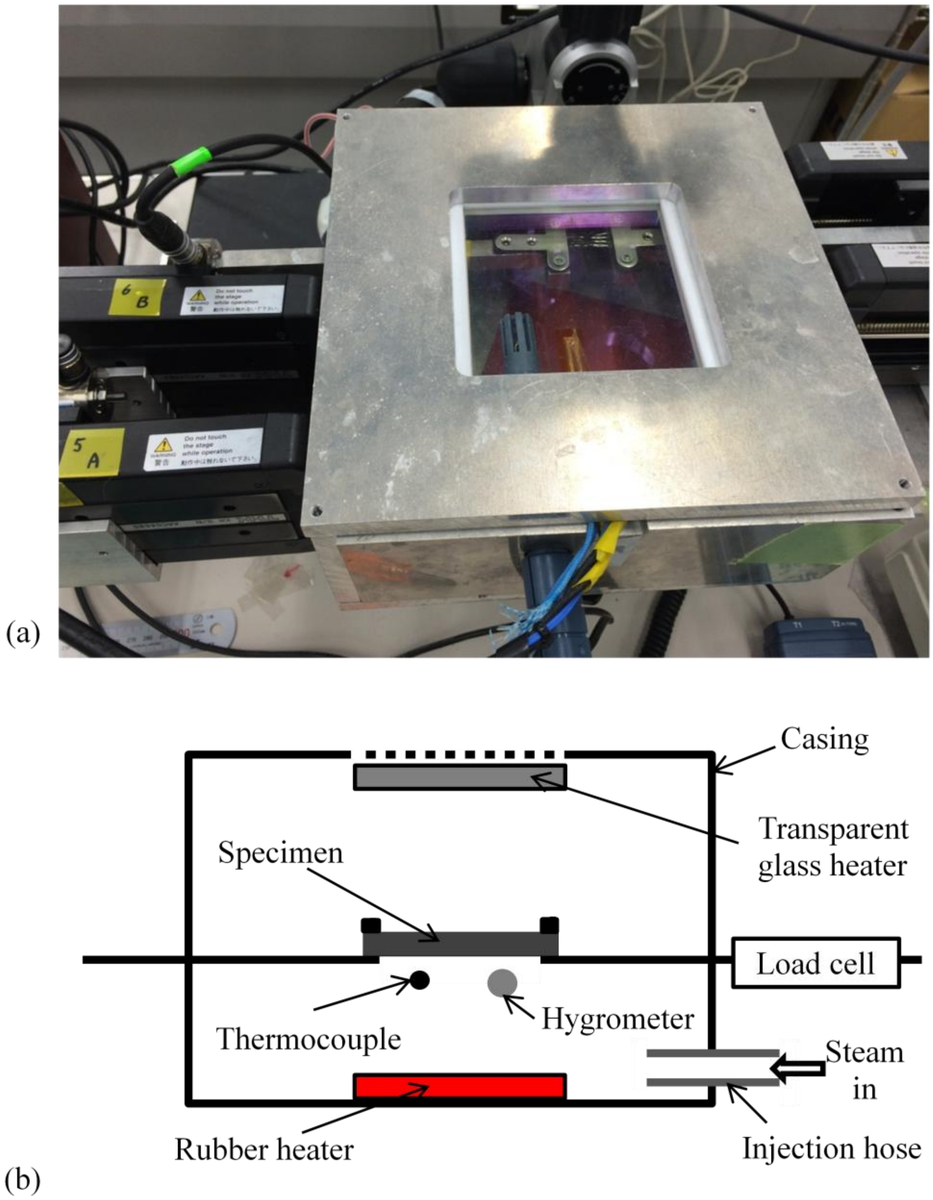

Fig. 5.2 Experimental apparatus: (a) Experimental Setup; (b) Schematic

technique. Therefore, it is unlikely that the cutting technique affected the results in this study.

A load cell (LUX-B-100N-ID, Kyowa Electronic Instruments Co., Ltd.) situated on one of the stages monitors the load applied to the specimen during the experiment. The nominal stress is calculated by dividing the applied load by the initial cross sectional area of the specimen. Combined with the known displacement that is applied at a given time, this allows to trace the stress-strain curve of Nafion as the experiment progresses. The specific dissipated energy is then calculated from those results as

$$w_F = \frac{1}{lt}\int \sigma(\varepsilon) \cdot d\varepsilon \qquad (5.5)$$

dividing the dissipated energy by the total crack area.

5.3. Results and discussion

5.3.1. Ambient conditions

In general, all specimens in this study underwent ductile failure. This is understandable by the shape of the stress-strain curves obtained, some of them being presented in Fig. 5.3. Ductile failure is characterized by a smooth curve, where once the crack is initiated the elastic energy stored in the material is released, helping the crack to propagate in a progressive way. On the contrary, a brittle failure would show a sharp drop in the measured stress as the crack would propagate very quickly through the specimen[108]. Nevertheless, the ligament length has an effect on the shape of the stress-strain curve: a longer ligament length is associated with a lower maximum stress, a higher crack initiation strain and a higher rupture strain. This is explained by how much of the ligament has yielded at the time of crack initiation and propagation. As noted in the section describing the DENT test protocol, it is often observed during DENT tests that the ligament is not fully yielded at the time of failure. This is especially true the longer the ligament, since the plastic zone first develops around the notch tips and develops from there. In the case of short ligaments, the full section of the specimen will be yielded. Conversely, the longer the ligament, the smaller the plastic zone will be when compared to the length of the ligament. This results in generally smaller stresses along the ligament, while at the same time the specimen will be allowed to deform more before failure happens.

Figure 5.4 (cross symbols) shows the results of the DENT tests performed in ambient conditions (30°C, 50%RH). As expected from Eq.(5.4), the measured dissipated energy increases with the ligament length in a linear fashion. The linear regression shows a value at the origin of 18.4 kJ m^{-2} (the EWF) and a slope of 13.6 kJ m^{-3} (the increase rate of plastic dissipated energy)

The only value found in the literature for the EWF of a Nafion membrane with the DENT test is 20.5 kJ m^{-2} in ambient conditions[110]. This value is somewhat higher than the one found here, however the authors note that considerable viscous and plastic deformations dominated the fracture process. There was no mention of whether the failures happened in a ductile or brittle manner, which would have been of interest since ligament lengths greater than a third of the specimen width were used. The difference of crosshead speed during the experiment might also be another factor explaining the discrepancy.

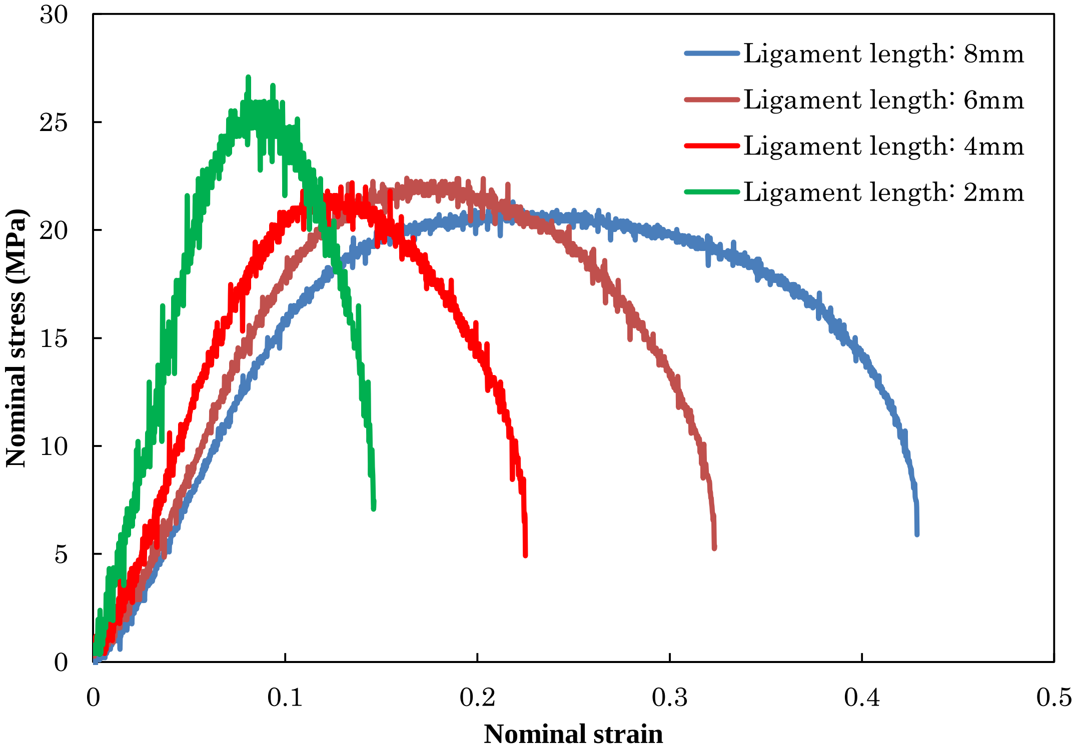

Fig. 5.3 Result of DENT experiment on Nafion specimen at ambient conditions for different ligament lengths

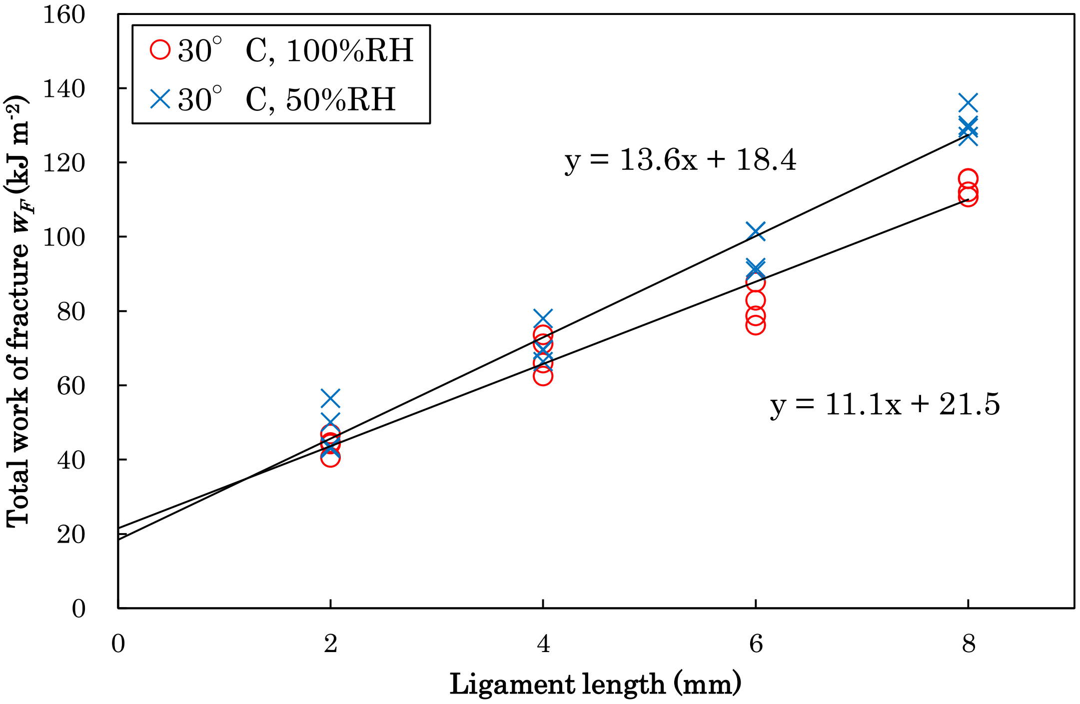

Fig. 5.4 Total Work of Fracture calculated for different ligament lengths at ambient temperature (30ºC). The linear regression shows a EWF of 18.4 kJ m^{-2} at ambient humidity and 21.5 kJ m^{-2} at high humidity

5.3.2. High humidity, ambient temperature

The same set of data was gathered for high humidity conditions (30°C, 100%RH). The results are synthesized in Fig. 5.4 (round symbols). Compared to the previous case, the data is less scattered, with results clustering more closely along the trend line. The EWF obtained by the experiments is 21.5 kJ m^{-2}, which is close to the EWF calculated for ambient temperatures, though a bit higher. In contrast, the slope of the linear regression is lower for high humidity than for ambient conditions, indicating a lower amount of plastic dissipated energy. This is linked to the change of mechanical properties of Nafion in humidified states: they provoke a lower yield stress and a higher yield strain in the material, but also a higher rupture strain[111], as also discussed in Chapter 2. These two factors have opposite effects on the plastic energy being dissipated. Overall, the lower dissipation energy found in the experiments suggests that the lower yield stress and flow stress after yielding in the material is the dominant effect to lower dissipation energy.

5.3.3. High temperature

The experimental results for high temperature conditions differ from the previous cases in that the dissipated energy does not follow a linear law. Instead, the data seems to follow a square law, with values of w_F increasing faster the longer the ligament length. This holds true for both high and ambient humidity. Meanwhile, the effect of humidity seems to be the same as in ambient temperature cases: higher humidity results in a slightly lower dissipated energy, with the difference increasing monotonically with the ligament length. Those results are shown in Fig.5.5.

Trying to fit the data with a linear regression would lead to a negative value for the EWF, which is obviously incorrect. This suggests that in this case the shape factor of the plastic zone β (see Eq. 5.4) becomes geometry-dependant and therefore varies with the ligament length l.

As mentioned earlier, the dissipated energy will increase linearly with the ligament length as long as the specimen failed in a ductile manner. A brittle fracture, as is more often observed for longer ligaments, results in less plastic energy being dissipated, leading to lower dissipated energies than a linear regression would expect[108]. Inversely, ductile fracture is associated with necking of the specimen, followed by cavitations before cracks start to appear. Both the experimental stress-strain curves (Fig. 5.3) and the fracture profile of the failed specimens (Fig. 5.6) indicate that all the specimens in this study failed in a ductile manner. However, as readily visible in Fig. 5.6, the specimens tested at high temperature show significantly more necking than those tested at ambient temperature. This difference in level of ductility justifies the greater amount of plastic dissipated energy in those cases. The underlying reason for this would be that at the temperature tested (80ºC), Nafion enters its glass transition, which is associated with higher ductility of the material.

It has been noted earlier that in high humidity cases the decreased stress in the material was the dominant effect over the increased rupture strain, leading to lower dissipation energies. While temperature and humidity have been noted to have the same qualitative effects on the material properties of Nafion[111], the higher dissipated energies indicate that in the case of high

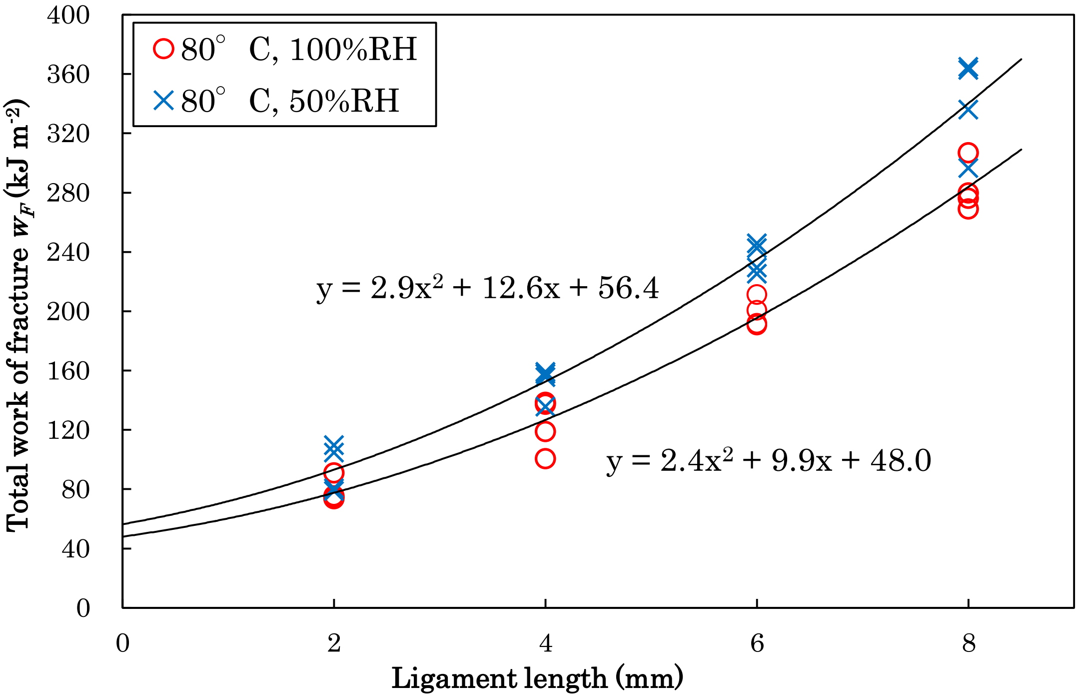

Fig. 5.5 Total Work of Fracture calculated for different ligament lengths at high temperature

(80ºC)

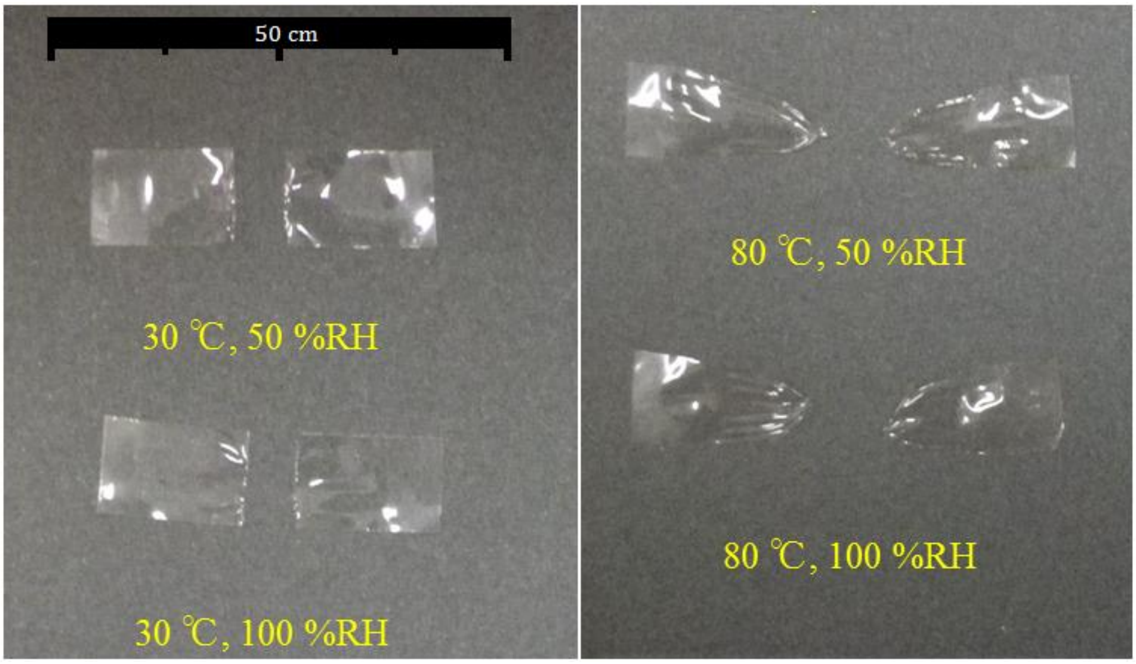

Fig. 5.6 Overview of the 8mm ligament length fractured specimens for different environmental conditions

temperature the dominant effect becomes the increased rupture strain: despite the strains in the material being lower, the larger deformations sustained before failure result in more energy being dissipated overall.

A numerical simulation of this experiment allows to visualize the distribution of stresses in the specimen during the experiment, clarifying this phenomenon. This will be discussed in the next chapter.

5.4. Local observation of the fracture surfaces

In order to supplement the observation of specimens from Fig. 5.6, a local observation of the fracture surfaces was realized using a scanning electron microscope. The results are presented in Fig. 5.7.

Figure 5.7 (a) and (b) shows the two high temperature specimens, magnified 200 times. In both cases, there is large scale plastic deformation occurring along the length of the specimen. Furthermore, the fracture surface is undulated, indicating that the specimens buckled under the Poisson effect during the experiment. Those undulations are more prominent in the high humidity case. These two effects, large scale deformation and buckling, confirm the previous observations and explain the higher amount of plastic dissipated energy in the high humidity cases, and why the results are qualitatively different depending on the humidity level: the low temperature specimens do not show any amount of out-of-plane deformation.

Figure 5.7 (c) through (f) gives a better look of all fracture surfaces with a 1000x magnification. There, the effects of humidity can be seen: while the ambient temperature, high humidity case shows a relatively smooth fracture surface, all other cases have rougher and more damaged fracture surfaces. Regardless of temperature, the fracture surface in ambient humidity cases appear more damaged than in the corresponding high humidity case. Thus, the difference in the work of fracture between ambient and high humidity cases can be attributed to an increased amount of surface damage taking place during the experiment.

In order to quantify the roughness of the fracture surfaces, specimens were observed with a laser microscope with depth selectivity. Figure 5.8 compares the results at high temperature between ambient and high humidity. In both cases the defects on the surface appear to be around 1 to 2 micrometers in depth, however their distribution varies depending in the humidity: in the ambient humidity case the surface defects are more densely distributed, while in the high humidity case the surface seems to present less defects overall.

Roughness only appears locally along the ligament, so it is understandable that its effect would be much smaller than the large scale plastic deformation observed in higher temperatures. Overall, the local observation of the fractured surfaces gives a qualitative explanation to the differences in the total work of fracture in the different cases that were tested.

5.5. Essential and Non-essential work of fracture

This section discusses the remarks that can be made on the works of fracture of Nafion based on the previous paragraphs.

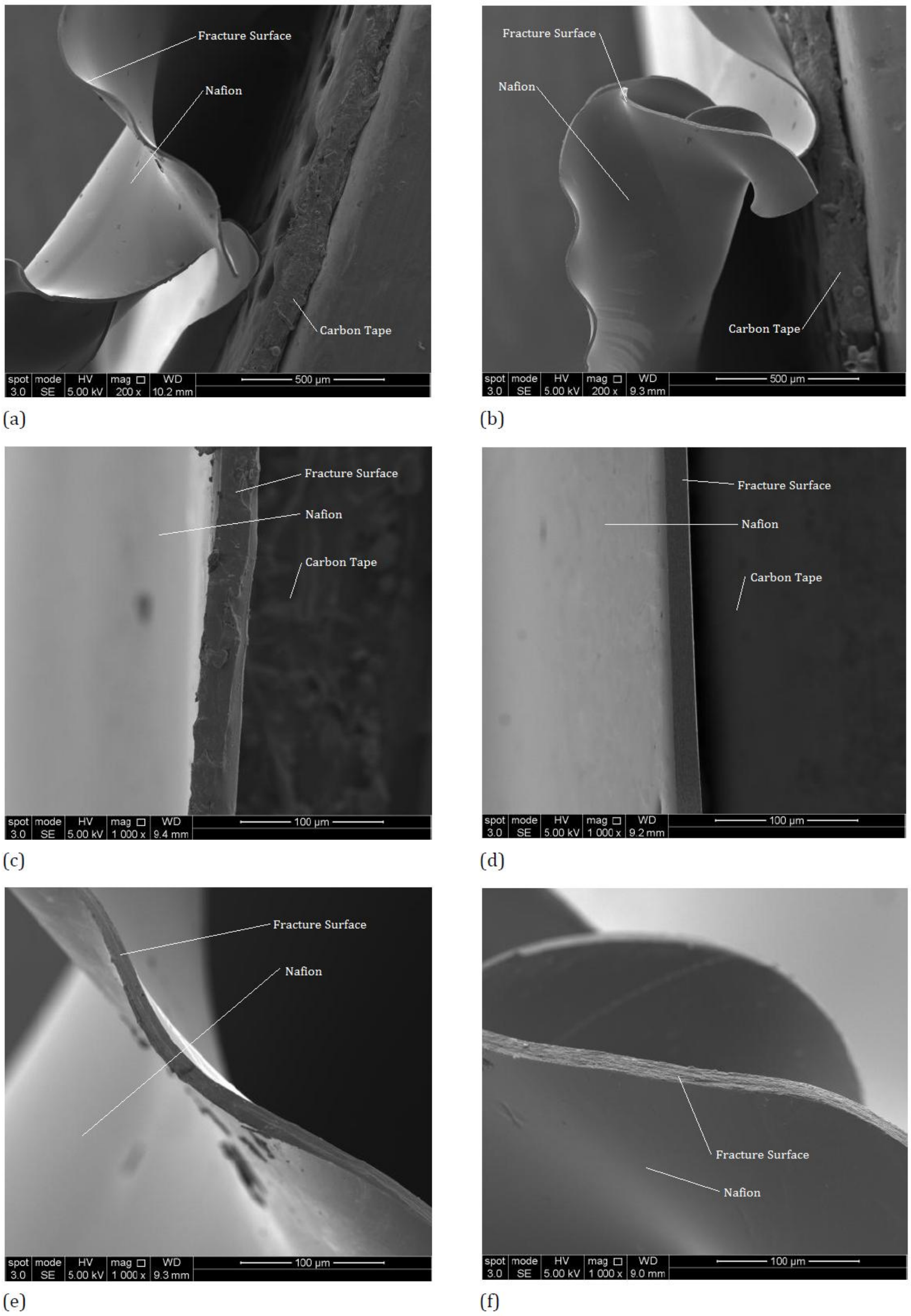

Fig. 5.7 Scanning electron microscope observation of the fracture surface of 8mm ligament length specimens: (a) 80ºC, 50%RH, 200x; (b) 80ºC, 100%RH, 200x; (c) 30ºC, 50%RH, 1000x; (d) 30ºC, 100%RH, 1000x; (e) 80ºC, 50%RH, 1000x; (f) 80ºC, 100%RH, 1000x

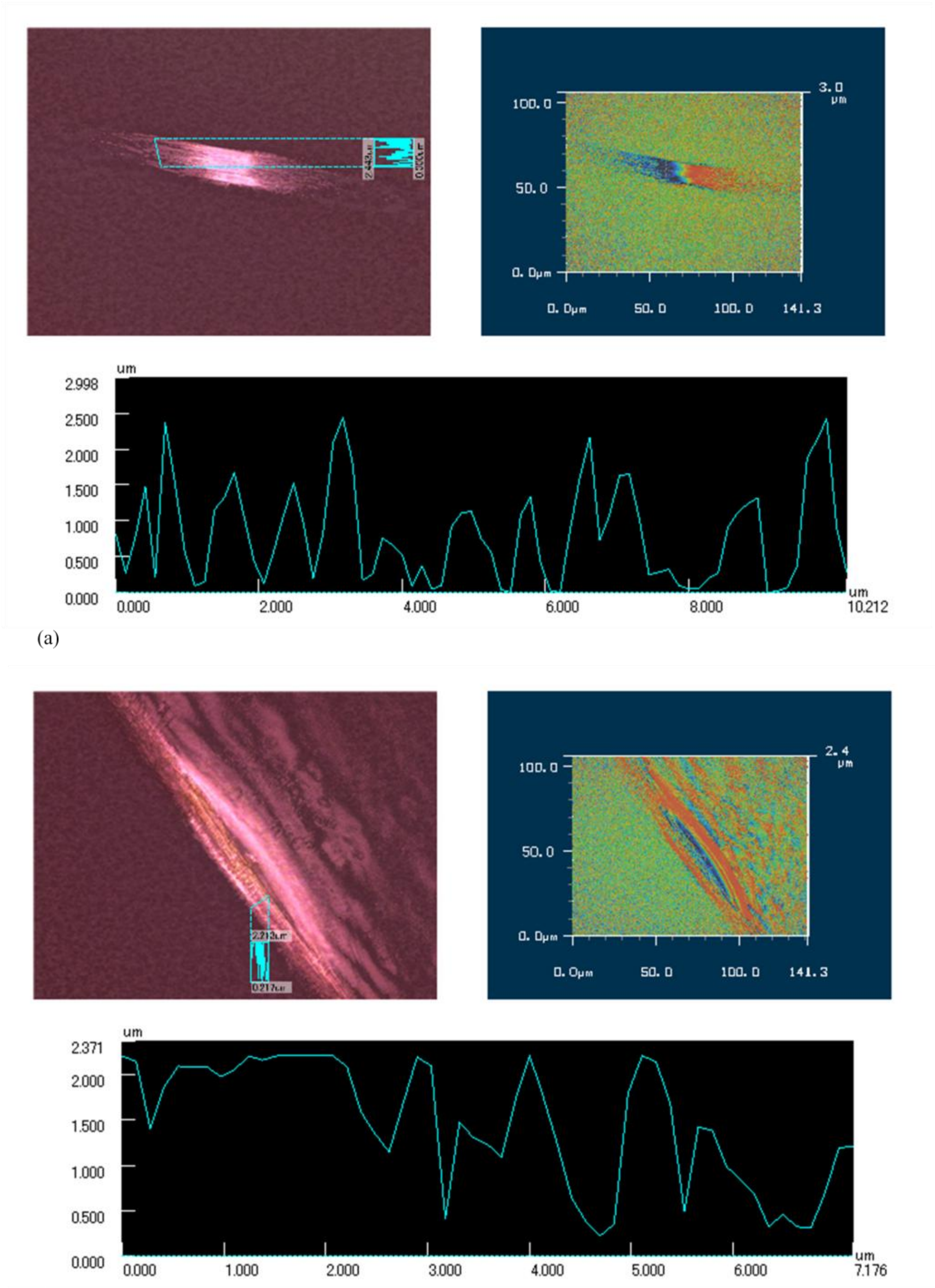

(a)

(b)

Fig. 5.8 Laser microscope observation and profiling of the fracture surfaces: (a) 80ºC, 50%RH; (b) 80ºC, 100%RH

The membrane's sensitivity to changes of temperature is clear, with a great increase of dissipated energies at higher temperatures. The sensitivity to humidity is less pronounced but still present: in all the tested cases, the dissipated energy decreases when the humidity increases. Because of this, it would seem natural that the EWF would follow the same pattern, and while this is what is observed with respect to temperature, the EWF at ambient humidity is measured higher when humidity is high. The difference is small however, with a difference of only 3.1 kJ m^{-2}. This stands within experimental error, as it is smaller than the standard deviation of the dissipated energies calculated from the experimental curves.

By subtracting the EWF from the values of the dissipated energy, it is possible to isolate the non-essential work of fracture, as shown in Fig. 5.9. This corresponds to the energy lost in plastically deforming the ligament and its close surroundings, as well as tearing and possible creep and friction around the crack. The evidence of these effects is discussed above in the local observation of the fracture surfaces. Since these effects decrease as the ligament length becomes smaller, eventually disappearing when the length nears 0, the fitting curves in Fig. 5.9 all tend towards 0 for ligament lengths of 0. As expected, the effects of temperature and humidity are the same on the non-essential work of failure as on the EWF.

From the point of view of fracture resistance, the value which holds the most interest is the lowest value of the EWF across all conditions, as this is the case where cracks will most easily propagate. The lowest value that was found in this study was 18.4kJ m^{-2} in ambient conditions. In order to mitigate the development of defects in the proton exchange membrane, it would

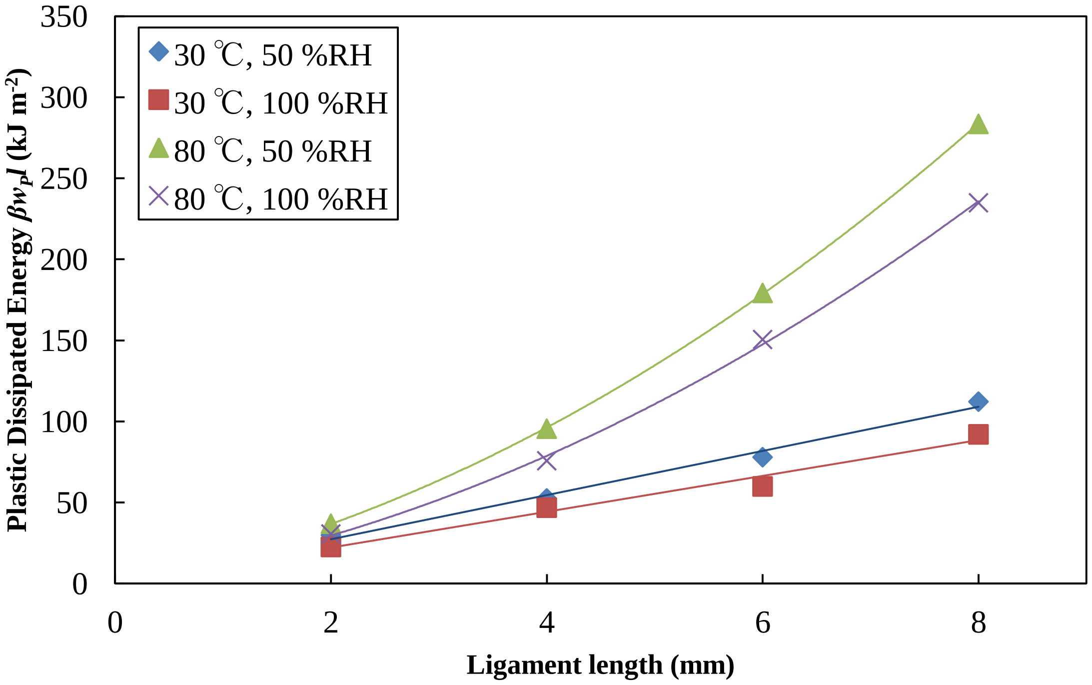

Fig. 5.9 Non-essential work of fracture, each data point corresponding to the average of all four tested specimens for each case

therefore be advantageous to use this value as a reference during design of the MEA.

5.6. Summary

This study focuses on the EWF of Nafion membranes, and how it relates to the environmental condition surrounding the membrane. In order to get insights that are useful for the purpose of fuel cells, the most prominent use of proton exchange membranes, several types of conditions were considered: ambient conditions, representing the fuel cell in an idle state; high temperature, representing the cell after start-up when the temperature has to be increased in order for the nominal efficiency of the reaction to be reached; and high humidity, which happens as a result of the water formed as a by-product of the reaction. The EWF was calculated using the DENT test protocol.

Table 5.1 summarizes the values of the EWF found from the experiments. Results show a great sensitivity to environmental conditions, especially to increases of temperature. While the EWF in ambient conditions was found to be 18.4 kJ m^{-2}, it more than doubled at high temperature to values of 48.0 kJ m^{-2} (ambient humidity) and 56.4 kJ m^{-2} (high humidity). In both cases this represents a 160% increase of the EWF compared to ambient temperature. Humidity was found to have a similar effect but less pronounced, the increase being limited to 17-18% compared to cases of ambient humidity. The local observation of the fractured specimen gives insights about what causes these differences: in high temperature cases, significant plastic deformation and buckling is visible along the ligament length. Concurrently, lower humidity seems to result in increased roughness of the fracture surface. Since the surface damage is much more localized than the buckling, the temperature ends up having a larger impact on the work of fracture than the humidity.

The plastic dissipated energy in ambient temperature cases followed the expected linear law with respect to the ligament length; however it assumed a quadratic pattern in cases of high humidity. Given Eq.(5.4), this change of behavior comes from a modification of the shape factor β, meaning that the shape of the plastic zone is dependent on the temperature of the material. This in turn can be attributed to the fact that Nafion undergoes its glass transition at the high temperatures tested, resulting in some structural changes in the polymer as well as in a much increased ductility. The effects of temperature on the stress distribution of Nafion, and how it relates to the measured plastic dissipation energy, are discussed in depth in the next chapter.

It was found that the EWF of Nafion was at its lowest in ambient conditions. At high temperatures, the much increased EWF of Nafion means that it necessitates more energy to break, reducing crack propagation. Inversely, even though ambient temperatures would seem to be gentler conditions for the membrane, these conditions actually favor crack propagation. The minimum value found for the EWF, 18.4kJ m^{-2}, is therefore the most relevant value from the point of view of fracture resistance, and the one that should be retained when estimating the lifetime of a Nafion membrane.

Table 5.1 EWF of Nafion in different environmental conditions

EWF	Ambient Temperature (30°C)	High Temperature (80°C)
Ambient Humidity (50%RH)	18.4 kJ m^{-2}	48.0 kJ m^{-2}
High Humidity (100%RH)	21.5 kJ m^{-2}	56.4kJ m^{-2}

CHAPTER 6

Numerical estimation of the Essential Work of Failure of Nafion by Finite Element Analysis

In the previous chapter, the EWF of Nafion was calculated by using a DENT test, and a discussion was given about the effects of temperature and humidity on its fracture resistance. This chapter aims to complement these findings by developing a Finite Element Analysis to provide an alternative method of calculating the work of fracture.

6.1. Motivation for the Finite Element Analysis

This study investigates the essential work of fracture (EWF) of the proton exchange membrane in a variety of environmental conditions relevant to the actual function of the fuel cell. This fits into the bigger scope of the thesis, which is to gain a comprehensive understanding of the mechanisms of failure of the MEA. A concrete application of this understanding is to develop models that are reliable in simulating the behavior and failure of the MEA in a variety of circumstances. Such models would have the advantages of being more flexible and less resource intensive when compared to series of experiments. In all fields of engineering numerical simulations are already being taken advantage of thanks to that.

In that optic, the motivation for replicating the DENT experiments with a Finite Element Analysis is twofold:

- It provides a proof of concept that the constitutive models developed in this study are accurate and that it is feasible to apply these models to complex systems such as the fracture of the MEA.

- By taking advantage of the visualization tools of the FEA, it allows further discussion about the work of failure of Nafion. Notably, by observing the stress distribution in the membrane around the crack tip, it becomes possible to elucidate the qualitative change in the work of failure that was observed and described earlier in Section 5.3.3.

6.2. Finite Element Model

In this study, a numerical scheme is proposed in order to calculate the EWF. This method has the advantage of only needing a single experimental input: the applied strain at the time of fracture for a given ligament length. The material used in this study is Nafion, for which the constitutive model is the one proposed in Chapter 4. Since the failure of Nafion needs to be simulated, it is necessary that the model stays accurate even at high strains.

6.2.1. Method of calculating the EWF

The Finite Element Model aims to simulate a DENT test, and so it is necessary to model the behavior and crack propagation of a DENT test specimen (see Fig. 5.1) subjected to a tensile strain. Figure 6.1 shows the model that was used in this study. The analysis was made using the finite element code ABAQUS/Standard. Eight-node brick elements (C3D8) are used in the entire model, and a cohesive zone model is applied to the boundary elements. Because of symmetry, only one half of the model needs to be created. Even though the conditions are also symmetrical along the length of the specimen, the progression of the crack along the plane of symmetry makes it necessary to model both sides of the specimen. As shown in Fig 6.1 (a), the upper and lower edges of the specimen were constrained to move in the tensile direction, while other edges were left free.

Since one of the objectives of this model is to be able to reproduce experimental results, several specimens are created with different ligament lengths, allowing calculating the EWF with a linear regression in the same way than in the experiment. The proposed mesh is more refined around the notch tip and crack propagation path (see Fig 6.1 (b)), so the total number of elements will differ depending on the ligament length, in any case the elements along the cohesive zone measure 0.01mm in length.

6.2.2. Cohesive Zone Model

The characterization of the cohesive zone in the model is of particular importance here as this is what will define the fracture behavior in the simulation. In addition to that, analyzing the results for a given cohesive zone model can provide insights for an experimental protocol that diminishes unwanted effects such as plastic deformation or friction.

The model employed here uses a traction-separation law with a maximum stress criterion, as shown in Fig. 6.2. Cohesive elements become separated after the maximum stress has been reached. As there is not currently enough published data on the fracture of Nafion, the failure criterion needs to be first estimated through experiment. Three parameters intervene in the traction-separation law: the crack initiation displacement δ_0, the maximum stress T_{max} and the displacement at complete failure δ_{max}. In the chosen model, the traction increases gradually to reach its maximum T_{max} once the displacement reaches δ_0. Traction then decreases linearly until it reaches a value of zero at displacement δ_{max}. Since the constitutive model for Nafion has already been established, T_{max} can be calculated from δ_0. Since it would depend on the stress profile of the specimen and therefore on the specimen geometry, T_{max} needs to be recalculated for each ligament length. Setting $\delta_{max} = \delta_0$ was found to give satisfying results, and so the elements are set to become separated as soon as the maximum stress has been reached. Therefore, the only experimental input that is needed is the crack initiation displacement, which is easily identified as the displacement for which the maximum stress is reached before cracking starts to occur, as exemplified in Fig 6.2(b) and denoted by ε_C in Fig.6.4.

The crack initiation strain can be seen in Fig. 6.3 to vary linearly with the ligament length, making it in theory possible to extend simulations to ligament lengths not experimentally tested. Notably, the crack initiation strain for a theoretical ligament length of 0 does not go to 0. This minimum value of the crack initiation strain is calculated to be $\varepsilon_{C,0} = 0.036$, and can be linked to

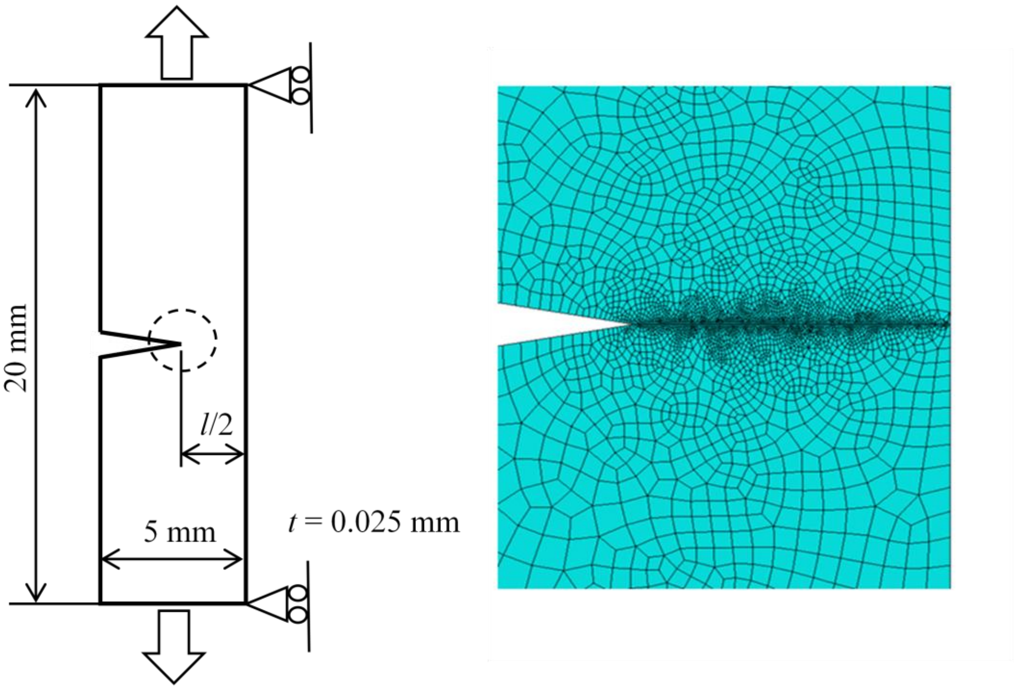

(a) (b)

Fig. 6.1 DENT test specimen: (a) Calculation model with boundary conditions; (b) Detail of mesh around the notch tip

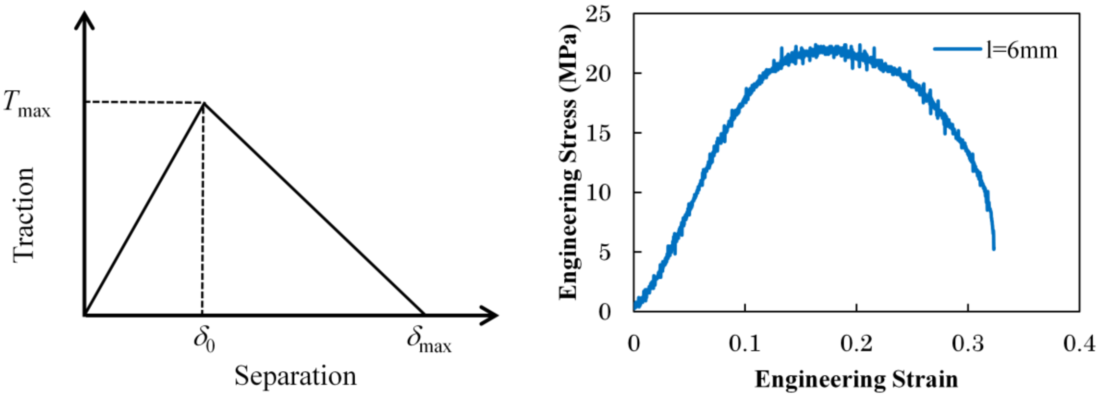

(a) (b)

Fig. 6.2 (a) Representation of a traction-separation law; (b) Typical stress-strain curve for the specimen in a DENT test the Crack tip Opening Displacement.

In the case of the DENT experiment, friction was found to not have any appreciable effect on the fracture energy being dissipated. Any frictional effect introduced in the cohesive zone model would only account for variations of the calculated dissipated energy of less than a percent, well below experimental error. This is because the failure happens primarily by tearing, where frictional forces are only marginal.

6.3. Results and discussion

6.3.1. Ambient conditions

Having derived the values for critical strain from the experiments, the finite element model was used with the objective of replicating the experimental results. It is worth noting that in all cases, the true stress calculated at the notch tip at the time of failure is found to be close to the maximum stress of Nafion as indicated on the material data sheet (an engineering stress of 23MPa). Overall, the simulation seems to fit the experimental stress-strain curve well, as shown in Fig.6.4.

Figure 6.5 (a) shows the dissipated energies calculated by the FEM for ambient conditions, and compares it to experimental results. For all simulations, the calculated dissipated energy was within experimental error. The linear regressions for the experiment and simulation are in agreement with values at the origin (the EWF) of 18.4 kJ m^{-2} and 18.5 kJ m^{-2} respectively; and very close slopes (the plastic dissipated energy).

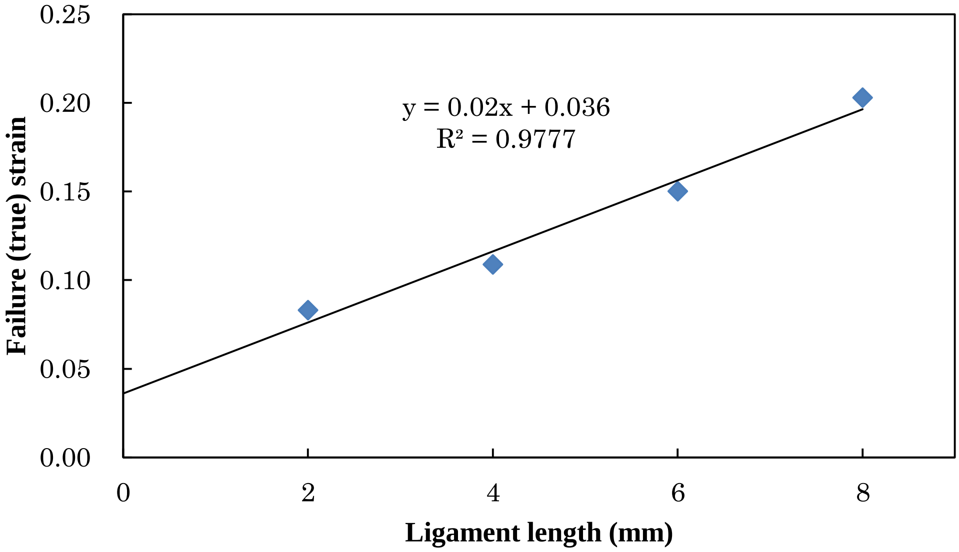

Fig. 6.3 Evolution of experimental critical strain ε_C with ligament length

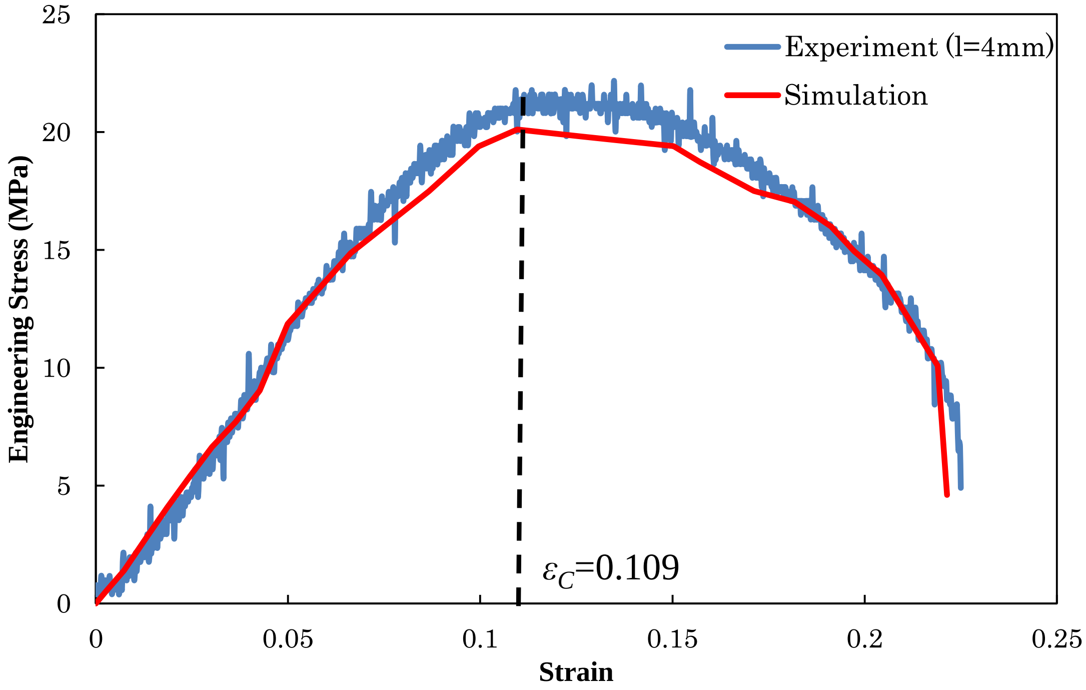

Fig. 6.4 Stress-Strain curve for Nafion during a DENT test

6.3.2. *High humidity, ambient temperature*

The same set of data was gathered for high humidity conditions (30°C, 100%RH). The critical strains are assumed to be the same than in the previous case. The results are synthesized in Fig. 6.5 (b). The agreement between the experiment and the simulation is still good, particularly with the slope of the linear regression, though the simulation data is more scattered than in the previous case. The EWF obtained by the experiments is 21.5 kJ m^{-2}, while the numerical simulation gives a value of 16.8 kJ m^{-2}. Both of these values are close to the EWF calculated for ambient temperatures. In contrast, the slope of the linear regression is lower for high humidity than for ambient conditions, indicating a lower amount of plastic dissipated energy. This is expected, as Nafion becomes more compliant in humidified states. This implies a lower yield stress in the material, and consequently a lower plastic energy being dissipated.

6.3.3. *High temperature*

The experimental results for high temperature conditions (regardless of humidity) differ from the previous cases in that the dissipated energy do not follow a linear law. Instead, the data seems to follow a square law, with values of w_F increasing faster the longer the ligament length. There is no appreciable difference in experimental results between the ambient humidity case (80ºC, 50%RH) and the high humidity case (80°C, 100%RH), as indicated by the similar experimental results in both situations. The results from the simulation show the same behavior, as is shown in Fig.6.6.

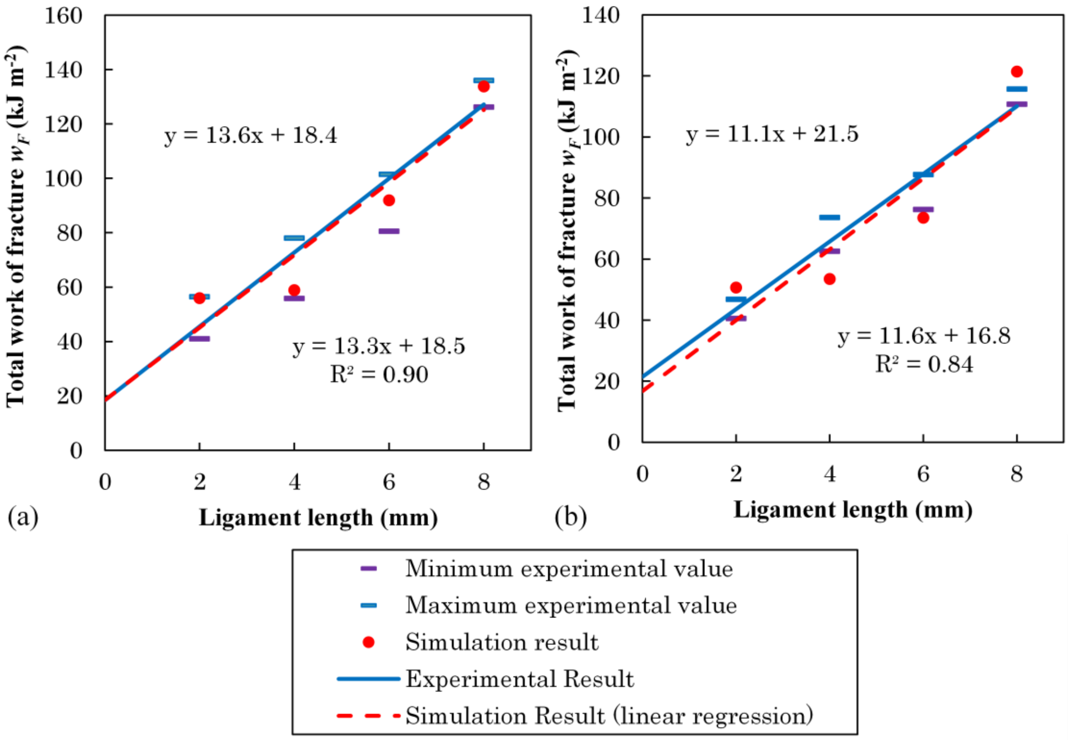

Fig. 6.5 Total Work of Fracture calculated for experiments and simulations for different ligament lengths: (a) at ambient conditions (30ºC, 50%RH); (b) at high humidity (30ºC, 100%RH)

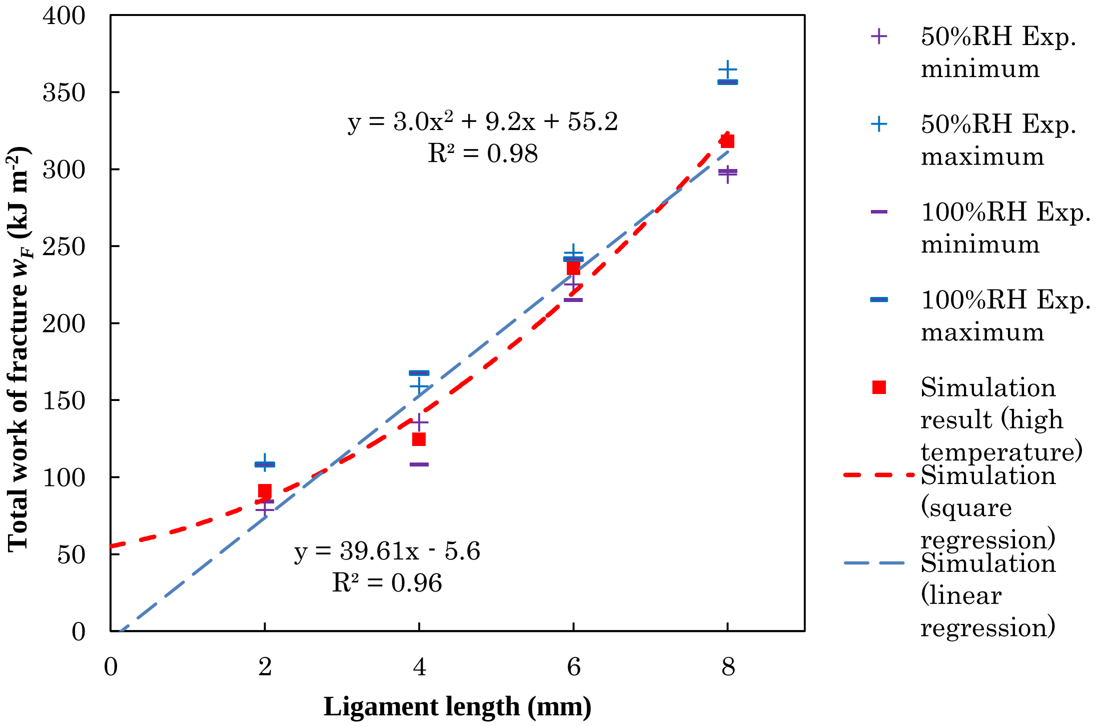

Fig. 6.6 Total Work of Fracture calculated for experiments and simulations for different ligament lengths at high temperature (80ºC)

As mentioned earlier, it has been noted in previous studies[108] that the linear regression was assured as long as the specimen failed in a ductile manner. A brittle fracture, as is more often observed for longer ligaments, leads to lower dissipated energies than a linear regression would expect. In this study, the stress-strain curves of the DENT tests suggest that all specimens undergo ductile failure. However, at the temperature tested (80ºC), Nafion enters its glass transition, which is associated with higher ductility of the material.

6.4. Effect of the size and shape of the plastic zone

In order to clarify this phenomenon, the size of the plastic zone was investigated. The calculated length and width of the plastic zone at the onset of failure were retrieved using the results from the finite element analysis. These are shown in Fig.6.7 and compared between cases of high temperature and of ambient conditions.

Several observations can be made from these measurements. Firstly, the specimens at ambient conditions present plastic zones with almost identical widths and lengths. This means that the plastic zone keeps a symmetrical shape for all ligament lengths. This is congruent to plane stress conditions[112], satisfying the plane stress assumption of the DENT test. The second observation is that the plastic zones for all conditions are close for small ligament lengths ($W <$ 4mm) but difference grows the longer the ligaments. The plastic zones in the cases of high humidity become larger and more elongated, possibly indicating that a plane stress to plane strain transition has occurred. Also, the larger plastic zones are congruent with the larger amounts of

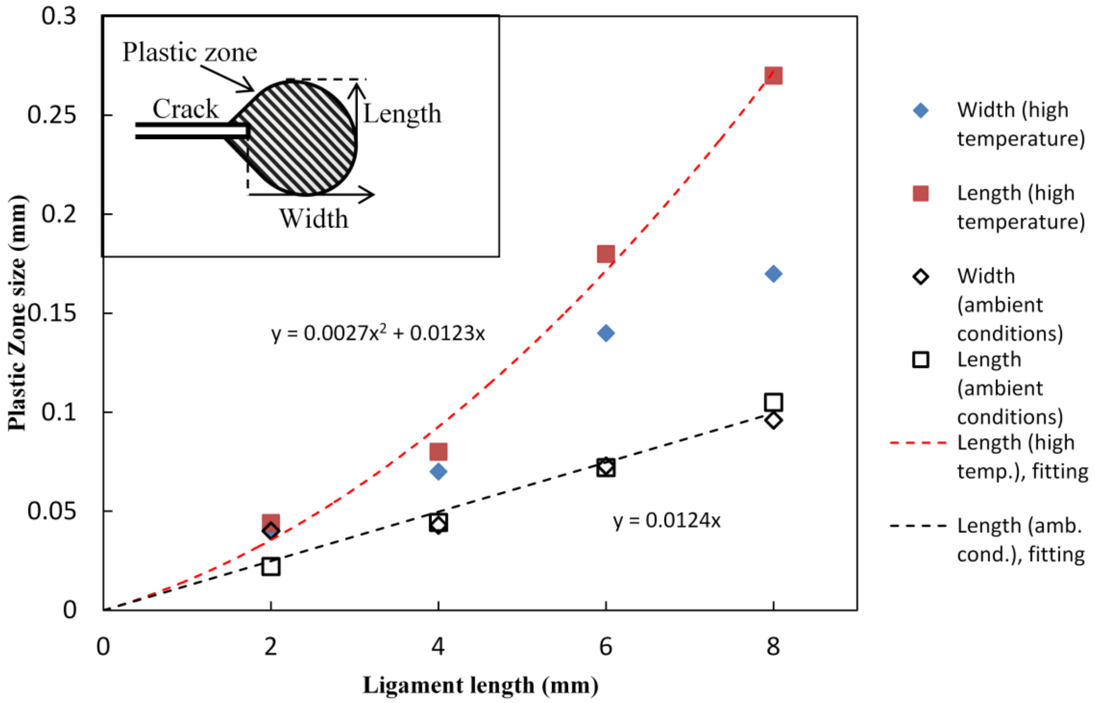

Fig. 6.7 Dimensions of the plastic zone at the onset of failure at high temperature (filled symbols) and ambient conditions (hollow symbols). Insert: points of reference to calculate width and length of the plastic zone

dissipated plastic energy.

In Eq.(5.3), the volume of the plastic zone was written as $\beta l^2 t$. In this formulation, β is the shape factor of the plastic zone, which verifies

$$\beta \propto \frac{h}{l} \tag{6.1}$$

where h is the length of the plastic zone and l the ligament length.

In ambient conditions, h is proportional to l, as shown in Fig.6.7. This results in β being independent from l, justifying the fact that the w_F term from Eq.(5.4) is a linear function of l.

In the high temperature case, however, h is no longer proportional to l but instead is closer to a quadratic function of it. Thus β itself becomes a linear function of l. Following Eq.(5.4), we finally get the result that w_F has become a quadratic function of l, explaining the results from Fig.5.5 and Fig.6.6.

These changes in the geometry of the plastic zone only affect the plastic dissipated energy. Although it is no longer proportional to the ligament length, it is still possible to calculate the EWF by extrapolating the results to a length of 0, this time using a quadratic regression. Using this different approach, the EWF of Nafion at high temperature can be estimated at 55.2kJ.m^{-2}, according to the results of Fig.6.6. This figure is roughly 2.5 times the EWF found in the two previous cases.

A hypothesis to explain this change is that the glass transition that Nafion undergoes at the high temperature tested affects its higher order structure. This causes ductility to increase, some cross-linking to happen, making the specimen more compliant and therefore harder to fracture.

6.5. Summary

In this chapter and in the previous one, the EWF of Nafion membranes was investigated. The chosen approach uses a DENT test in different environmental conditions in order to investigate the effect of these conditions on the EWF. In order to complement these results, a finite element model was developed, giving additional insight on the behavior of Nafion during a DENT test. The constitutive model of Nafion developed in Chapter 4 was successfully implemented and the results of the FEM were shown to be close to experimental results.

A discussion on the effects of environmental conditions on the EWF of Nafion was already given in the previous chapter. However, the FEM allowed to elucidate the reason why the high temperature cases were qualitatively different than at ambient temperature. The study of the distribution of plastic strains revealed that this was due to the shape of the plastic zone becoming a function of the ligament length. The EWF in these cases was found to be larger than in previous cases, with a value of 55.2 kJ m^{-2}. This can be attributed to a much increased ductility of Nafion at temperatures that surpass its glass transition. An important consequence of this change in the EWF is that cracks will more readily propagate in Nafion at lower temperatures. Even though higher temperatures would seem to be harsher conditions for the function of the cell, they represent the best case scenario when it comes to crack propagation. This suggests that from the point of view of fracture resistance, design of the MEA would be best done with ambient conditions in mind.

The FEM was found to closely reproduce the experimental DENT test results. The only parameter that is needed in order to simulate the fracture is the critical stress of the cohesive zone, which can be simply obtained through experiment. Because of this, the proposed method is significantly quicker in calculating the EWF than the alternatives found in the literature. This method also opens the door for further investigation, such as investigating the effect of the notch shape, load history or a variety of other parameters relevant to estimating the durability of proton exchange membranes.

CHAPTER 7

Conclusion

7.1. Novel aspects of this research

This thesis focused on two areas regarding Membrane Electrode Assemblies. The primary aim was to gain a thorough understanding of the mechanical behavior and failure of MEAs. The other objective was to develop numerical models that would allow to accurately simulate this behavior. These results provide tools that are useful to make more informed and accurate predictions of the lifetime of MEAs.

For the systematic study of the mechanical properties of the MEA that was conducted during the research, it was necessary to take into account at all times the environmental conditions surrounding the materials. It was demonstrated in multiple cases throughout the study how much these parameters affect the behavior of the membranes, both qualitatively and quantitatively.

The failure of the MEA was examined both from the point of view of crack initiation and crack propagation. Both of these stages are relevant to predict the lifetime of the MEA. The approach chosen to study the crack initiation was fatigue testing, since mechanical fatigue is the primary concern for the durability of the MEA. For the crack propagation phase, the Essential Work of Failure was investigated.

In parallel, finite element analysis was used to supplement the experimental results. Constitutive models were introduced for the materials that compose state-of-the-art MEAs. These models were shown to accurately estimate the behavior of the MEA in a variety of applications, and to accurately predict its failure. These results open the door to a variety of applications for these models, which should help make further prediction about the lifetime of MEAs.

There are two strategies to extend the lifetime of MEAs in PEMFCs: the first is to postpone the apparition of cracks in the CL (see Fig. 1.4(b)); the second is to slow down the propagation of these cracks (Fig. 1.4(c) and (d)). Naturally, these two approaches can be used concurrently. At the design stage of the MEA, numerical models can be used to ensure that the plastic dissipation energy does not exceed the critical value of D_c proposed in Chapter 3. The second approach is to optimize the cell for environmental conditions where the fracture resistance of the membrane is higher, thus slowing crack propagation. In particular, the large impact of temperature on the EWF of the membrane that was demonstrated in Chapters 5 and 6 can be taken into account when designing thermal management for the cell.

Another use of the results proposed in this dissertation is for material selection. As laboratories are still trying to develop new materials for improved performance of fuel cells, their resistance to fracture and crack propagation can be used as another basis of comparison between competing materials. As these parameters directly influence the lifetime of the materials within a PEMFC, and therefore their cost-effectiveness, they are a critical factor to take into account.

7.2. Research achievements

The mechanical behavior of MEAs was tested for various environmental conditions relevant to the function of a fuel cell. It was found that in general, increased values of temperature and humidity made both Nafion and the Catalyst Layer more compliant, with humidity having the most pronounced effect. This effect carried over to the tensile failure: higher temperature and humidity was linked to lower crack initiation strain and stress.

This sensitivity to environmental parameters is what led the author to select an energy-based criterion for predicting the onset of failure in cyclic experiments. Where a critical stress would need to be recalculated for each set of experimental parameters, the critical value of plastic dissipated energy is independent from them. The author proposed that the onset of failure in the CL is reached once the plastic dissipated energy reaches D_c = 12.4 MJ.m^{-3}. This criterion was shown to accurately match experimental results. Using a numerical simulation, it was hypothesized that micro-cracks form in the CL during humidity cycles due to decohesion between Nafion and the carbon black.

On the subject of crack propagation, several results are obtained. The essential work of failure of Nafion was found to be heavily dependent on both temperature and humidity. However in contrast to what was observed during tensile behavior, temperature had the most noticeable effect. Indeed, at high temperature the more rubbery behavior of Nafion resulted in a greatly increased work of failure and indicated a transition from plane stress to plane strain conditions. Aggregating all results, the lowest value for the EWF calculated across all tested configurations was w_F = 18.4 kJ.m^{-2}. This was the value found for ambient conditions, indicating that Nafion is more prone to crack propagation when left at ambient temperature and humidity.

The other stated objective of the study was to develop numerical models that would be accurate in simulating the behaviors of the MEA in a variety of situations. Constitutive models were proposed for both Nafion and the CL, and were shown to reproduce experimental results with satisfying precision. In the case of Nafion an existing constitutive model that was found in the literature was adapted to accurately estimate the stress-strain behavior over the whole range of strains of the material. This constitutive model was successfully used to simulate a DENT test and estimate the EWF of Nafion, confirming the accuracy of the model and its usefulness in practical applications.

The mechanical properties, the crack initiation and the crack propagation stages are all important to take into account when considering the lifetime of the MEA. Naturally, a better understanding of the properties of the MEA is crucial from the point of view of safety and cost, and therefore the author hopes that the results presented in this study will help the fuel cell technology to become ever more competitive in the domain of power generation.

7.3. Future research

In the course of this thesis several opportunities for further research were identified. While the fuel cell technology and in particular fuel cell vehicles have received a lot of attention in the recent years, still more work is needed before it can gain mainstream adoption.

In this study, the mechanical properties of the MEA were discussed. In the future, the scope could be extended to include other components of the fuel cell, notably the gas diffusion layer and the bipolar plates. Similarly to the MEA, the materials forming these components are selected from the point of view of power generation, and therefore focus on their chemical and thermal properties. Data on the mechanical properties and degradation of these materials in the context of a fuel cell is still lacking. While the MEA is typically the limiting factor for the durability of the cell, being able to better estimate of the lifetime of other components would still be an important asset.

Regarding the MEA itself, the catalyst layer will be subject to more research in the future, as the industry has not yet settled on a specific standard. In particular, the type of carbon black used has an effect on the resulting structure and composition of the CL. It would be useful to know how exactly it affects the mechanical behavior and failure, for example between carbon blacks that form circular clusters versus more elongated ones.

Finally, the numerical models that have been proposed in this study can be used for other purposes. Since they have been shown to be accurate over the range of environmental conditions, strains and strain rates that are relevant to the function of a fuel cell, the possibilities of application are numerous. To give an example, the models could be used to simulate the deformation of the MEA into the GDL when swollen under the effect of humidity, and study the possibility of buckling. Another application would be to study the distribution of compressive stresses that occur in the MEA when constrained and subjected to humidity cycles. Eventually, the author anticipates the development of a fully integrated numerical model, providing useful results at all stages of design and evaluation of a fuel cell.

Acknowledgements

I would like to express my sincere gratitude to my advisor Prof. Masaki Omiya. His guidance and encouragements were crucial at all steps of this thesis to help me achieve my research goals and are what made this thesis possible. Further, I thank him for his generosity in donating some of his research funds to help me attend conferences.

I would also like to thank the rest of my thesis committee for their advice and precious comments about this dissertation: Prof. Atsuhi Hotta, Prof. Jun Komotori and Prof. Shogo Miyata.

I am grateful to Ms. Yuki Kitayama and Mr. Yusuke Kai for their help in establishing the experimental framework for the cyclic fatigue experiments. I would also like to thank Mr. Yuki Arai for his assistance in conducting the DENT experimental testing.

Financial support for the three years of this project was generously provided by the Fujiwara foundation. Their support removed the financial burden of everyday student life, and allowed me to focus entirely on the research. I am also grateful to the KLL organization in Keio, who provided additional financial support for this work.

To all my peers and friends at Omiya Laboratory I also express many thanks for having conveyed a warm and agreeable atmosphere at work for the entire length of this project. You made this whole experience thoroughly enjoyable and unforgettable.

Finally, I would like to thank my family back in France for their unrelenting support throughout the project. Despite the distance you remained at my side for the entire journey, and your love has been a constant source of comfort.

Thank you to everyone who made this thesis possible; I hope that these relationships will keep flourishing as I now progress further towards my dreams.

References

1. Fuel Cell Today (2013), "The Fuel Cell Industry Review 2013"
2. McNicol B, Rand D and Williams K (2001), "Fuel cells for road transportation purposes - yes or no?", Journal of Power Sources, Vol. 100, pp. 47-59.
3. Shah A, Luo K, Ralph T and Walsh F (2011), "Recent trends and developments in polymer electrolyte membrane fuel cell modelling", Electrochimica Acta, Vol. 56, pp. 3731-3757.
4. Wanga Y, Chen KS, Mishler J, Cho SC and Adroher XC (2011), "A review of polymer electrolyte membrane fuel cells: Technology, applications, and needs on fundamental research", Applied Energy, Vol. 88, pp. 981-1007.
5. United States Department of Energy (2011), "Multi-Year Research, Development and Demonstration Plan: Technical Plan - Fuel Cells"
6. de Bruijn FA, Dam VAT and Janssen GJM (2008), "Review: Durability and Degradation Issues of PEM Fuel Cell Components", Fuel Cells, Vol. 8(1), pp. 3-22.
7. Luo Z, Li D, Tang H and M. Pan RR (2006), "Degradation behavior of membrane-electrode-assembly materials in 10-cell PEMFC stack", International Journal of Hydrogen Energy, Vol. 31, pp. 1831-1837.
8. Placca L and Kouta R (2011), "Fault tree analysis for PEM fuel cell degradation process modelling", International Journal of Hydrogen Energy, Vol. 36, pp. 12393-12405.
9. Aiyejina A and Sastry MKS (2012), "PEMFC Flow Channel Geometry Optimization: A Review", Journal of Fuel Cell Science and Technology, February, 2012. Vol. 9, p. 011011.
10. Promislow K and Wetton B (2009), "PEM Fuel Cells: A Mathematical Overview", Society for Industrial and Applied Mathematics, Vol. 70(2), pp. 369-409.
11. Das SK and Bansode AS (2009), "Heat and Mass Transport in Proton Exchange Membrane Fuel Cells - A Review", Heat Transfer Engineering, Vol. 30(9), pp. 691-719.
12. Escudero M, Hontanon E, Schwartz S, Boutonnet M and Daza L (2002),

"Development and performance characterisation of new electrocatalysts for PEMFC", Journal of Power Sources, Vol. 106, pp. 206-214.

13. Cerri I, Nagami T, Davies J, Mormiche C, Vecoven A and Hayden B (2013), "Innovative catalyst supports to address fuel cell stack durability", International Journal of Hydrogen Energy, Vol. 38, pp. 640-645.
14. Zhong C-J, Luo J, Fang B, Wanjala BN, Njoki PN, Loukrakpam R and Yin J (2010), "Nanostructured catalysts in fuel cells", Nanotechnology, Vol. 21, p. 062001.
15. Esmaeilifar A, Rowshanzamir S, Eikani M and Ghazanfari E (2010), "Synthesis methods of low-Pt-loading electrocatalysts for proton exchange membrane fuel cell systems", Energy, Vol. 35, pp. 3941-3957.
16. Yang G, Thongkam M, Vitidsant T, Yoneyama Y, Tan Y and Tsubaki N (2011), "A double-shell capsule catalyst with core-shell-like structure for one-step exactly controlled synthesis of dimethyl ether from CO2 containing syngas", Catalysis Today, Vol. 171, pp. 229-235.
17. Zhou X, Gan Y, Du J, Tian D, Zhang R, Yang C and Dai Z (2013), "A review of hollow Pt-based nanocatalysts applied in proton exchange membrane fuel cells", Journal of Power Sources, Vol. 232, pp. 310-322.
18. Yang H (2011), "Platinum-Based Electrocatalysts with Core-Shell Nanostructures", Angewandte Chemie International Edition, Vol. 50, pp. 2674-2676.
19. Jao T-C, Ke S-T, Chi P-H, Jung G-B and Chan S-H (2010), "Degradation on a PTFE/Nafion membrane electrode assembly with accelerating degradation technique", International Journal of Hydrogen Energy, Vol. 35, pp. 6941-6949.
20. Oyarce A, Zakrisson E, Ivity M, Lagergren C, Ofstad AB, Bodén A and Lindbergh G (2014), "Comparing shut-down strategies for proton exchange membrane fuel cells", Journal of Power Sources, Vol. 254, pp. 232-240
21. Luo M, Huang C, Liu W, Luo Z and Pan M (2010), "Degradation behaviors of polymer electrolyte membrane fuel cell under freeze/thaw cycles", international Journal of Hydrogen Energy, Vol. 35, pp. 2986-2993.
22. Sasmito AP, Birgersson E and Mujumdar AS (2012), "A novel flow reversal concept for improved thermal management in polymer electrolyte fuel cell stacks", International Journal of Thermal Sciences, Vol. 54, pp. 242-252.

23. Hickner MA, Ghassemi H, Kim YS, Einsla BR and McGrath JE (2004), "Alternative Polymer Systems for Proton Exchange Membranes (PEMs)", Chemical Reviews, Vol. 104(10), pp. 4587-4612.
24. Liyanage AD, Ferraris JP, Musselman IH, Yang D-J, Andersson TE, Son DY and Jr. KJB (2012), "Nafion-sulfonated dendrimer composite membranes for fuel cell applications", Journal of Membrane Science, Vol. 392-393, pp. 175-180.
25. Cele N and Ray SS (2009), "Recent Progress on Nafion-Based Nanocomposite Membranes for Fuel Cell Applications", Macromolecular Materials and Engineering, Vol. 294, pp. 719-738.
26. Yee R, Rozendal R, Zhang K and Ladewig B (2012), "Cost effective cation exchange membranes: A review", Chemical Engineering Research and Design, Vol. 90, pp. 950-959.
27. Mauritz KA and Moore RB (2004), "State of Understanding of Nafion", Chemical Reviews, Vol. 104, pp. 4535-4585.
28. Eastman SA, Kim S, Page KA, Rowe BW, Kang S and Soles CL (2012), "Effect of Confinement on Structure, Water Solubility, and Water Transport in Nafion Thin Films", Macromolecules, Vol. 45, pp. 7920-7930.
29. Yeo SC and Eisenberg A (1977), "Physical Properties and Supermolecular Structure of Perfluorinated Ion-Containing (Nafion) Polymers", Journal of Applied Polymer Science, Vol. 21, pp. 875-898.
30. Jalani NH and Datta R (2005), "The effect of equivalent weight, temperature, cationic forms, sorbates, and nanoinorganic additives on the sorption behavior of Nafion", Journal of Membrane Science, Vol. 264, pp. 167-175.
31. Duan Q, Wang H and Benziger J (2012), "Transport of liquid water through Nafion membranes", Journal of Membrane Science, Vol. 392, pp. 88-94.
32. Izquierdo-Gil M, V.M.Barragan, J.P.G.Villaluenga and M.P.Godino (2012), "Water uptake and salt transport through Nafion cation-exchange membranes with different thicknesses", Chemical Engineering Science, Vol. 72, pp. 1-9.
33. Sánchez LM (2012), "Experimental characterization of water sorption and transport properties of polymer electrolyte membranes for fuel cells". Thesis at: Université de Lorraine.
34. Otmani N, Morin A, Iorio SD, Rouillon L, Delette G, Blachot J-F, Gebel G and Besse S (2008), "Stresses in Nafion Membranes during Fuel Cell Operation",

CEA Grenoble.

35. Tang H, Peikang S, Jiang SP, Wang F and Pan M (2007), "A degradation study of Nafion proton exchange membrane of PEM fuel cells", Journal of Power Sources, Vol. 170, pp. 85-92.
36. Tang Y, Karlsson AM, Santare MH, Gilbert M, Cleghorn S and Johnson WB (2006), "An experimental investigation of humidity and temperature effects on the mechanical properties of perfluorosulfonic acid membrane", Materials Science and Engineering A, Vol. 425, pp. 297-304.
37. Solasi R, Huang X and Reifsnider K (2010), "Creep and stress-rupture of Nafion membranes under controlled environment", Mechanics of Materials, Vol. 42, pp. 678-685.
38. Dillard DA, Li Y, Grohs JR, Case SW, Ellis MW, Lai Y-H, Budinski MK and Gittleman CS (2009), "On the Use of Pressure-Loaded Blister Tests to Characterize the Strength and Durability of Proton Exchange Membranes", Journal of Fuel Cell Science and Technology, August, 2009. Vol. 6, p. 031014.
39. Satterfield MB and Benziger JB (2008), "Viscoelastic Properties of Nafion at Elevated Temperature and Humidity", Journal of Polymer Science: Part B: Polymer Physics Vol. 47, pp. 11-24.,
40. Majsztrik PW, Bocarsly AB and Benziger JB (2008), "Viscoelastic Response of Nafion. Effects of Temperature and Hydration on Tensile Creep", Macromolecules, Vol. 41, pp. 9849-9862.
41. Kusoglu A, Karlsson AM, Santare MH, Cleghorn S and Johnson WB (2006), "Mechanical response of fuel cell membranes subjected to a hygro-thermal cycle", Journal of Power Sources, Vol. 161, pp. 987-996.
42. Kusoglu A, Karlsson AM, Santare MH, Cleghorn S and Johnson WB (2007), "Mechanical behavior of fuel cell membranes under humidity cycles and effect of swelling anisotropy on the fatigue stresses", Journal of Power Sources, Vol. 170, pp. 345-358.
43. Kusoglu A, Tang Y, Santare MH, Karlsson AM, Cleghorn S and Johnson WB (2009), "Stress-Strain Behavior of Perfluorosulfonic Acid Membranes at Various Temperatures and Humidities: Experiments and Phenomenological Modeling", Journal of Fuel Cell Science and Technology, February, 2009. Vol. 6, p. 011012.
44. Huang X, Solasi R, Zou Y, Feshler M, Reifsnider K, Condit D, Burlatsky S and

Madden T (2006), "Mechanical Endurance of Polymer Electrolyte Membrane and PEM Fuel Cell Durability", Journal of Polymer Science: Part B: Polymer Physics, Vol. 44, pp. 2346-2357.

45. Solasi R, Zou Y, Huang X, Reifsnider K and Condit D (2007), "On mechanical behavior and in-plane modeling of constrained PEM fuel cell membranes subjected to hydration and temperature cycles", Journal of Power Sources, Vol. 167, pp. 366-377.
46. Lai Y-H, Mittelsteadt CK, Gittleman CS and Dillard DA (2009), "Viscoelastic Stress Analysis of Constrained Proton Exchange Membranes Under Humidity Cycling", Journal of Fuel Cell Science and Technology, May, 2009, Vol. 6, p. 021002.
47. Pestrak M, Li Y, Case SW, Dillard DA, Ellis MW, Lai Y-H and Gittleman CS (2010), "The Effect of Mechanical Fatigue on the Lifetimes of Membrane Electrode Assemblies", Journal of Fuel Cell Science and Technology, August, 2010. Vol. 7, p. 041009.
48. Solasi R, Zou Y, Huang X and Reifsnider K (2008), "A time and hydration dependent viscoplastic model for polyelectrolyte membranes in fuel cells", Mechanics of Time-Dependent Materials, Vol. 12, pp. 15-30.
49. Yoon W and Huang X (2011), "A nonlinear viscoelastic--viscoplastic constitutive model for ionomer membranes in polymer electrolyte membrane fuel cells", Journal of Power Sources, Vol. 196, pp. 3933-3941.
50. Bergstrom J and Boyce M (1998), "Constitutive modeling of the large strain time-dependant behavior of elastomers", Journal of the Mechanics and Physics of Solids, Vol. 46(5), pp. 931-954.
51. Silberstein MN (2008), "Mechanics of proton exchange membranes: time, temperature, and hydration dependence of the stress-strain behavior of persulfonated polytetrafluoroethylene". Thesis at: Massachusetts Institute of Technology.
52. Silberstein MN and Boyce MC (2010), "Constitutive modeling of the rate, temperature, and hydration dependent deformation response of Nafion to monotonic and cyclic loading", Journal of Power Sources. Vol. 195, pp. 5692-5706.
53. Silberstein MN, Pillai PV and Boyce MC (2011), "Biaxial elastic-viscoplastic

behavior of Nafion membranes", Polymer, Vol. 52, pp. 529-539.

54. Silberstein MN and Boyce MC (2011), "Hygro-thermal mechanical behavior of Nafion during constrained swelling", Journal of Power Sources, Vol. 196, pp. 3452-3460.
55. Silberstein MN (2011), "Mechanics of multi-physics deformation behavior of polymer electrolyte membranes". Thesis at: Massachusetts Institute of Technology., June, 2011.
56. Wang B, Lu H and ho Kim G (2002), "A damage model for the fatigue life of elastomeric materials", Mechanics of Materials, Vol. 34, pp. 475-483.
57. Zarrin-Ghalami T and Fatemi A (2012), "Cumulative fatigue damage and life prediction of elastomeric components", Fatigue and Fracture of Engineering Materials and Structures, Vol. 36, pp. 270-279.
58. Zarrin-Ghalami T and Fatemi A (2012), "Material Deformation and Fatigue Behavior Characterization for Elastomeric Component Life Predictions", Polymer Engineering and Science, Vol. 52, pp. 1795-1805.
59. Zhang S, Yuan X, Wang H, Mérida W, Zhu H, Shen J, Wu S and Zhang J (2009), "A review of accelerated stress tests of MEA durability in PEM fuel cells", International Journal of Hydrogen Energy, Vol. 34, pp. 388-404.
60. Kai Y, Omiya YKM, Uchiyama T and Kumei H (2014), "In Situ Observation of Deformation Behavior of Membrane Electrode Assembly Under Humidity Cycles", Journal of Fuel Cell Science and Technology, Vol. 11, p. 051006.
61. Feng Rong CH, Liu Z-S, Song D and Wang Q (2008), "Microstructure changes in the catalyst layers of PEM fuel cells induced by load cycling Part I. Mechanical model", Journal of Power Sources, Vol. 175, pp. 699-711.
62. Saha LK, Tabe Y and Oshima N (2012), "Effect of GDL deformation on the pressure drop of polymer electrolyte fuel cell separator channel", Journal of Power Sources, Vol. 202, pp. 100-107.
63. Song D, Wang Q, Liu Z-S and Huang C (2006), "Transient analysis for the cathode gas diffusion layer of PEM fuel cells", Journal of Power Sources, Vol. 159, pp. 928-942.
64. Arvay A, Yli-Rantala E, Liu C-H, Peng X-H, Koski P, Cindrella L, Kauranen P, Wilde P and Kannan A (2012), "Characterization techniques for gas diffusion layers for proton exchange membrane fuel cells - A review", Journal of Power

Sources, Vol. 213, pp. 317-337.

65. Williams MV, Begg E, Bonville L, Kunz HR and Fenton JM (2004), "Characterization of Gas Diffusion Layers for PEMFC", Journal of The Electrochemical Society, Vol. 151(8), pp. A1173-A1180.
66. Poornesh K, Cho C, Lee G and Tak Y (2010), "Gradation of mechanical properties in gas diffusion electrode. Part 1: Influence of nano-scale heterogeneity in catalyst layer on interfacial strength between catalyst layer and membrane", Journal of Power Sources, Vol. 195, pp. 2709-2717.
67. Poornesh K, Cho C, Lee G and Tak Y (2010), "Gradation of mechanical properties in gas-diffusion electrode. Part 2: Heterogeneous carbon fiber and damage evolution in cell layers", Journal of Power Sources, Vol. 195, pp. 2718-1730.
68. Yoon G-H, Park SB, Kim EH, Oh M-H, Cho K-S, Jeong SW, Kim S and il Park Y (2009), "Novel hydrophobic coating process for gas diffusion layer in PEMFCs", Journal of Electroceramics, Vol. 23, pp. 110-115.
69. Joo J, Choun M, Kim K, Uhm S, Kim YD and Lee J (2014), "Controlled water flooding of polymer electrolyte fuel cells applying superhydrophobic gas diffusion layer", Current Applied Physics, Vol. 14, pp. 1374-1379.
70. Lin G and Nguyen TV (2005), "Effect of Thickness and Hydrophobic Polymer Content of the Gas Diffusion Layer on Electrode Flooding Level in a PEMFC", Journal of The Electrochemical Society, Vol. 152(10), pp. A1942-A1948.
71. Liu P, Yin G-P and Lai Q-Z (2009), "Gold-plated Ni mesh as the gas diffusion medium for air-breathing direct methanol fuel cell", International Journal of Hydrogen Research, Vol. 33, pp. 1-7.
72. Arisetty S, Prasad AK and Advani SG (2007), "Metal foams as flow field and gas diffusion layer in direct methanol fuel cells", Journal of Power Sources, Vol. 165, pp. 49-57.
73. Ye D-H and Zhan Z-G (2013), "A review on the sealing structures of membrane electrode assembly of proton exchange membrane fuel cells", Journal of Power Sources, Vol. 231, pp. 285-292.
74. Wang X-D, Duan Y-Y, Yan W-M and Peng X-F (2008), "Local transport phenomena and cell performance of PEM fuel cells with various serpentine flow field designs", Journal of Power Sources, Vol. 175, pp. 397-407.

75. Wang J and Wang H (2012), "Flow-Field Designs of Bipolar Plates in PEM Fuel Cells: Theory and Applications", Fuel Cells, Vol. 12(6), pp. 989-1003.
76. Hamilton PJ and Pollet B (2010), "Polymer Electrolyte Membrane Fuel Cell (PEMFC) Flow Field Plate: Design, Materials and Characterisation", Fuel Cells, Vol. 10(4), pp. 489-509.
77. Yan X, Hou M, Zhang H, Jing F, Ming P and Yi B (2006), "Performance of PEMFC stack using expanded graphite bipolar plates", Journal of Power Sources, Vol. 160, pp. 252-257.
78. Park T, Chang I, Lee YH, Ji S and Cha SW (2014), "Analysis of operational characteristics of polymer electrolyte fuel cell with expanded graphite flow-field plates via electrochemical impedance investigation", Energy, Vol. 66, pp. 77-81.
79. Du C, Ming P, Hou M, Fu J, Fu Y, Luo X, Shen Q, Shao Z and Yi B (2010), "The preparation technique optimization of epoxy/compressed expanded graphite composite bipolar plates for proton exchange membrane fuel cells", Journal of Power Sources, Vol. 195, pp. 5312-5319.
80. Alayavalli K and Bourell DL (2010), "Fabrication of modified graphite bipolar plates by indirect selective laser sintering (SLS) for direct methanol fuel cells", Rapid Prototyping Journal, Vol. 16(4), pp. 268-274.
81. Sykam N, Gautam RK and Kar KK (2015), "Electrical, Mechanical, and Thermal Properties of Exfoliated Graphite/Phenolic Resin Composite Bipolar Plate for Polymer Electrolyte Membrane Fuel Cell", Polymer Engineering and Science, Vol. 55, pp. 917-923.
82. Kang K, Park S and Ju H (2014), "Effects of type of graphite conductive filler on the performance of a composite bipolar plate for fuel cells", Solid State Ionics, Vol. 262, pp. 332-336.
83. Hui C, Bo LH, Jian-Xin L, Li Y and Yue-De H (2009), "Characteristics and Preparation of Polymer/Graphite Composite Bipolar Plate for PEM Fuel Cells", Journal of Composite Materials, Vol. 43(7), pp. 755-767.
84. Antunes RA, de Oliveira M.CL, Ett G and Ett V (2011), "Carbon materials in composite bipolar plates for polymer electrolyte membrane fuel cells: A review of the main challenges to improve electrical performance", Journal of Power Sources, Vol. 196, pp. 2945-2961.
85. de Oliveira MCL, Ett G and Antunes RA (2012), "Materials selection for bipolar

plates for polymer electrolyte membrane fuel cells using the Ashby approach", Journal of Power Sources, Vol. 206, pp. 3-13.

86. Tian R (2011), "Chromium nitride/Cr coated 316L stainless steel as bipolar plate for proton exchange membrane fuel cell", Journal of Power Sources, Vol. 196, pp. 1258-1263.
87. S.-T.Myung, Sakurada S, Kumagai and H.Yashiro (2010), "A Promising Alternative to PEMFC Graphite Bipolar Plates: Surface Modified Type 304 Stainless Steel with TiN Nanoparticles and Elastic Styrene Butadiene Rubber Particles", Fuel Cells, Vol. 10(4), pp. 545-555.
88. Kim KM, Park JH, Kim HS, Kim JH, Lee YY and Kim KY (2012), "Effect of plastic deformation on the corrosion resistance of ferritic stainless steel as a bipolar plate for polymer electrolyte membrane fuel cells", International Journal of Hydrogen Energy, Vol. 37, pp. 8459-8464.
89. Tawfik H, Hung Y and Mahajan D (2007), "Metal bipolar plates for PEM fuel cell - A review", Journal of Power Sources, Vol. 163, pp. 755-767.
90. Netwall CJ, Gould BD, Rodgers JA, Nasello NJ and Swider-Lyons KE (2013), "Decreasing contact resistance in proton-exchange membrane fuel cells with metal bipolar plates", Journal of Power Sources, Vol. 227, pp. 137-144.
91. Ren Z, Zhang D and Wang Z (2012), "Stacks with TiN/titanium as the bipolar plate for PEMFCs", Energy, Vol. 48, pp. 577-581.
92. Jin CK, Jeong MG and Kang CG (2014), "Fabrication of titanium bipolar plates by rubber forming and performance of single cell using TiN-coated titanium bipolar plates", International Journal of Hydrogen Energy, Vol. 39, pp. 21480-21488.
93. Wang S-H, Peng J, Lui W-B and Zhang J-S (2006), "Performance of the gold-plated titanium bipolar plates for the light weight PEM fuel cells", Journal of Power Sources, Vol. 162, pp. 486-491.
94. Oh M-H, Yoon Y-S, Park S-G, Kima JY, Kim HH and Tetsuya O (2004), "The Electrical Properties of Aluminum Bipolar Plate for PEM Fuel Cell System", Transactions on Electrical and Electronic Materials, Vol. 5(5), pp. 204-207.
95. Jin CK, Jung M and Kang C (2014), "Fabrication of Aluminum Bipolar Plates by Semi-solid Forging Process and Performance Test of TiN Coated Aluminum Bipolar Plates", Fuel Cells, Vol. 14, pp. 551-560.

96. El-Enin SAA, Abdel-Salam OE, El-Abd H and Amin AM (2008), "New electroplated aluminum bipolar plate for PEM fuel cell", Journal of Power Sources, Vol. 177, pp. 131-136.

97. McGuigan A, Briggs G, Burlakov V, Yanaka M and Tsukahara Y (2003), "An elastic-plastic shear lag model for fracture of layered coatings", Thin Solid Films, Vol. 424, pp. 219-223.

98. Vermot des Roches T (2012), "Failure Prediction for Membrane Electrode Assembly". Master's Thesis at: Keio University.

99. Vengatesan S, Panha K, Fowler MW, Yuan X-Z and Wang H (2012), "Membrane electrode assembly degradation under idle conditions via unsymmetrical reactant relative humidity cycling", Journal of Power Sources, Vol. 207, pp. 101-110.

100. Vengatesan S, Fowler MW, Yuan X-Z and Wang H (2011), "Diagnosis of MEA degradation under accelerated relative humidity cycling", Journal of Power Sources, Vol. 196, pp. 5045-5052.

101. Cantournet S, Desmorat R and Besson J (2009), "Mullins effect and cyclic stress softening of filled elastomers by internal sliding and friction thermodynamics model", International Journal of Solids and Structures, Vol. 46, pp. 2255-2264.

102. Diani J, Gilormini P, Merckel Y and Vion-Loisel F (2013), "Micromechanical modeling of the linear viscoelasticity of carbon-black filled styrene butadiene rubbers: The role of the filler--rubber interphase", Mechanics of Materials, Vol. 59, pp. 65-72.

103. Huang J-C (2002), "Carbon Black Filled Conducting Polymers and Polymer Blends", Advances in Polymer Technology, Vol. 21(4), pp. 299-313.

104. Jha V (2008), "Carbon Black Filler Reinforcement of Elastomers". Ph.D Thesis at: University of London.

105. Bárány T, Czigány T and Karger-Kocsis J (2010), "Application of the essential work of fracture (EWF) concept for polymers, related blends and composites: A review", Progress in Polymer Science, Vol. 35, pp. 1257-1287.

106. Group ET-4 (1993), "Testing Protocol for Essential Work of Fracture"

107. Karger-Kocsis J and Czigfiny T (1996), "On the essential and non-essential work of fracture of biaxial-oriented filled PET film", Polymer, Vol. 37(12), pp. 2433-2438.

108. Ching ECY, Li RKY and Mai Y-W (2000), "Effects of Gauge Length and Strain Rate on Fracture Toughness of Polyethylene Terephthalate Glycol (PETG) Film Using The Essential Work of Fracture Analysis", Polymer Engineering and Science, Vol. 40(2), pp. 310-319.
109. Poon W, Ching E, Cheng C and Li R (2001), "Measurement of plane stress essential work of fracture (EWF) for polymer films: effects of gripping and notching methodology", Polymer Testing, Vol. 20, pp. 295-401.
110. Li Y, Quincy JK, Case SW, Ellis MW, Dillard DA, Lai Y-H, Budinski MK and Gittleman CS (2008), "Characterizing the fracture resistance of proton exchange membranes", Journal of Power Sources, Vol. 185, pp. 374-380.
111. Kai Y, Kitayama Y, Omiya M, Uchiyama T and Kato M (2013), "Crack Formation in Membrane Electrode Assembly Under Static and Cyclic Loadings", Journal of Fuel Cell Science and Technology, Vol. 10, p. 021007.
112. Xin G, Hangong W, Xingwu K and Liangzhou J (2010), "Analytic solutions to crack tip plastic zone under various loading conditions", European Journal of Mechanics A/Solids, Vol. 29, pp. 738-745.

APPENDIX A

List of Publications

Articles on Periodicals

1) Vermot des Roches, T. and Omiya, M., Failure Prediction for Membrane Electrode Assembly, Journal of Computational Science and Technology, Vol.7; No.2; Page.221-230; (2013)

2) Vermot des Roches, T., Arai, Y. and Omiya, M., Effect of Environmental Condition on Essential Work of Fracture of Proton Exchange Membranes, Mechanical Engineering Journal, Vol.2, No.5, p.15-00320 (2015)

Articles on international conference proceedings

1) Vermot des Roches, T.* and Omiya, M., Failure Prediction for Membrane Electrode Assembly, Proceedings of JSME-CMD International Computational Mechanics Symposium (ICMS 2012, Kobe, Japan), MS4-5-2, (2012)

2) Vermot des Roches, T.* and Omiya, M., Calculating the essential work of fracture

of proton exchange membranes using a finite element analysis, Recent Advances in Structural Integrity Analysis: Proceedings of the International Congress APCFS/SIF-2014 (APCFS/SIF 2014, Sydney, Australia), pp. 17-21, (2014)

Presentations at international conferences

1) Vermot des Roches, T.* and Omiya, M., Mechanical Behavior and Failure of Membrane Electrode Assembly in Proton Exchange Membrane Fuel Cells, 7th International Conference on Fracture of Polymers, Composites and Adhesives (ESIS 2014, Les Diablerets, Switzerland)(2014)

Presentations at domestic meetings

1) Vermot des Roches, T.* and Omiya, M., Failure Prediction for Membrane Electrode Assembly, 日本機械学会 M&M2012 材料力学カンファレンス (M&M 2012, 松山), OS0620, (2012)